UNIVERSIDAD NACIONAL AUTÓNOMA DE MÉXICO

POSGRADO EN CIENCIAS FÍSICAS

INSTITUTO DE CIENCIAS NUCLEARES

ACCRETION OF A RELATIVISTIC COLLISIONLESS KINETIC GAS ONTO A BLACK HOLE FROM FINITE RADIUS

T E S I S

QUE PARA OPTAR POR EL GRADO DE:

MAESTRO EN CIENCIAS (FÍSICA)

PRESENTA:

ALDO JAVIER GAMBOA CASTILLO

TUTOR PRINCIPAL:

DR. DARÍO NÚÑEZ ZÚÑIGA
INSTITUTO DE CIENCIAS NUCLEARES

MIEMBROS DEL COMITÉ TUTOR:

DRA. CELIA DEL CARMEN ESCAMILLA RIVERA
INSTITUTO DE CIENCIAS NUCLEARES

DR. JOSÉ ALBERTO VÁZQUEZ GONZÁLEZ
INSTITUTO DE CIENCIAS FÍSICAS

CIUDAD UNIVERSITARIA, CD. MX., AGOSTO DE 2022

"If I have seen further, it is by standing on the shoulders of giants."
Sir Isaac Newton

"It followed from the special theory of relativity that mass and energy are both but different manifestations of the same thing – a somewhat unfamiliar conception for the average mind."
Albert Einstein

Agradecimientos

Primero que nada, quisiera agradecer a mis padres (y a todos mis ascendientes) pues ellos fueron quienes, gracias al esfuerzo y a las decisiones que tomaron durante su vida, me otorgaron ciertas condiciones iniciales y de frontera, así como fuerzas impulsoras y restauradoras, para llegar a donde me encuentro.

Una clave fundamental para todos mis éxitos ha sido la compañía de mi mejor amiga y esposa, Jessica. No solamente ha sido la principal y casi única compañía que he tenido durante este viaje, sino que me ha motivado siempre a dar lo mejor de mí en cualquier escenario. Sin duda alguna, su confianza en mis capacidades me ha hecho sentir seguro y me ha permitido dar siempre pasos firmes.

También quisiera agradecer a mi amigo Ulil por acompañarme y escucharme, aunque sea virtualmente, durante toda mi licenciatura y maestría, así como a mi amigo Víctor Knapp por impulsarme y motivarme a ser un mejor Físico. Sin duda alguna, este es un trayecto que no puede recorrerse solo.

Además, quisiera darle las gracias a mi asesor, el Dr. Darío Núñez, por el constante apoyo y motivación que me ha otorgado desde que me adoptó como su estudiante antes de iniciar mi maestría. Gracias a él pude involucrarme en el tema de esta tesis y pude conocer a excelentes personas e investigadoræs. En particular, los resultados de esta tesis se lograron gracias al trabajo y a las valiosas discusiones que tuve con el Dr. Darío, el Dr. Olivier Sarbach, la Dra. Paola Domínguez y el futuro Dr. Carlos Gabarrete, a quien le estoy infinitamente agradecido por orientarme cuando encontré algunos obstáculos durante la realización de este trabajo.

Resumen

La acreción es un mecanismo muy importante para la astrofísica y la cosmología observacional pues tiene un rol fundamental en la formación y evolución de planetas, estrellas, estrellas de neutrones, agujeros negros (ANs) y galaxias debido a la naturaleza atractiva de la gravedad. Sin embargo, entender el proceso de acreción es una tarea difícil porque requiere de diversas ramas de la física para modelar el flujo de acreción y todas las interacciones involucradas.

Una de las primeras suposiciones que se debe hacer está relacionada con el *régimen* (Newtoniano o relativista) en el que modelamos el problema de acreción. Para gases que se mueven a muy altas velocidades y/o en fuertes campos gravitacionales, naturalmente esperamos que una descripción relativista sea significativamente mejor. Otra suposición está relacionada con la *naturaleza del flujo acretante* (hidrodinámica o cinética). En muchos escenarios astrofísicos la aproximación hidrodinámica es la más adecuada. Sin embargo, hay ciertos casos en los que esperamos que un tratamiento cinético daría mejores resultados, por ejemplo, en la acreción de flujos radiativamente ineficientes y poco colisionales que se encuentran cerca de ANs supermasivos (como Sgr A* y M87*), y en la acreción de materia oscura hacia ANs. Combinando estas dos suposiciones acerca del régimen del modelo y la naturaleza del flujo de acreción, se vuelve claro que necesitamos una Teoría Cinética compatible con la Relatividad General para describir completamente la acreción de gases cinéticos cerca de ANs.

En este sentido, estudios previos han tratado el problema de la acreción relativista de un gas cinético sin colisiones hacia un AN especificando las condiciones de frontera en el infinito, es decir, una nube de gas infinita que acreta hacia un AN. A primera vista, esta es una suposición incorrecta ya que esperamos que todos los sistemas astrofísicos tengan un tamaño finito. Sin embargo, es necesario un análisis cuidadoso para validar o refutar esta suposición.

Motivados por este problema, en este trabajo utilizaremos la Teoría Cinética compatible con la Relatividad General para modelar, por primera vez, la acreción de un gas de partículas sin colisiones hacia un AN *desde un radio finito* (los resultados presentados en este trabajo fueron publicados en Gamboa et al. 2021). Como primera aproximación, supondremos

una acreción esférica y estática hacia un AN de Schwarzschild. Modelaremos la acreción puramente radial en la que todas las partículas tienen momento angular nulo, y luego pasaremos a un modelo más realista en el que las partículas tienen momento angular. Las tasas de acreción resultantes se analizarán y compararán con modelos anteriores, incluido el modelo de Bondi estándar para un flujo hidrodinámico. Al final, aplicaremos nuestros modelos a los flujos de Sgr A* y M87*, y discutiremos cómo su baja luminosidad podría explicarse parcialmente por una descripción cinética que involucre al momento angular. Nuestros resultados son consistentes con cotas anteriores (dependientes del modelo) para la tasa de acreción impuestas por las mediciones de la rotación de luz polarizada procedente de Sgr A* y con estimaciones de la tasa de acreción de M87* por parte de la colaboración Event Horizon Telescope.

La estructura de esta tesis es la siguiente: En el Capítulo 1 introduciremos conceptos básicos de Relatividad General necesarios para estudiar algunas de las propiedades de los ANs relevantes para el problema de acreción, como la dinámica de partículas de prueba masivas que se mueven alrededor de un AN de Schwarzschild. En el Capítulo 2 vamos a presentar los aspectos fundamentales de la acreción astrofísica; además, nos centraremos en la comprensión actual de los flujos de acreción de ANs, y revisaremos los modelos y métodos actuales que se utilizan para estimar las tasas de acreción de Sgr A* y M87*. En el Capítulo 3 presentaremos las ideas básicas de la Teoría Cinética y sus generalizaciones relativistas; nos centraremos en la Teoría Cinética compatible con la Relatividad General y su relación con el proceso de acreción. Al final, en el Capítulo 4 vamos a utilizar los conceptos y el formalismo desarrollado en capítulos anteriores, para estudiar el problema de la acreción relativista desde radio finito y su aplicación a los flujos de acreción de Sgr A* y M87*.

Abstract

Accretion is a very important mechanism for astrophysics and observational cosmology since it has a fundamental role in the formation and evolution of planets, stars, neutron stars, black holes (BHs) and galaxies due to the attractive nature of gravity. However, understanding the accretion process is a difficult task because we require several branches of physics to model the accretion flow and all the interactions involved. Depending on the astrophysical scenario, we may use different approximations to make the problem more tractable.

One of the first assumptions that must be done is related to the *regime* (Newtonian or relativistic) in which we will model the accretion problem. For gases moving at very high velocities and/or in strong gravitational fields, we naturally expect a special or general relativistic description to be significantly better. Another assumption is related to the *nature of the accreting flow* (hydrodynamic or kinetic). In many astrophysical scenarios the hydrodynamic approximation is the most appropriate. However, there are certain cases in which we expect that a kinetic treatment would give better results, for example, in the accretion of nearly collisionless radiatively inefficient flows that are near supermassive BHs (such as Sgr A* and M87*), and in the dark matter accretion onto BHs. Combining these two assumptions about the regime of the model and the nature of the accreting flow, it becomes clear that we need a *general relativistic Kinetic Theory* in order to completely describe the accretion of kinetic gases near BHs.

In this regard, previous studies have treated the problem of relativistic accretion of a collisionless kinetic gas onto a BH by specifying boundary conditions at infinity, that is, an infinite gas cloud accreting onto a BH. At first glance, this is an incorrect supposition since we expect that all astrophysical systems have a finite size. However, a careful analysis is needed in order to validate or disprove this assumption.

Motivated by this problem, in this work we will use general relativistic kinetic theory to model, for the first time, the accretion of a collisionless gas of particles onto a BH *from finite radius* (the results presented in this work were published in Gamboa et al. 2021). As a first approximation, we will assume a steady, spherical accretion onto a

Schwarzschild BH. We will model the purely radial accretion in which all the particles have zero angular momentum, and then we will move on to a more realistic model in which the particles do have angular momentum. The resulting mass accretion rates will be analyzed and compared with previous models, including the standard Bondi model for a hydrodynamic flow. At the end, we will apply our models to the flows of Sgr A* and M87*, and we will discuss how their low luminosity could be partially explained by a kinetic description involving angular momentum. Our results are consistent with previous model-dependent bounds for the accretion rate imposed by rotation measures of the polarized light coming from Sgr A* and with estimations of the accretion rate of M87* from the Event Horizon Telescope collaboration.

The structure of this thesis is as follows: In Chapter 1 we will introduce basic concepts of General Relativity needed to study some of the properties of BHs relevant to the accretion problem, such as the dynamics of massive test particles moving around a Schwarzschild BH. In Chapter 2 we are going to present the fundamental aspects of astrophysical accretion; additionally, we will focus on the present understanding of BH accretion flows, and we are going to review the current models and methods that are used to estimate the accretion rates of Sgr A* and M87*. In Chapter 3 we will present the basic ideas of Kinetic Theory and its relativistic generalizations; we will focus in general relativistic Kinetic Theory and its relation to the accretion process. At the end, in Chapter 4 we are going to use the concepts and the formalism developed in previous chapters, to study the problem of relativistic accretion from finite radius and its application to the accretion flows of Sgr A* and M87*.

Table of contents

Chapter 1

Black Holes

One of the most astonishing predictions of General Relativity (GR) is the existence of black holes (BHs). These entities are full of exciting properties, unexpected from our daily Newtonian life. Time delay, gravitational redshift, a zone of no-return, *spaghettification* (or extreme tidal forces) and singularities, are all phenomena associated to the presence of a BH. Usually, these objects are not alone: they could be accreting matter from a nearby star or completely disrupting a neutron star, or they could be in a beautiful dance with another BH emitting gravitational waves until their coalescence. BHs and their astrophysical consequences have been thoroughly studied over the years and several observations have been confirming our knowledge about their properties.

In this chapter we are going to introduce basic concepts of GR needed to study some of the properties of BHs (Sec. 1.1). Then, after reviewing a historical account of BHs (Sec. 1.2), we are going to focus in the dynamics of massive test particles moving around a Schwarzschild BH (Sec. 1.3). Our purpose will be to establish a connection with the phenomenon of general relativistic astrophysical accretion.

1.1 Fundamentals of General Relativity

Einstein's theory of GR describes gravitational phenomena from an elegant geometrical point of view, in which the effects of gravity are explained in terms of space-time curvature induced by the presence of energy. It is the generalization of the theory of Special Relativity (SR) which focuses on the properties of a flat (Minkowski) space-time. GR is considered one of the pillars of modern physics due to its completeness as a physical theory and its success describing several observations ranging from Earth-size experiments, to Solar system tests, and even going beyond describing the Universe as a whole (see e.g. Berti et al. 2015; Turyshev

2008; Will 2014). In this section we will give a very brief *reminder* of basic GR concepts needed in this work (we are going to assume prior basic knowledge of GR). We refer the reader to the book of D'Inverno (1992) for concepts of SR, to the books of Nakahara (2003); Renteln (2014) for the mathematical aspects of GR, and to the books of Carroll (2004); Straumann (2013); Wald (1984) for a detailed presentation of GR.

In GR a *space-time* is characterized by a differentiable manifold M of dimension 4 (whose elements or points are known as *events*) and a pseudo-Riemannian metric g which allows us to calculate important physical quantities, such as proper distances, time lapses and the trajectories of test particles (the *geodesics* of the space-time). The manifold M can be covered with *coordinate charts* $\{x^\mu\}$, so that a point $x \in M$ has *local coordinates* $(x^0, x^i) = (ct, x^i)$, where c is the speed of light in vacuum, t is the time coordinate and x^i $(i = 1,2,3)$ are the spatial coordinates for a certain system of reference.

We can also define additional structures related to the space-time manifold (they will be needed to formulate a General Relativistic Kinetic Theory in Chapter 3). At each $x \in M$ we can define the *tangent space* T_xM (also with dimension 4) as the set of *vectors* which act on scalar functions defined over M. Since T_xM is a linear vector space, we can construct its dual space called the *cotangent space* T_x^*M whose elements are dual vectors. By considering tensor products between T_xM and T_x^*M we can construct the main mathematical objects in differential geometry known as *tensors*. Moreover, we can associate all the points in M together with their tangent spaces (cotangent spaces) in another manifold called the *tangent bundle* TM (*cotangent bundle* T^*M) of dimension 8. A more complete discussion of these geometrical definitions can be found in Nakahara (2003); Renteln (2014).

Tensors are used to write equations in a *covariant* way. The covariant formulation establishes the equivalence between arbitrary systems of coordinates, which was precisely one of Einstein's main motivations to follow a geometrical point of view. For example, Einstein's field equations are written as the following combination of tensors:

$$G_{\mu\nu} := R_{\mu\nu} - \frac{1}{2} R g_{\mu\nu} = \frac{8\pi G}{c^4} T_{\mu\nu}, \tag{1.1}$$

where $G_{\mu\nu}$ is the Einstein tensor, $R_{\mu\nu}$ is the Ricci tensor, R is the Ricci scalar, $g_{\mu\nu}$ are the components of the metric, G is Newton's gravitational constant and $T_{\mu\nu}$ is the energy-momentum tensor. These equations describe the structure of space-time given a distribution of energy, and they are equivalent for all observers since the equations are written in a covariant manner. Furthermore, the Einstein and energy-momentum tensors satisfy a conservation law

$$\nabla^\mu G_{\mu\nu} = 0 \qquad \text{and} \qquad \nabla^\mu T_{\mu\nu} = 0, \tag{1.2}$$

where ∇^μ is the *covariant derivative* obtained from the Levi-Civita connection associated to the differentiable manifold M and to the metric g. Our purpose is to solve Einstein's field equations for different physical configurations. However, this is a formidable task because these equations form a coupled system of 10 non-linear partial differential equations for the components of the metric, subject to the four constrictions $\nabla^\mu G_{\mu\nu} = 0$.

There are several analytical and approximate methods to solve Einstein's equations for different physical scenarios. One of the main strategies to obtain simple solutions has been to assume certain *symmetries* of the space-time. With this methodology, people have obtained very interesting solutions known as *black holes*, which is the topic of the following section. A particularly important solution representing a *stationary, spherically symmetric space-time* is described by the following line element[1] (see e.g. Wald 1984)

$$ds^2 = g_{mn}(r)\,dx^m dx^n + r^2\left(d\theta^2 + \sin^2\theta d\phi^2\right), \tag{1.3}$$

where r is the radial coordinate,[2] θ and ϕ are the standard angular coordinates on a 2-sphere, and $m,n \in \{t,r\}$. Using Eq. (1.3) as an *ansatz* in the Einstein's field equations (1.1), we can obtain differential equations for the metric coefficients g_{mn}.

As we mentioned earlier, with the metric we can compute several important physical aspects of the space-time. Particularly, we can calculate the trajectories of test particles, which are known as the *geodesics* of the space-time. To understand the definition of a geodesic, we first introduce very basic notions of the movement of a particle in a given space-time. Suppose that a particle follows a curve which is parametrized by a certain variable λ. In this way, the local coordinates of the curve will be given by the four functions $x^\mu = x^\mu(\lambda)$, such that $x^0 = c\,t(\lambda)$ and $x^i = x^i(\lambda)$, and the tangent vector to this curve will be $u^\mu := dx^\mu/d\lambda$.

A very important property of GR is that, locally, the dynamics of particles is determined by the principles of SR (see e.g. D'Inverno 1992). In this framework, particles with rest mass m follow *time-like curves*[3] to ensure that the speed of massive particles is less than the speed of light. The *proper time*[4] τ is a particularly important choice of the parameter λ for massive particles; the corresponding tangent vector is known as the *four-velocity* and it has a constant

[1] Throughout this work we are going to use the signature $(-,+,+,+)$ for the space-time metric, and we will follow Einstein's summation convention.

[2] The coordinate r is known as the *areal radius* because it is defined in terms of the total area A of a 2-sphere, as $r = \sqrt{A/4\pi}$.

[3] A time-like curve is such that its tangent vector u^μ satisfies $g_{\mu\nu}u^\mu u^\nu < 0$ along the curve.

[4] The proper time along a time-like curve represents the time as measured by a clock following that curve, and it is independent of the choice of a coordinate system.

length. In the formalism of GR, the constant length condition is expressed as

$$g_{\mu\nu}u^\mu u^\nu = g_{\mu\nu}\frac{dx^\mu}{d\tau}\frac{dx^\nu}{d\tau} = -c^2, \tag{1.4}$$

which is a representation of the constancy of the speed of light. Additionally, we can define the *four-momentum* as

$$p^\mu := mu^\mu, \tag{1.5}$$

such that it satisfies the so-called *on-shell restriction*

$$g_{\mu\nu}p^\mu p^\nu = -m^2c^2. \tag{1.6}$$

With these definitions that come from SR, we can proceed to explain the concept of a geodesic. A *geodesic* is defined to be a curve whose tangent vectors remain parallel if they are transported along it (the so-called *parallel transport*); in this way, geodesics are the straightest trajectories that a particle can follow in a certain space-time. Naturally, in flat space-time geodesics are straight lines, however, this is not the case when curvature is present. In the formalism of differential geometry, the geodesic equation can be obtained by demanding that the tangent vector u^μ of an *affinely parametrized* curve $x^\mu = x^\mu(\lambda)$ obeys the condition[5]

$$u^\nu\nabla_\nu u^\mu = 0, \tag{1.7}$$

written in local coordinates. Using the coordinate expression of the covariant derivative,[6] the *geodesic equation* (1.7) transforms to

$$\frac{d^2x^\mu}{d\lambda^2} + \Gamma^\mu_{\nu\rho}\frac{dx^\nu}{d\lambda}\frac{dx^\rho}{d\lambda} = 0, \tag{1.8}$$

where $\Gamma^\mu_{\nu\rho}$ are the *Christoffel symbols* of the Levi-Civita connection. In practice, one solves the four equations present in (1.8)[7] for the functions x^μ to obtain the parametrized trajectory. However, we can also use Eq. (1.4) to obtain information about the dynamics of the particles

[5]The weaker condition $u^\nu\nabla_\nu u^\mu = \sigma u^\mu$, where σ is an arbitrary function of the curve, is enough to ensure the *parallel transport* of the vector u. However, by demanding that the vector u also maintains the same length along the curve, one obtains Eq. (1.7). We can always re-parametrize the curve so that the geodesic equation is given by (1.7); the corresponding parameter is known as an *affine parameter* and the geodesic is known as an *affinely parametrized geodesic*.

[6]The components of the covariant derivative of a vector a are: $\nabla_\mu a^\nu = \partial_\mu a^\nu + \Gamma^\nu_{\mu\rho}a^\rho$.

[7]Eq. (1.8) represents a system of four coupled ordinary differential equations, which can be solved analytically for simple cases.

moving along geodesics; we will follow this procedure in Section 1.3.1 to determine the orbits of massive test particles moving around a Schwarzschild BH.

A particularly important procedure to simplify the problem of calculating geodesics is to find *conserved quantities*. In GR we can find these quantities by identifying *symmetry transformations* of the metric g, also known as *isometries*. The basic idea is to find a vector field ξ such that the metric does not change when it "moves" along this vector field. In mathematical terms, the vector field ξ induces a diffeomorphism of the manifold into itself, $\Phi_\xi : M \to M$, such that

$$\pounds_\xi g = 0, \tag{1.9}$$

where $\pounds_\xi$ is the *Lie derivative* with respect to ξ (see e.g. Appendix C of Wald (1984) for a discussion of the Lie derivative). The diffeomorphism Φ_ξ carries the metric g along the vector field ξ, and Eq. (1.9) means that Φ_ξ is an isometry. A vector field satisfying Eq. (1.9) is known as a *Killing vector field*. In local coordinates, we can rewrite this equation as

$$\nabla_\mu \xi_\nu + \nabla_\nu \xi_\mu = 0, \tag{1.10}$$

which is known as the *Killing equation*. The importance of Killing vector fields is that they induce a conserved quantity, given by $\xi_\mu u^\mu$, along a geodesic, where u^μ are the components of the tangent vector. To prove that $\xi_\mu u^\mu$ is conserved along the geodesic, we consider

$$u^\mu \nabla_\mu (\xi_\nu u^\nu) = u^\mu u^\nu \nabla_\mu \xi_\nu + \xi_\nu u^\mu \nabla_\mu u^\nu. \tag{1.11}$$

The first term vanishes because it is a contraction of a symmetric tensor ($u^\mu u^\nu$) with an anti-symmetric tensor [$\nabla_\mu \xi_\nu$; see Eq. (1.10)], and the second term vanishes due to the geodesic equation (1.7). Therefore $u^\mu \nabla_\mu (\xi_\nu u^\nu) = 0$ and $\xi_\mu u^\mu$ is conserved along the geodesic.

There is an easy way to identify Killing vector fields given the components of the metric. This method uses the fact that in a local coordinate system adapted to a Killing vector field ("adapted" means that the parameter along the integral curves of ξ is chosen as one of the coordinates, say x^1, so that $\xi^\mu = (\partial/\partial x^1)^\mu$), we have

$$\pounds_\xi g_{\mu\nu} = \frac{\partial g_{\mu\nu}}{\partial x^1}. \tag{1.12}$$

Therefore, if the components $g_{\mu\nu}$ do not depend on a certain coordinate, then we can associate a Killing vector field to that coordinate. This will be useful in the subsequent sections.

1.2 Historical account of Black Holes

BHs are regions of space-time where the effects of gravity are so strong that the region itself is *causally disconnected* from the rest of the Universe: events occurring inside the BH are invisible to the outside Universe, and the frontier is commonly known as the *event horizon* (see e.g. Wald 1984 for a formal mathematical definition of the concept of BH). Not even light can escape the tremendous gravitational field of the BH, which explains its name. The concept of BH was envisaged by Laplace as early as 1795, who noted that light (composed by corpuscles, as Newton suggested) could not escape from a sufficiently massive and compact object, according to Newton's gravitational theory. However, this early idea of BHs was forgotten due to the success of the wave theory of light. The journey of the BH concept continued with the discovery of the first exact solution to Einstein's field equations, found by Schwarzschild (1916), which described the gravitational field surrounding a spherical mass. Nevertheless, nobody knew at that time that Schwarzschild's solution was a unique and complete description of the external gravitational field of a spherical, electrically neutral, stationary and non-rotating BH, as proved by Birkhoff's theorem (Birkhoff 1923). Following Schwarzschild's work, people started searching for more solutions to Einstein's field equations. In particular, Reissner (1916) and Nordström (1918) (also Weyl 1917 and Jeffery and Filon 1921) discovered independently the electrically charged generalization of Schwarzschild's solution (the *Reissner-Nordström metric*) by solving the coupled system of Einstein's field equations and Maxwell's equations in vacuum (an *electrovacuum* solution).

The studies on the ultimate fate of stars were crucial in the development of the BH concept. Relativistic modeling of stars in their last stages of life shown the existence of *upper mass limits* (Chandrasekhar 1931). Dying stars with greater masses than the allowed by the upper limits, do not have enough internal pressure to counteract its own gravitational attraction. Hence, these stars become unstable and undergo complete *gravitational collapse* (Chandrasekhar 1957). The endpoint of this collapse will be a BH space-time, as first shown by Oppenheimer and Snyder (1939) with a numerical modeling. Further studies on the physical plausibility of gravitational collapse were done by John Wheeler and his collaborators (Harrison et al. 1965); in fact, it was Wheeler who coined the term "black hole" (Wheeler 1968). These investigations added more and more credibility to the concept of BH as a physical entity.

More rigorous studies of the concept of BH started in the 1960s. On the mathematical side, Kruskal (1960) and Szekeres (1960) gave an extension of the Schwarzschild solution which allowed us to better understand the interior of a BH, and allowed us to suspect that the complete gravitational collapse of a spherical body always produces a Schwarzschild BH. In fact, Penrose (1969) showed that there are mathematical reasons to believe that complete

gravitational collapse of non-spherical configurations will also lead to the formation of a BH space-time. At the same decade, Kerr (1963) found another vacuum solution to Einstein's field equations representing a rotating, stationary BH (the *Kerr metric*) and Newman et al. (1965) calculated the charged generalization of the Kerr metric by solving the Einstein-Maxwell field equations. This *Kerr-Newman geometry* is known to be a unique and complete description of the external gravitational and electromagnetic fields of a stationary BH (see e.g. the review by Adamo and Newman 2014). At sufficiently large times, one could expect that the space-time geometry surrounding a BH should settle down into a stationary state. Therefore, the assumption of stationarity in the aforementioned BH solutions is well supported on physical grounds. In contrast, a charged BH in an astrophysical environment would neutralize rapidly due to the presence of electrical charges in interstellar media. Consequently, *the Kerr BH is the most astrophysically relevant solution*. However, due to its simplicity, the Schwarzschild solution has been the preferred option for starting works and/or new ideas.

Besides the mathematical and physical motivation of the existence of BHs, people started to collect observational evidence of BHs (see e.g. Ashtekar et al. 2015). The discovery of compact X-ray sources (Giacconi et al. 1962; see also Chapter 13 of Shapiro and Teukolsky 1983 for an historical account of observations of compact X-ray sources), quasars (Schmidt 1963), and pulsars (Hewish et al. 1968) also motivated the thorough study of BHs. Particularly, the binary X-ray source *Cygnus X-1* discovered in 1964 was the first astronomical object widely accepted to be a BH (see e.g. Oda 1977). Apart from these electromagnetic observations, the recent detections of *gravitational waves* (ripples of space-time predicted by GR) have also greatly contributed to our confidence of the existence of BHs.[8]

After all the mathematical and observational studies of the past years, today BHs are universally recognized as real entities in our Universe. With this motivation, in the following sections we are going to study the simplest BH: the Schwarzschild solution.

1.3 Schwarzschild space-time

As we mentioned in the previous section, the static gravitational field outside a spherical object is uniquely described by the *Schwarzschild metric*. To obtain this solution, one can substitute the ansatz (1.3) (with $g_{tr} = g_{rt} = 0$ for a static solution) into the Einstein's field equations, and solve the resulting differential equations.[9] This standard procedure can be consulted for

[8] See The LIGO Scientific Collaboration et al. (2021) for a catalog of the latest detections of compact binary coalescences by LIGO, Virgo and KAGRA collaborations. Also, see https://www.ligo.org/detections.php for the full list of GW detections.

[9] In fact, solving Eintein's field equations in vacuum is easier. Contracting Eq. (1.1) in vacuum with $g^{\mu\nu}$, we obtain $R = 0$. Thus, the field equations simplify to $R_{\mu\nu} = 0$.

example in Wald (1984). The resulting line element is

$$ds^2 = -\alpha(r)^2\,dt^2 + \alpha(r)^{-2}\,dr^2 + r^2\left(d\theta^2 + \sin^2\theta d\phi^2\right), \tag{1.13}$$

with

$$\alpha(r) \coloneqq \sqrt{1 - \frac{r_S}{r}} \qquad \text{and} \qquad r_S \coloneqq \frac{2GM}{c^2}, \tag{1.14}$$

where r_S is called the *Schwarzschild radius* and M is an integration constant which can be identified as the mass of the object. This metric has a *coordinate singularity* at $r = r_S$ (the event horizon), which can be removed by writing the metric in other coordinates, for example, in Eddington–Finkelstein coordinates (Wald 1984). However, we will stick to the standard Schwarzschild coordinates because we are interested in the dynamics of particles moving outside the event horizon.

With the Schwarzschild metric we can calculate important physical aspects, such as conserved quantities and the geodesics of the space-time. This is a very important subject because it allows us to study the behavior of particles surrounding the BH, and in this way we can test the predictions of GR. For example, we can analyze the deflection of light rays (particles with no mass) or the orbits of massive test particles (particles with sufficiently small mass such that it does not alter significantly the space-time). The latter option will be the topic of the next section and it will be fundamental for understanding the process of general relativistic astrophysical accretion.

From the line element (1.13) we can immediately see that there are at least[10] two Killing vector fields in the Schwarzschild space-time, given by

$$(\xi^\mu_{(t)}) = (1,0,0,0) \qquad \text{and} \qquad (\xi^\mu_{(\phi)}) = (0,0,0,1), \tag{1.15}$$

which are associated to time and azimuthal symmetry, respectively. As we saw in Section 1.1, we can construct conserved quantities along a geodesic with the Killing vector fields. To this end, we consider an affinely parametrized geodesic $x^\mu = x^\mu(\lambda)$ with tangent vector $u^\mu = dx^\mu/d\lambda$. The associated conserved quantities along the geodesics are related to the energy per unit mass[11]

$$-\frac{E}{mc} \coloneqq \xi_{(t)\mu}u^\mu = g_{\mu\nu}\xi^\nu_{(t)}u^\mu = g_{\mu t}u^\mu = -\alpha(r)^2 u^t = -\left(1 - \frac{r_S}{r}\right)u^t, \tag{1.16}$$

[10] There are another two Killing fields associated to spherically symmetric space-times, see e.g. Carroll (2004).

[11] To identify the quantity $\xi_{(t)\mu}u^\mu$ in terms of the energy E, one can analyze the flat-space limit in which $\alpha(r) \to 1$. Since $u^t = c\,dt/d\tau$ for massive particles, then $\xi_{(t)\mu}u^\mu$ must be equal to $-E/mc$ to recover the famous formula $E = mc^2\,dt/d\tau$, where $dt/d\tau$ is identified with the Lorentz factor in flat space-time.

and the magnitude of the angular momentum[12]

$$\frac{L}{m} := \xi_{(\phi)\mu} u^\mu = g_{\mu\nu} \xi^\nu_{(\phi)} u^\mu = g_{\mu\phi} u^\mu = r^2 u^\phi, \tag{1.17}$$

where in the last step we have used the conservation of angular momentum (due to the spherical symmetry) to restrict the motion to the $\theta = \pi/2$ plane, so that $L_z = L$, where L_z is the angular momentum in the z-direction and L is the total angular momentum.

We can write the conserved quantities E and L in terms of the four-momentum $p^\mu = m u^\mu$ to get rid of the mass dependence. The corresponding expressions are

$$E = \alpha(r)^2 c\, p^t, \tag{1.18}$$

$$L = r^2\, p^\phi, \tag{1.19}$$

and they can be applied to particles with no mass, such as photons.

With Eq. (1.18) we can obtain the *minimum possible energy* that a particle can have at radius $r = R$. Using the on-shell restriction (1.6) with zero spatial momenta (the minimum possible energy will be achieved when the particle is instantaneously at rest), we get

$$-m^2c^2 = g_{tt}(p^t)^2 \qquad \rightarrow \qquad p^t = \frac{mc}{\alpha(R)}. \tag{1.20}$$

Therefore, substituting Eq. (1.20) in (1.18) we obtain

$$E_{\min}(R) = \alpha(R)\, mc^2. \tag{1.21}$$

Note that in the limit $R \to \infty$ we recover the energy for non-relativistic particles (particles with speed much less than the speed of light) given by $E = mc^2$.

1.3.1 Test particle motion

Massive particles moving in geodesics parametrized by proper time obey the condition (1.4), which can be expanded as

$$-c^2 = -\alpha(r)^2 c^2 \dot{t}^2 + \alpha(r)^{-2} \dot{r}^2 + r^2 \dot{\phi}^2, \tag{1.22}$$

[12] By dimensional analysis, the conserved quantity $\xi_{(\phi)\mu} u^\mu$ will be equal to L/m.

where we have used that the particle is moving in the $\theta = \pi/2$ plane, and we have defined $\dot{t} := dt/d\tau$ and $\dot{\phi} := d\phi/d\tau$. Using Eqs. (1.18) and (1.19) in (1.22), we obtain

$$\frac{1}{2}\dot{r}^2 + V_{\text{clas}}(r) = \mathscr{E}, \tag{1.23}$$

with

$$V_{\text{clas}}(r) := \frac{1}{2}\alpha(r)^2\left(c^2 + \frac{L^2}{m^2r^2}\right) \qquad \text{and} \qquad \mathscr{E} := \frac{E^2}{2m^2c^2}. \tag{1.24}$$

Eq. (1.23) is precisely the equation for a classical particle of unit mass and energy $\mathscr{E}$ moving under the effective potential V_{clas}. Note that

$$V_{\text{clas}}(r) = \frac{c^2}{2} - \frac{GM}{r} + \frac{L^2}{2m^2r^2} - \frac{GML^2}{m^2r^3}. \tag{1.25}$$

In this expression the first term is a constant, the second term is the Newtonian gravitational potential, the third term is a contribution from angular momentum which also appears in Newtonian gravity (it is known as the *centrifugal potential*), and the fourth term is a contribution solely from GR which makes a great difference with respect to the Newtonian case for small r.

We can rewrite Eq. (1.23) to obtain an effective potential with the same units as E^2. The corresponding expression is

$$m^2c^2\dot{r}^2 + V_L(r) = E^2, \tag{1.26}$$

where

$$V_L(r) := c^2\alpha(r)^2\left(m^2c^2 + \frac{L^2}{r^2}\right). \tag{1.27}$$

In terms of the radial momentum p^r, we get

$$(p^r)^2 = \frac{E^2 - V_L(r)}{c^2}. \tag{1.28}$$

As in Classical Mechanics, we can get a qualitative description of the particle dynamics by analyzing the behavior of the potential $V_L(r)$. First, we rewrite Eq. (1.27) as

$$\frac{V_L(r)}{m^2c^4} = \left(1 - \frac{1}{\mathfrak{r}}\right)\left(1 + \frac{\ell^2}{\mathfrak{r}^2}\right), \tag{1.29}$$

where

$$\mathfrak{r} := \frac{r}{r_{\text{S}}} \qquad \text{and} \qquad \ell := \frac{Lc}{2GMm}. \tag{1.30}$$

A standard procedure to calculate the requirements for having circular orbits is to find the maxima of the effective potential. Therefore, differentiating Eq. (1.29) with respect to $\mathfrak{r}$ we

find the quadratic equation for the maxima

$$\mathfrak{r}^2 - 2\ell^2\mathfrak{r} + 3\ell^2 = 0, \tag{1.31}$$

whose solutions are

$$\mathfrak{r}_\pm = \ell^2 \pm \ell\sqrt{\ell^2 - 3}. \tag{1.32}$$

We observe that for $\ell^2 < 3$ there are no critical points, for $\ell^2 = 3$ there is just one critical point, and for $\ell^2 > 3$ there are two critical points. In Fig. 1.1 we show a plot of the effective potential for different values of ℓ.

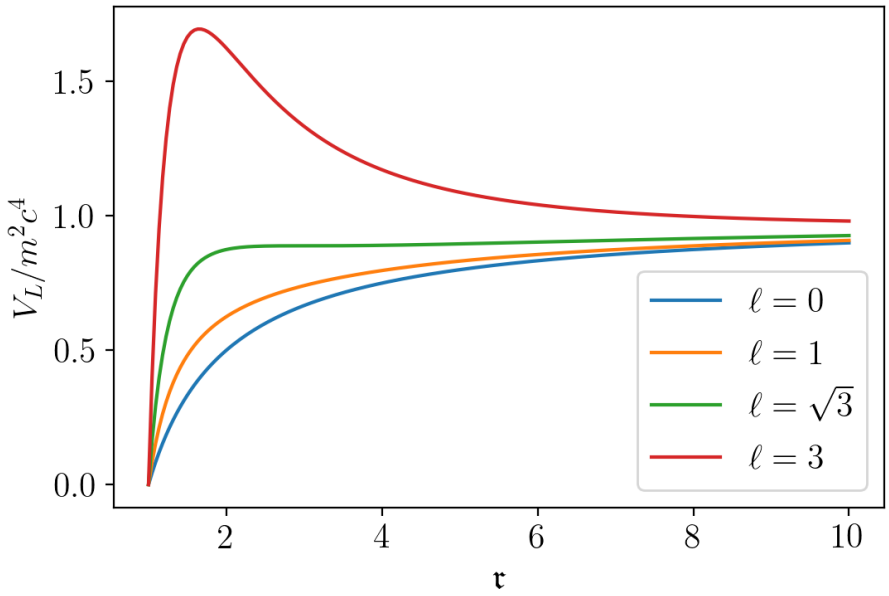

Fig. 1.1 Effective potential (1.29) for massive test particles moving in a Schwarzschild space-time as a function of $\mathfrak{r} = r/r_S$ for different values of $\ell = Lc/2GMm$ [see Eq. (1.30)].

In the case $\ell^2 < 3$ there are no critical points and particles inevitably fall to the BH (see Fig. 1.1) since they do not have enough angular momentum to counteract the attraction of the BH. In the case $\ell^2 \geq 3$, we can differentiate Eq. (1.29) twice and evaluate the solutions (1.32) to find that $\mathfrak{r}_-$ is a maximum and $\mathfrak{r}_+$ is a minimum of the effective potential (see Fig. 1.2). Hence, we can associate *stable circular orbits* to $\mathfrak{r}_+$, and *unstable circular orbits* to $\mathfrak{r}_-$. However, note that the minimum possible value of $\mathfrak{r}_+$ is achieved when $\ell^2 = 3$. The corresponding value is known as the radius of the *innermost stable circular orbit* (ISCO), and its explicit expression is given by

$$\mathfrak{r}_{+,\mathrm{ISCO}} = 3 \qquad \longleftrightarrow \qquad r_{\mathrm{ISCO}} = 3r_S = \frac{6GM}{c^2}. \tag{1.33}$$

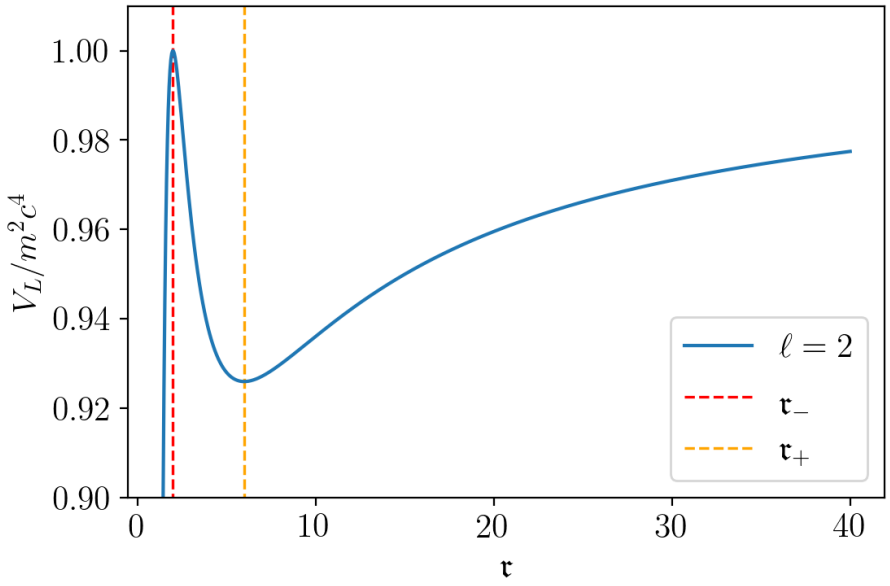

Fig. 1.2 Effective potential (1.29) for massive test particles moving in a Schwarzschild space-time as a function of $\mathfrak{r} = r/r_S$ for $\ell = 2 > \sqrt{3}$. In this case, we can observe with great detail the maximum and minimum of the effective potential which are given by Eq. (1.32).

The associated angular momentum of a particle on the ISCO is

$$\ell_{\text{ISCO}} = \sqrt{3} \qquad \longleftrightarrow \qquad L_{\text{ISCO}} = \frac{\sqrt{12}GMm}{c}, \tag{1.34}$$

and the energy of a particle moving on the ISCO is

$$E_{\text{ISCO}} = \frac{2\sqrt{2}mc^2}{3}, \tag{1.35}$$

which can be obtained by substituting Eqs. (1.33) and (1.34) in (1.26) with $\dot{r} = 0$.

Observe in Eq. (1.32) that there is no upper bound to the possible values of $\mathfrak{r}_+$. Hence, the stable circular orbits are restricted to the interval

$$\mathfrak{r}_+ \in (3, \infty) \qquad \longleftrightarrow \qquad r_+ \in \left(\frac{6GM}{c^2}, \infty\right). \tag{1.36}$$

Additionally, note that the minimum possible value of $\mathfrak{r}_-$ is achieved when $\ell \to \infty$, in which case $\mathfrak{r}_- \to 3/2$. Therefore, the unstable circular orbits (or the radius of the maximum of the effective potential) are restricted to the interval

$$\mathfrak{r}_- \in \left(\frac{3}{2}, 3\right) \qquad \longleftrightarrow \qquad r_- \in \left(\frac{3GM}{c^2}, \frac{6GM}{c^2}\right). \tag{1.37}$$

1.3.2 Absorbed and scattered particles

In this work we are interested in the accretion from finite radius of massive test particles onto a Schwarzschild BH. In other words, we want to know the behavior of particles that are *injected* from a sphere of radius R. To explain the dynamics of such scenario, we will apply some of the results of the previous section. Our objective will be to characterize the possible energies and angular momenta that are relevant to the accretion problem.

First, for $L \leq L_{\mathrm{ISCO}}$, there are no critical points of $V_L(r)$. In fact, we can see from Fig. 1.1 that, in this case, $V_L(r)$ is a monotonously increasing function of r, which means that *any infalling particle whose total angular momentum lies in this range inevitably falls into the BH* within a finite amount of its proper time.

For $L > L_{\mathrm{ISCO}}$, the function $V_L(r)$ has a local maximum which is inside the interval $(3GM/c^2, 6GM/c^2)$, and a local minimum lying in the interval $(6GM/c^2, \infty)$. *Whether or not an infalling particle released from $r = R$ with $L > L_{ISCO}$ falls into the BH depends on its energy* (see Eq. (1.26) and Fig. 1.3). If E^2 is larger than the maximum of the potential, then the particle is absorbed by the BH; otherwise it bounces off the centrifugal barrier and is reflected towards $r = R$.

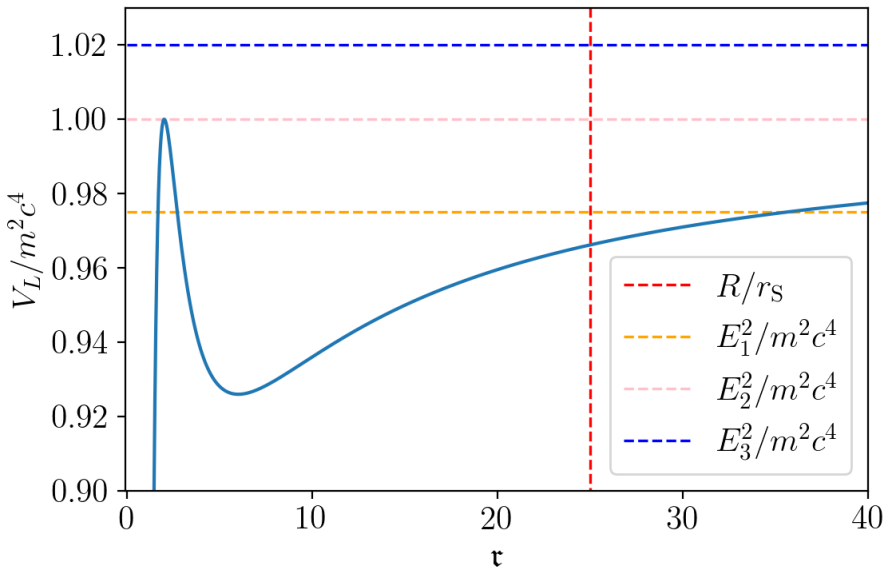

Fig. 1.3 Effective potential (1.29) for massive test particles moving in Schwarzschild space-time as a function of $\mathfrak{r} = r/r_{\mathrm{S}}$ for $\ell = 2 > \ell_{\mathrm{ISCO}}$. An infalling particle is released from $r = R$. We consider three particle energies of the infalling particle. When $E = E_1$ the particle bounces off the centrifugal barrier, however, when $E = E_3$ the particle falls into the BH. The limiting case is represented by a particle with energy $E = E_2$, whose squared value coincides with the maximum of the effective potential.

In fact, if the particle has a fixed energy E^2, we can calculate the angular momentum such that the maximum of its effective potential coincides with E^2 (see the pink horizontal dashed

line in Fig. 1.3). We know from Eq. (1.32) that the maximum of the effective potential is at $\mathfrak{r} = \mathfrak{r}_-$. Therefore, the condition

$$V_{L_c}(\mathfrak{r}_-) = E^2, \tag{1.38}$$

determines the *critical angular momentum* L_c such that the maximum of its potential is equal to E^2. In this way, substituting Eqs. (1.29) and (1.32) into Eq. (1.38), and solving for L_c with the software *Mathematica*[13] we find

$$L_c(E) = \frac{4\sqrt{2}GMm^3c^3}{\sqrt{36m^2c^4E^2 - 8m^4c^8 - 27E^4 + E(9E^2 - 8m^2c^4)^{3/2}}}, \tag{1.39}$$

valid for $E \geq E_{\rm ISCO}$ (otherwise there would be no critical points of the effective potential), with $L_c(E_{\rm ISCO}) = L_{\rm ISCO}$. Note that as E increases from $E_{\rm ISCO}$ to ∞, $L_c(E)$ increases from $L_{\rm ISCO}$ to ∞, because the maximum of the potential grows with the value of the angular momentum. Additionally, for non-relativistic particles ($E = mc^2$) we have $L_c(mc^2) = 4GMm/c$.

There is another particular value of the angular momentum relevant to the problem of accretion from finite radius. From Fig. 1.1 we can see that if the angular momentum increases, then the effective potential also increases for all the values of $\mathfrak{r}$. Therefore, if a particle is injected at radius R with a fixed energy E^2 (see e.g. the vertical red and the horizontal orange dashed lines in Fig. 1.3), then there will be a *maximum* angular momentum such that greater values of the angular momentum will produce an effective potential greater than E^2 at R, leading to imaginary velocities [see Eq. (1.26)]. The condition that determines this maximum value $L_{\rm max}$ is

$$V_{L_{\rm max}}(R) = E^2. \tag{1.40}$$

Thus, using Eq. (1.29) and solving for $L_{\rm max}$ we find

$$L_{\rm max}(E,R) = mcR\sqrt{\frac{E^2}{m^2c^4\alpha(R)^2} - 1}. \tag{1.41}$$

In Chapter 4 we will be interested in the possible values of the angular momentum as a function of the energy and the injection radius to calculate the accretion rate of particles accreting onto a Schwarzschild BH. From Eq. (1.26) we can see that the possible energies for particles released from $r = R$ with angular momentum L satisfy $\sqrt{V_L(R)} \leq E < \infty$. However, since $V_L(R)$ increases as a function of L, then the minimum possible energy [cf. Eq. (1.21)] is

[13] The computations in this work were done with Wolfram Mathematica, version 13.0.0 (https://www.wolfram.com/mathematica).

obtained when there is no angular momentum. Therefore, the interval

$$\sqrt{V_{L=0}(R)} = \alpha(R)\,mc^2 = E_{\min} \leq E < \infty, \tag{1.42}$$

will be the relevant energy range for describing an accretion scenario from finite radius as we will see in Section 4.2. Furthermore, by analyzing the behavior of $L_{\rm c}(E)$ and $L_{\max}(E,R)$ as functions of E we find

$$L_{\max}(E,R) < L_{\rm c}(E) \qquad \text{for} \qquad \alpha(R)\,mc^2 \leq E < E_{\rm c}(R), \tag{1.43}$$

$$L_{\rm c}(E) < L_{\max}(E,R) \qquad \text{for} \qquad E_{\rm c}(R) < E, \tag{1.44}$$

where $E_{\rm c}(R)$ is a *critical energy* such that $L_{\max}(E_{\rm c},R) = L_{\rm c}(E_{\rm c})$; equating the expressions (1.39) and (1.41), and solving for $E_{\rm c}$, we obtain (see also *Gabarrete and Sarbach, paper in preparation*)

$$E_{\rm c}(R) = mc^2 \frac{R + r_{\rm S}}{\sqrt{R(R+3r_{\rm S})}}. \tag{1.45}$$

With the formulae that we have developed, we can characterize the conditions under which particles are absorbed or scattered by the BH. Basically, *particles are absorbed when the square of the particle's energy is larger than the maximum of the effective potential*. If $E = E_{\min} = \alpha(R)\,mc^2$, then the only possible value for the angular momentum is $L = 0$ (see blue curves in Fig. 1.4). Next, if $E_{\min} < E < E_{\rm c}(R)$, then the possible values of the angular momentum of absorbed particles are $0 \leq L \leq L_{\max}(E,R)$ (see red curves in Fig. 1.4). Finally, if $E = E_{\rm c}(R)$, then absorbed particles satisfy $0 \leq L \leq L_{\max}(E,R) = L_{\rm c}(E)$ (see pink curves in Fig. 1.4). On the other hand, *particles are scattered when the square of the particle's energy is smaller than the maximum of the effective potential*. If $E = E_{\rm c}(R)$, then scattered particles have $L = L_{\max}(E,R) = L_{\rm c}(E)$ (see pink curves in Fig. 1.5), and if $E > E_{\rm c}(R)$, then the scattered particles should have $L_{\rm c}(E) < L < L_{\max}(E,R)$ (see orange curves in Fig. 1.5).

Summarizing, we have the following characterization which we will use in Chapter 4:

1. *Absorbed particles*

$$\begin{cases} \alpha(R)\,mc^2 \leq E < E_{\rm c}(R) \quad \text{and} \quad 0 \leq L \leq L_{\max}(E,R), \\ E_{\rm c}(R) < E < \infty \quad \text{and} \quad 0 \leq L < L_{\rm c}(E). \end{cases}$$

2. *Scattered particles*

$$E_{\rm c}(R) \leq E < \infty \quad \text{and} \quad L_{\rm c}(E) < L < L_{\max}(E,R).$$

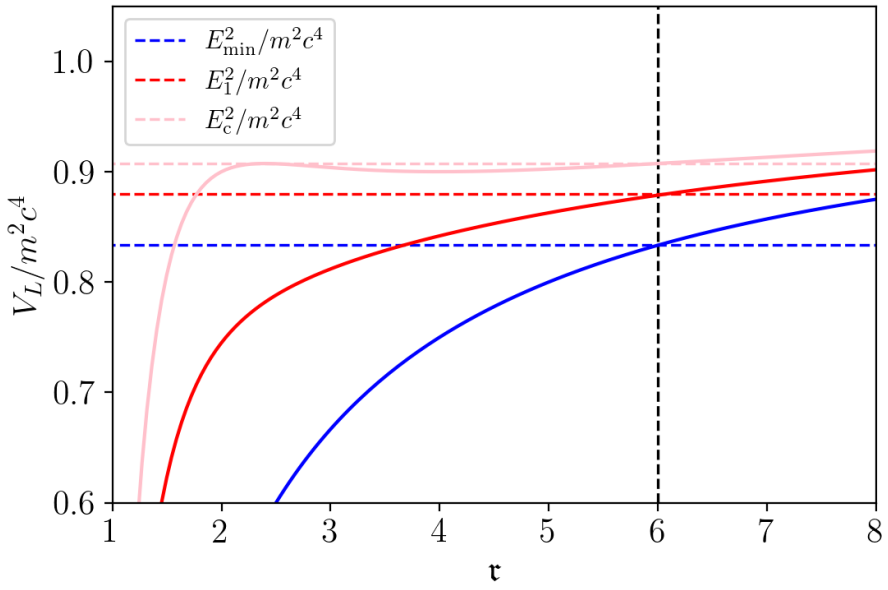

Fig. 1.4 Characterization of absorbed particles. We choose three particle energies: the minimum possible energy $E^2 = E^2_{\rm min}$ (dashed blue), an energy $E^2 = E^2_1 < E^2_{\rm c}$ (dashed red), and an energy $E^2 = E^2_{\rm c}$ (dashed pink). We plot the effective potentials (1.29) for a massive test particle released from $r = R = 6\,r_{\rm S}$ with $L = 0$ (solid blue), $L = L_{\rm max}(E_1, R) < L_{\rm c}(E_1)$ (solid red), and $L = L_{\rm max}(E_{\rm c}, R) = L_{\rm c}(E_{\rm c})$ (solid pink).

Finally, for the problem of accretion we will not consider particles with energies lower than $\sqrt{V_L(R)}$ since they correspond to bound trajectories whose turning points r_i satisfy $r_{\rm S} < r_1 < r_2 < R$ (see Fig. 1.6), and hence they do not affect the value of the accretion rate (because they are not absorbed by the BH), nor they contribute to the particle number density at $r = R$, which will be a quantity relevant to our computations of Chapter 4.

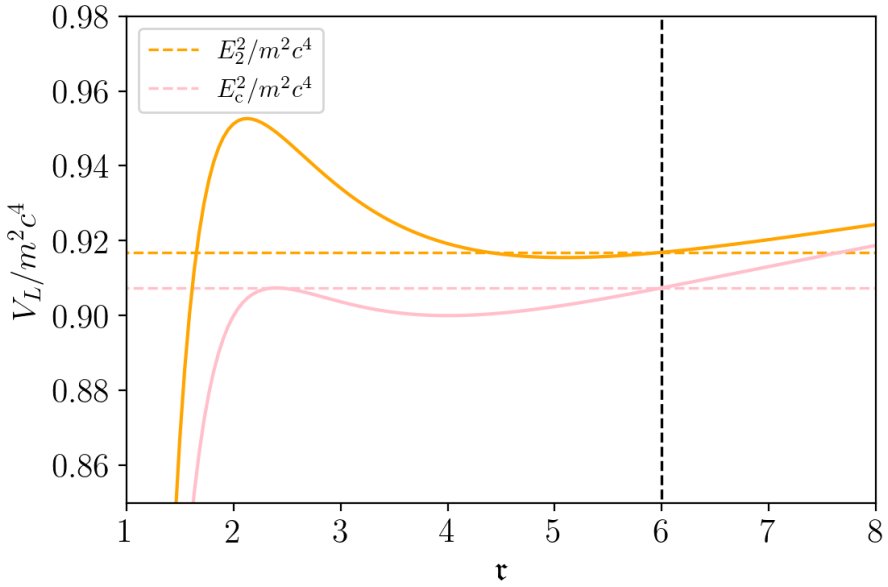

Fig. 1.5 Characterization of scattered particles. We choose two particle energies: an energy $E^2 = E_c^2$ (dashed pink), and an energy $E^2 = E_2^2 > E_c^2$ (dashed orange). We plot the effective potentials (1.29) for a massive test particle released from $r = R = 6\,r_S$ with $L = L_{max}(E_c, R) = L_c(E_c)$ (solid pink) and $L = L_{max}(E_2, R) > L_c(E_2)$ (solid orange).

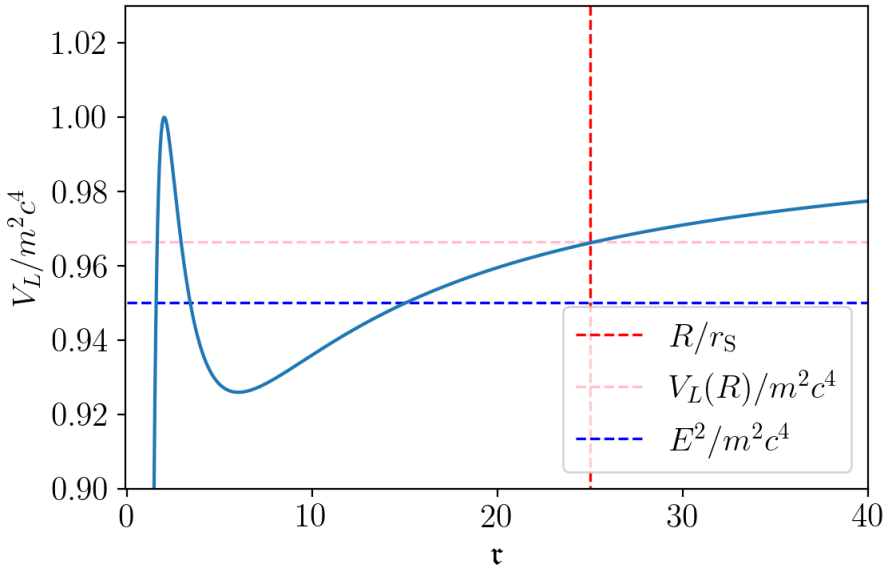

Fig. 1.6 Particles with energy $E < V_L(R)$ (blue dashed line) give rise to bounded trajectories which do not contribute to the accretion rate nor to the particle number density at $r = R$.

Chapter 2

Astrophysical accretion

Accretion is the process by which astrophysical objects gravitationally capture ambient matter which may come from the ubiquitous interstellar gases and/or from orbital companion stars. This mechanism has a fundamental role in the formation and development of galaxies, stars, planets, neutron stars (NSs) and BHs due to the attractive nature of gravity.

Particularly, the accretion onto compact objects[1] (COs) is an important mechanism for astrophysics and observational cosmology, since it is a powerful and natural process for producing detectable high-energy radiation. In fact, the accretion process has been recognized as the principal source of power in several types of binary systems, active galactic nuclei (AGN) and quasars (see e.g. Frank et al. 2002). Therefore, modeling the accretion mechanism is an extremely important task needed to understand the evolution of compact objects.

In this chapter we will describe basic concepts and how can we model the accretion process (Sec. 2.1). Then, we will briefly review the Bondi hydrodynamic spherical accretion model which is widely used to give a crude estimation of the accretion rate (Sec. 2.2). Since in this work we are interested in the accretion onto BHs, we will also discuss the types of flows present in this scenario (Sec. 2.3). Furthermore, we are going to review the current models and methods that are used to estimate the accretion rate onto the supermassive black holes (SMBHs) Sgr A* and M87* (Sec. 2.4). Finally, we will discuss the breakdown of the hydrodynamic approximation for certain astrophysical scenarios and motivate the need of a kinetic approach (Sec. 2.5).

[1] Compact objects are bodies whose mass M is concentrated in a very small region R. The compactness can be characterized, for example, by the parameter $\mathscr{C} = GM/Rc^2$. Examples of these objects are white dwarfs, NSs and BHs (which are the most compact objects, with $\mathscr{C} = 1/2$).

2.1 Fundamentals of astrophysical accretion

The energy coming from accretion is sourced by the extraction of gravitational potential energy of the accreting matter. Using Newtonian gravitation, we can estimate the energy that a particle with mass m releases when it accretes onto a central object with mass M and radius R. The change in gravitational potential energy of this particle is

$$\Delta E = \frac{GMm}{R} = G\xi m, \tag{2.1}$$

where $\xi := M/R$ is the *compactness parameter* of the accreting object. We thus see that the efficiency of accretion as a source of energy is directly proportional to ξ. Hence, BHs (which are the most compact objects) are great extractors of the energy stored in the accreting matter.

In falling through the steep gravitational potential of a CO, the gas is heated due to its friction in a process known as *viscous heating*, in which the viscous forces on the gas dissipate the kinetic energy of the particles into chaotic thermal motions. The associated densities and temperatures of the gas surrounding the CO, transform the flow into a *plasma* composed by electrons and ions. The large accelerations of the electrons cause the emission of high-frequency electromagnetic (EM) radiation. In fact, there is a conversion of roughly 10% of the accreted rest-mass energy into radiation and jets/outflows. Remarkably, this efficiency is considerably larger than that obtained by other astrophysical processes (e.g. nuclear fusion) (Frank et al. 2002; Shapiro and Teukolsky 1983).

2.1.1 Eddington and accretion luminosities

In general, the emitted radiation will transfer its momentum to the accreting material by scattering and absorption processes. Thus, in principle, the net rate at which matter is accreted (i.e. the *mass accretion rate*) will depend on the radiation field, which is naturally related to the *luminosity* (the measure of the EM power radiated by a light-emitting object over time) of the accreting object.[2]

Under specific circumstances, the luminosity has a maximum value for a given mass of the accreting object. This bound is known as the *Eddington limit* or *Eddington luminosity*, and it basically represents the *balance* between the radiation pressure and the gravitational pull (exerted by the central object) affecting the ions in the accreting plasma. To obtain an order-of-magnitude estimation of this limit, we consider the steady, spherically symmetrical accretion of a fully ionized hydrogen gas (composed of protons and electrons with masses m_{p}

[2] We are referring here to the light emitted by the accreting material (or accreting *flow*). In this sense, we can talk about the luminosity of a BH (which does not emit light by itself).

and m_e, respectively) onto a central object of mass M. The radiation pressure (average force per unit area) is given by $P_{rad} = S/c$, where S is the average of the Poynting vector which represents the energy flux density (energy per unit area, per unit time) transported by the EM fields (Griffiths 2013). If we use the non-relativistic approximation, the radiation pressure will affect mainly the free electrons in the gas through *Thomson scattering*.[3] Therefore, if $\sigma_T = 6.7 \times 10^{-25}\,\mathrm{cm}^2$ is the Thomson cross-section for electrons, then the radial force exerted in these particles will be $F_{rad} = \sigma_T P_{rad} = \sigma_T S/c$. The spherical symmetry and the definitions of L and S imply that $S = L/(4\pi r^2)$, where r is the radial distance from M to the electron. Hence, the final expression for the radial force exerted by the radiation on the electrons will be $F_{rad} = L\sigma_T/(4\pi r^2 c)$.[4] On the other hand, the gravitational force on a electron-proton pair is simply given by $F_g = GM(m_p + m_e)/r^2 \approx GMm_p/r^2$. In this way, the condition $F_{rad} = F_g$ allows us to calculate the Eddington luminosity for this idealized system,

$$L_{Edd} = \frac{4\pi GMm_p c}{\sigma_T} \approx 1.3 \times 10^{38} (M/M_\odot)\,\mathrm{erg\,s^{-1}}. \tag{2.2}$$

If there would be a greater luminosity (that is, a greater radiation pressure) then the accretion would be halted in this system.

Despite the employed assumptions in this highly idealized case, the Eddington luminosity is of great astrophysical importance because there are systems which behave as *standard candles*, whose luminosities are close to their Eddington limits. Therefore, we can extract information about the properties of these systems just by studying their luminosities.

Another important concept is the *accretion luminosity* L_{acc}, which is the emitted power if all the kinetic energy of the infalling matter would be transformed to radiation at the stellar surface R. We can calculate the accretion luminosity by analyzing the change in time of Eq. (2.1) applied to a collection of particles. In this way, we obtain

$$L_{acc} = \frac{GM\dot{M}}{R}, \tag{2.3}$$

since the absorption of particles represents a gain of mass of the accreting object.

In the case of BH accretion, much of the accretion energy could disappear into the BH's event horizon, rather than be radiated. To account for this uncertainty in the amount of emitted radiation, we introduce a dimensionless parameter η, called the *efficiency*, on the right hand

[3] The radiation scattering cross-section σ of a charged free particle of mass m satisfies $\sigma \sim 1/m^2$ (Jackson 1998). Therefore, compared with protons, the electrons have a larger probability of scattering the radiation since $m_p \gg m_e$.

[4] The radiation mainly pushes the electrons, nevertheless the attractive Coulomb force between the electrons and protons makes the electrons to drag the protons with them.

side of Eq. (2.3)

$$L_{\rm acc} = \frac{2\eta GM\dot{M}}{R} = \eta \dot{M} c^2, \tag{2.4}$$

where we have introduced a factor of 2 associated with the definition of η, and we have used the expression of the Schwarzschild radius $R = r_{\rm S} = 2GM/c^2$. Eq. (2.4) measures how much of the accreted rest-mass energy is converted into radiation, and as we mentioned earlier, for several cases we have $\eta \sim 0.1 = 10\%$ (Frank et al. 2002).

2.1.2 Modeling the accretion process

From the previous discussions we can see that the accretion mechanism can be regarded as a highly important process in astrophysics, so how could we describe in detail the flow of accreting matter? To model an accretion flow, we must take into account several ingredients:

1. The type of **accreting object** and the **boundary conditions**.
   The accreting object could be a star, a NS or a BH, in a wide range of different masses. Each object has a distinct *inner* boundary condition at or near its surface associated to the matter and the atmosphere at those regions; in the case of BHs, there is a "vacuum cleaner" boundary condition due to the nature of the event horizon. In contrast, the *outer* boundary condition is determined by the properties of the accreting matter at large distances. See, for example, the treatment of accretion onto BHs, NSs and white dwarfs in Shapiro and Teukolsky (1983).

2. The **nature of the flow**.
   If the effective mean free path λ of the particles is sufficiently short with respect to the length ℓ over which macroscopic quantities (such as the temperature, the particle number density or the bulk velocity) vary in a significant way, then thermal equilibrium is obtained locally and we are dealing with a flow which can be treated with the *hydrodynamic* or *fluid approximation*. The behavior of this system is studied in terms of *fluid variables* (velocity, temperature, density, pressure, etc.) as functions of position and time, and the evolution is obtained by imposing the laws of conservation of mass, momentum and energy. In the opposite limit ($\lambda \gg \ell$) we need to use a *kinetic approximation* in which the macroscopic properties of the flow are calculated directly from the statistical behavior of many particles. This framework is known as *Kinetic Theory* and its core concept is the distribution function which evolves through the Boltzmann equation. An intermediate scenario ($\lambda \sim \ell$) can be modeled with the fluid approximation but needs to take into account effects from micro-physics. The choice between the hydrodynamic or kinetic approximation is usually made with regard to the physical properties of interest

for the system or with regard to numerical considerations. See e.g. Belmont et al. (2013) for a discussion of the fluid and kinetic approximations.

3. The **flow geometry**.
   The configuration that accreting matter acquires over time is highly dependent on the specific scenario. In general, the flow geometry depends on the flow symmetries and the angular momentum of the gas, which may produce a 2 or 3-dimensional flow. One of the most studied cases is when the matter spirals into the accreting object, developing an *accretion disk* around it (an *axisymmetric flow*); this flow can be *geometrically thin* if the typical scale height H of the disk in the axial direction is much less than the radial scale of the disk R (i.e. $H \ll R$), it can be a *slim disk* if $H \lesssim R$, or it can be a *geometrically thick* disk if $H \gg R$ (see e.g. Frank et al. 2002). Another case is the *spherical flow*, which arise when there is no mean motion of the gas in a certain direction.

4. The effects of **radiation**.
   Depending on the properties of the radiation field the flow may be *optically thick* (corresponding to an optical depth $\tau \gg 1$, so that photons are absorbed or scattered many times by the gas before escaping to infinity) or *optically thin* (with $\tau \ll 1$, so that radiation is scarcely reabsorbed by the gas and escapes almost freely once produced). Radiation processes (such as synchrotron emission, bremsstrahlung radiation and inverse Compton scattering) cool the accretion flow because they extract energy from the electrons and send it out from the system (see e.g. Rybicki and Lightman 1985 for a discussion of radiative processes in astrophysics). For optically thin plasmas (such as those present in *hot flows*; see Section 2.3), the impact of radiative cooling in the flow becomes less important. Nevertheless, for other kinds of flow the accretion modeling needs to include radiation effects self-consistently. In fact, the radiation field affects the *transport processes*, discussed next.

5. The **transport processes**.
   The microscopic structure of a plasma affects its macroscopic properties through *transport processes* (Zank 2014), such as thermal conductivity and viscosity. Generally, these processes become important when there are large gradients (e.g. of temperature or velocity) in the plasma. In particular, the dominant heating (viscous and compressional heating) and cooling (escaping of radiation) mechanisms determine the gas dynamics.

6. The presence of **magnetic fields**.
   Plasmas are electrically conducting gases, so they are susceptible to magnetic fields. Depending on the intensity, these fields may affect the dynamics of the flow, the transport

processes and the transfer of radiation (see e.g. Frank et al. 2002). The magnetic fields may originate from the accreting object itself (in the case of stars or NSs), or may come from external sources (such as orbital star companions).

7. The existence of **outflows** and **jets**.
   Some accretion flows have strong winds (matter outflows) and/or are related to astrophysical jets (Blandford and Begelman 1999; Narayan and Yi 1994; Yuan and Narayan 2014). The former are associated with a convective inward transport of angular momentum (see Section 2.3) and the latter are associated to the extraction of rotational energy from a central BH (Blandford and Znajek 1977) or from the accretion flow (Blandford and Payne 1982).

It should be clear by now that modeling the accretion process is a titanic task since there is a lot of complicated physics that needs to be included. In this work, we will treat very simple accretion scenarios in order to focus on the novel approach of modeling a kinetic accretion from finite radius. Particularly, in Chapter 4 we will consider the spherically symmetric accretion of a collisionless kinetic gas onto a Schwarzschild BH, with boundary conditions given at the Schwarzschild radius and at an external *injection sphere*. We are going to neglect the radiation field, transport processes, magnetic fields, outflows and jets. Furthermore, we will assume a gas composed only by ions since they have a much larger mass than electrons.

In the following, we will describe various models of hydrodynamical accretion and then we will briefly present their application to the SMBHs Sgr A* and M87*.

2.2 Bondi hydrodynamic spherical accretion

In some cases, Coulomb collisions between charged particles are not enough to couple the plasma particles effectively. Nevertheless, the presence of macroscopically weak magnetic fields and/or plasma collective effects, ensure that local equilibrium is attained with an effective mean free path that satisfies the hydrodynamic approximation, $\lambda \ll \ell$ (Belmont et al. 2013). In this way, *the fluid description is well-suited for a variety of common astrophysical scenarios* (such as the accretion of interstellar gases or the matter exchange between binary stars) where magnetic fields or plasma effects are significant.

The first treatment of the hydrodynamic accretion problem was done by Hoyle and Lyttleton (1939) who considered the accretion by a star moving at a steady speed through an infinite gas cloud; later on, Bondi and Hoyle (1944) extended this analysis (see e.g. Edgar 2004 for a review of this models). However, it was Bondi (1952) who first studied the hydrodynamic, spherical and steady flow of an infinite gas cloud accreting onto a point-like distribution

of mass M described by a Newtonian potential. Under this assumptions, one can use the continuity equation ($\nabla \cdot (\rho \mathbf{u}) = 0$, where ρ and $\mathbf{u}$ are the density and velocity of the gas cloud, respectively) in spherical coordinates to obtain the accretion rate

$$\dot{M} = 4\pi r^2 \rho u = \text{constant}. \tag{2.5}$$

To identify this constant we must use the Euler equation and specify boundary conditions. Particularly, for a *polytropic gas* (which satisfies $P = K\rho_{\text{a}}^{\gamma}$, where P is the gas pressure, K is a constant and γ_{a} is the adiabatic index) at rest at infinity (where the density is ρ_∞, the pressure is P_∞ and the sound speed,[5] defined by $a := (dP/d\rho)^{1/2} = (\gamma_{\text{a}} P/\rho)^{1/2}$, is a_∞), it can be shown that the integration of the Euler equation, together with the requirement that the flow does not have singularities, gives the *Bondi mass accretion rate* (Bondi 1952; see also Korol et al. 2016),

$$\dot{M}_{\text{B}} = 4\pi \lambda_{\text{a}} r_{\text{B}}^2 \rho_\infty a_\infty, \tag{2.6}$$

where λ_{a} is a function of the adiabatic index (for example, a monoatomic adiabatic process has $\gamma = 5/3$ and $\lambda_{\text{a}} = 1/4$), and r_{B} is the *Bondi radius* defined by

$$r_{\text{B}} = \frac{GM}{a_\infty^2}. \tag{2.7}$$

Assuming the equation of state for an ideal gas ($P = nk_{\text{B}}T$, where n is the numerical density of the gas and k_{B} is the Boltzmann constant), we obtain

$$a_\infty = \sqrt{\frac{\gamma k_{\text{B}} T_\infty}{m}}, \tag{2.8}$$

where T_∞ is the temperature of the gas at infinity. Therefore, the accretion rate in this model is related to the mass of the accreting object, the temperature of the flow (which is measured through EM observations) and the microscopic structure of the gas (which is contained in γ).

Strictly speaking, if the accreting object is a BH, then the accretion rate should be computed by means of a general relativistic calculation (see Appendix G of Shapiro and Teukolsky 1983). This was first done by Michel (1972) who studied the steady, spherical, hydrodynamical accretion of simple polytropic gases onto a Schwarzschild BH. However, if the gas is mainly composed by ionized hydrogen atoms with mass m_{p} (the proton mass) so that $\gamma_{\text{a}} \leq 5/3$, and the gas is at non-relativistic temperatures (such that $k_{\text{B}} T_\infty \ll m_{\text{p}} c^2$), the Newtonian calculation yields a very good approximation to the general relativistic case even if the central BH is

[5] The sound speed is the speed at which pressure disturbances travel through the gas. The sound speed limits the gas response to pressure changes.

rotating (see Aguayo-Ortiz et al. 2021 for the rotating case and other generalizations of the hydrodynamic solutions due Bondi and Michel). Therefore, the Bondi accretion model is a reasonable approximation to the accretion of a compact object provided that the bulk motion of the accreting matter (with respect to the compact object), the angular momentum and the magnetic fields can be neglected (Frank et al. 2002).

2.3 Radiatively inefficient accretion flows

Observations show that BH accretion flows can be divided into two broad classes (Yuan and Narayan 2014):

1. **Cold flows:** When the sources are very bright (with luminosities $\sim 10\% L_{\rm Edd}$), the accretion flow is an optically thick, geometrically thin accretion disk (Pringle and Rees 1972; Shakura and Sunyaev 1973), with an energy spectrum dominated by black-body radiation that peaks at soft X-rays (for some stellar mass BHs and also for NSs) or hard ultraviolet energies (for some SMBHs) (D'Angelo et al. 2015). Depending on the BH mass, the gas temperature lies in the range $10^4 - 10^7$ K, which is relatively low compared to the virial temperature.[6] Quasars observed at high redshifts are examples of sources with a cold flow (Di Matteo et al. 2012).

2. **Hot flows:** For lower gas densities the accreting gas can no longer cool efficiently. The gas temperature becomes much higher, approaching virial, and the flow becomes optically thin (Yuan and Narayan 2014). Under these conditions, there are various mechanisms (described below) which retain the accretion energy causing a lower radiative efficiency. These *radiatively inefficient accretion flows* (RIAFs) are conventionally used to model the accretion onto *low-luminosity sources* whose bolometric luminosity[7] is many orders of magnitude below the Eddington limit. Examples of these underluminous sources are the SMBHs Sgr A* and M87* (see Section 2.4).

We are going to focus in RIAFs since, as we will see later in this chapter, their lower gas densities suggest that a proper modeling of these flows requires Kinetic Theory, which is one of the main topics in this work. In the following, we are going to describe the operating physical mechanisms in the RIAFs and two well-known examples of this kind of flow.

[6] The *virial theorem* provides us with an estimation of the temperature of an astrophysical object. For an ionized hydrogen gas held together by its self-gravity within a length scale R, the *virial temperature* is given by $T_{\rm vir} \simeq \frac{GMm_{\rm p}}{6k_{\rm B}R} \sim \frac{10^{12}}{r_*}$ K, where $r_* \equiv R/r_{\rm S}$ and $r_{\rm S}$ is the Schwarzschild radius associated to a mass M (see e.g. Maoz 2016; Yuan and Narayan 2014).

[7] The bolometric luminosity is the total power output emitted by an astrophysical object across the whole electromagnetic spectrum.

2.3.1 Physics of the RIAFs

It is widely believed that a RIAF is composed by a two-temperature plasma: one temperature for the electrons and another for the ions. This property is not an assumption, but rather a generic consequence of the physics of the associated flow. To see why, we consider the following facts:

- **Radiation is produced primarily by electrons.** Larmor's formula tells us that the total power emitted by a charged particle is proportional to the square of its acceleration (Jackson 1998). Hence, the radiation emitted by the accreting flow is mainly due to the electrons because their masses m_e are much smaller (easier to accelerate) than those of the ions, m_i.

- **Ions are heated more easily than electrons.** Gravitational energy is converted into thermal energy via viscous heating and compressional heating. On one hand, by numerically modeling astrophysical scenarios of hot accretion flows, researchers have found that the fraction of the viscously dissipated energy that directly heats the electrons is around $10-50\%$, thus ions receive most of the energy coming from viscous heating. On the other hand, at regions close to the BH, the compressional heating of the electrons is less than the compressional heating of the ions because the electrons become relativistic ($k_B T_e > m_e c^2$) more easily due to their smaller mass, which causes a change in their adiabatic index. (See e.g. Yuan and Narayan (2014) for a discussion of these effects.) Thus, ions receive more heat than electrons.

- **Coulomb collisions between electrons and ions is highly inefficient.** Assuming elastic collisions and using the conservation of linear momentum, we can infer that the transfer of kinetic energy between electrons and ions takes $m_i/m_e \sim 1836$ times longer than the transfer of kinetic energy between electrons (Frank et al. 2002). Therefore, the low densities present in the RIAFs and the poor coupling between these particles via Coulomb collisions, make this process highly inefficient.

In this way, we see that: 1) electrons cool more than ions, 2) ions heat more than electrons, and 3) there is no efficient coupling mechanism between these particles. Hence, the development of a two-temperature plasma over appreciable timescales is naturally expected (Mahadevan 1999; Mahadevan and Quataert 1997).

There is no unique dynamic model of a RIAF. The difference between distinct models is basically in the origin of the low radiative efficiency. The most popular and studied class is the *advection-dominated accretion flow* (ADAF). In this model, most of the viscously generated energy stored in the ions is advected onto the central object (Abramowicz et al. 1988; Narayan

and Yi 1994; Quataert and Narayan 1999). Since only a small fraction of the ions' energy is transferred to the electrons, the total energy radiated is much less than the generated energy, causing a low radiative efficiency. The popularity of the ADAF models is due to their ability to predict accurately the observed radio-to-γ-ray spectrum from a number of accreting stellar mass and supermassive BH systems (see e.g. Narayan et al. 1998).

Other RIAF solutions propose a reduced mass accretion rate close to the accreting object. For example, the *adiabatic inflow–outflow solution* (ADIOS) assumes that most of the accretion energy is advected outwards in the form of strong matter outflows at the outer parts of the accretion flow (Blandford and Begelman 1999). Another solution is given by the *convection-dominated accretion flow* (CDAF) in which the inner particles of the flow acquire angular momentum due to convection currents. The increase in angular momentum prevents the infall of particles and, thus, a smaller net accretion rate is obtained (Quataert and Gruzinov 2000b).

In the past years, analytical and semi-analytical approaches of the RIAF solutions have successfully reproduced the main features of the EM spectra of underluminous sources (see e.g. Yuan et al. 2003). Nevertheless, the richness and complexity of the physical mechanisms present in the accretion process (see Section 2.1.2) require the implementation of magnetohydrodynamic (MHD) or general-relativistic magnetohydrodynamic (GRMHD) simulations in the regime of the RIAFs to capture all the relevant physics (see e.g. Goddi et al. 2017; Porth et al. 2017 and references therein).

2.3.2 The flows of Sgr A* and M87*

Sgr A* is the nearest SMBH at only $\sim 8.35\,\mathrm{kpc}$ from us, situated at the center of our galaxy, with a typical observed bolometric luminosity of $L_{\mathrm{observed}} \sim 10^{35}\,\mathrm{erg\,s^{-1}}$ (Falcke and Markoff 2013; Ghez et al. 2003; Gillessen et al. 2009). However, the estimated luminosity of Sgr A* is $L_{\mathrm{estimated}} = \%10\dot{M}_{\mathrm{Bondi}}\,c^2 \sim 10^{41}\,\mathrm{erg\,s^{-1}}$ (corresponding to a process with %10 of efficiency and an accretion rate of $\dot{M} = \dot{M}(r_{\mathrm{B}}) \sim 10^{-5}\,\mathrm{M_\odot\,yr^{-1}}$ at the Bondi radius $r_{\mathrm{B}} \sim 0.06\,\mathrm{pc}$; see more details on Section 2.4.1). Furthermore, the Eddington luminosity, Eq. (2.2), of Sgr A* is $L_{\mathrm{Edd}} \sim 10^{44}$ for a mass $M = 4.3 \times 10^6\,\mathrm{M_\odot}$ (Ghez et al. 2003; Gillessen et al. 2009). The six orders of difference between L_{observed} and $L_{\mathrm{estimated}}$, the eleven orders of difference between L_{observed} and L_{Edd}, as well as the low densities around Sgr A* inferred from radio (Marrone et al. 2006, 2007) and X-ray (Wang et al. 2013) observations, are clear indicators that the accreting flow of Sgr A* is radiatively inefficient (see also Event Horizon Telescope Collaboration 2022a).

M87* is another SMBH situated at the center of the galaxy Messier 87 (NGC 4486) at $\sim 16.8\,\mathrm{Mpc}$ (Event Horizon Telescope Collaboration 2019f; Gebhardt et al. 2011; Macchetto et al. 1997; Walsh et al. 2013). It is another underluminous source with a bolometric

luminosity of $L_{\text{observed}} \sim 10^{42}\,\text{erg}\,\text{s}^{-1}$ (Prieto et al. 2016) and an estimated luminosity of $L_{\text{estimated}} = \%10\dot{M}_{\text{Bondi}}\,c^2 \sim 10^{45}\,\text{erg}\,\text{s}^{-1}$ (corresponding to a process with %10 of efficiency and an accretion rate of $\dot{M} = \dot{M}(r_{\text{B}}) \sim 0.3\,\text{M}_{\odot}\,\text{yr}^{-1}$ at the Bondi radius $r_{\text{B}} \sim 0.19\,\text{kpc}$; see Section 2.4.1). The Eddington luminosity, Eq. (2.2), of M87* is $L_{\text{Edd}} \sim 10^{47}$ for $M = 6.2 \times 10^9\,\text{M}_{\odot}$ (Event Horizon Telescope Collaboration 2019e). As in the case of Sgr A*, the difference in several orders of magnitude of these luminosities, and the low densities and high temperatures of the accreting flow of M87* (Matteo et al. 2003), strongly suggest the existence of a RIAF (Kuo et al. 2014).

The proximity of Sgr A* and the large mass of M87* have made these sources the main objective of several analytical and numerical studies of accretion. Particularly, they are the principal targets of the Event Horizon Telescope (EHT) collaboration.[8] We will present a brief summary of the well-known methods used to estimate the accretion rates of these SMBHs.

2.4 The accretion rates of Sgr A* and M87*

As a first guess, the luminosity of the BH accretion flow can be used to estimate its accretion rate. However, this approximation becomes less appropriate for RIAFs due to the various physical mechanisms (advection, convection, outflows and jets) that alter the accretion flow. In particular, these mechanisms allow the possibility of having an accretion rate which depends on the distance from the BH (Yuan and Narayan 2014).

For scales of the order of the Bondi radius, the estimations of the accretion rate come from observations of the properties of the surrounding gas (see Section 2.4.1). For inner regions of the flow, the best constraints we have on the accretion rate come from radio polarization measurements (see Section 2.4.2). Nevertheless, these estimations are highly model-dependent. One of the purposes of MHD and GRMHD simulations is to obtain more general values of the accretion rate, and to test the validity of the aforementioned constraints. In the following, we will discuss the models used to constrain the accretion rates of the SMBHs Sgr A* and M87*, and their relation to current numerical simulations. It is important to mention that all of these estimations are done under the hydrodynamical approximation.

2.4.1 The Bondi estimation of the accretion rate

A crude estimation of the accretion rate onto a BH can be made with the Bondi hydrodynamical spherical accretion (see Section 2.2). Various observations indicate that Sgr A* has a mass of $\sim 4.3 \times 10^6\,\text{M}_{\odot}$ (Ghez et al. 2003; Gillessen et al. 2009). Additionally, the *Chandra X-ray*

[8] https://eventhorizontelescope.org/

Observatory discovered a flow with a temperature of $\sim 2.2 \times 10^7$ K (1.9 keV) and an electron number density of $\sim 160\,\mathrm{cm}^{-3}$ measured at ~ 0.06 pc from Sgr A* (Baganoff et al. 2003; Eatough et al. 2013). For a fully ionized hydrogen gas (in which the number densities of the electrons and protons are equal, $n_\mathrm{e} = n_\mathrm{p}$), this temperature gives a sound speed of $550\,\mathrm{km\,s}^{-1}$ (which is estimated with Eq. (2.8) using $m \approx m_\mathrm{p}$, since $m_\mathrm{e} \ll m_\mathrm{p}$), which yields a consistent value of the Bondi radius of $r_\mathrm{B} \sim 0.06\,\mathrm{pc}$, calculated with Eq. (2.7). Using these values in the Bondi accretion rate formula (2.6), we obtain

$$|\dot{M}_\mathrm{B}| \sim 10^{-5}\,\mathrm{M}_\odot\mathrm{yr}^{-1}\left(\frac{\mathrm{M}}{4.3\times10^6\mathrm{M}_\odot}\right)^2\left(\frac{n_\mathrm{e}}{160\,\mathrm{cm}^{-3}}\right)\times\left(\frac{k_\mathrm{B}T}{1.9\,\mathrm{keV}}\right)^{-\frac{3}{2}}, \tag{2.9}$$

where an adiabatic index $\gamma_\mathrm{a} = 5/3$ was assumed as in Falcke and Markoff (2013)[9]. In this case, it is implicit that one assumes the selected finite radius ~ 0.06 pc to be a good approximation for the values n_∞ and T_∞.[10] In the past years, accretion models based on numerical hydrodynamical simulations have estimated a mass accretion rate of order $\sim 10^{-6} M_\odot\,\mathrm{yr}^{-1}$ at the Bondi radius scales, calculated from the rate of gas capture from massive stellar winds in the galactic center (Cuadra and Nayakshin 2006; Cuadra et al. 2008; Cuadra et al. 2015; Quataert and Gruzinov 2000b).

The *Chandra X-ray Observatory* also measured the properties of the interstellar medium of M87* (Matteo et al. 2003; Russell et al. 2015). The surrounding flow has a temperature of $\sim 1.06 \times 10^7$ K (0.91 keV) and an electron number density of $\sim 0.31\,\mathrm{cm}^{-3}$ measured at $\sim 0.12 - 0.22$ kpc from M87*, which is consistent with a Bondi radius of $r_\mathrm{B} \sim 0.19$ kpc. Using the same assumptions as in the Bondi estimation of Sgr A* accretion rate, we obtain

$$|\dot{M}_\mathrm{B}| \sim 0.3\,\mathrm{M}_\odot\mathrm{yr}^{-1}\left(\frac{\mathrm{M}}{6.5\times10^9\mathrm{M}_\odot}\right)^2\left(\frac{n_\mathrm{e}}{0.31\,\mathrm{cm}^{-3}}\right)\times\left(\frac{k_\mathrm{B}T}{0.91\,\mathrm{keV}}\right)^{-\frac{3}{2}}, \tag{2.10}$$

where we have used the recent estimation of the mass of M87* of $\sim 6.5 \times 10^9\,\mathrm{M}_\odot$, by Event Horizon Telescope Collaboration (2019f). This estimation of the accretion rate seems to match fairly well with the overall energetic output of the relativistic jet present in M87* (Kuo et al. 2014; Matteo et al. 2003).

[9] In Falcke and Markoff (2013) it was obtained an accretion rate of $|\dot{M}_\mathrm{B}| \sim 10^{-4}$, since they did not use $\lambda_\mathrm{a} = 1/4$ in Eq. (2.6), which corresponds to $\gamma_\mathrm{a} = 5/3$ (see e.g. Frank et al. 2002).

[10] This assumption can lead to an overestimation of the actual mass accretion rate under certain conditions (Korol et al. 2016).

2.4.2 Polarization constraints to the accretion rate

The detection of linearly polarized light at ~ 230 GHz coming from Sgr A* and M87* (Aitken et al. 2000; Bower et al. 2003; Event Horizon Telescope Collaboration 2021a,b; Kuo et al. 2014) suggested another plausible way to estimate the accretion rate through the analysis of *rotation measures* (RMs) of the incoming polarized emission (Agol 2000; Quataert and Gruzinov 2000b).

It is believed that the linearly polarized light comes from the synchrotron radiation emitted by relativistic electrons at regions close to the event horizon (Bower et al. 2018, 2003). Particularly, for Sgr A* the linearly polarized light originates within distances of $\sim 10\,r_{\rm S}$ (Johnson et al. 2015), and for M87* the emission is produced within distances of $\sim 5\,r_{\rm S}$ (Event Horizon Telescope Collaboration 2019e). When the linearly polarized EM wave passes through a magnetized medium (such as those present in the accretion flows), the polarization angle ϕ changes due to a phenomenon known as *Faraday rotation*. The observed ϕ varies as a function of the wavelength λ according to (Rybicki and Lightman 1985)

$$\frac{\phi-\phi_0}{\lambda^2}=\mathscr{RM}=0.81\int_{\rm source}^{\rm observer} f_{\rm rel}(\Theta_{\rm e})\,n_{\rm e}\,B_{\parallel}\,dl \quad \mathrm{rad\,m^{-2}}, \tag{2.11}$$

where ϕ_0 is the intrinsic position angle, $\mathscr{RM}$ is the rotation measure in units of $\mathrm{rad\,m^{-2}}$, $\Theta_{\rm e}\coloneqq k_{\rm B}T_{\rm e}/m_{\rm e}c^2$ with $T_{\rm e}$ the electron temperature, $f_{\rm rel}$ is a correction term suppressing Faraday rotation at relativistic temperatures,[11] $n_{\rm e}$ is the free-electron number density in units of $\mathrm{cm^{-3}}$, $B_{\parallel}$ is the line-of-sight magnetic field in units of μG and l is the path length along the line-of-sight through the medium in units of pc. Since ϕ varies with λ for the same line-of-sight, we can estimate the value of ϕ_0 and $\mathscr{RM}$ by making measurements of ϕ at several wavelengths and using Eq. (2.11) (see e.g. Marrone et al. 2007). This procedure requires assumptions of the electron temperature, electron density and the radial magnetic field profile, and it has been applied to obtain *model-dependent constraints* on the accretion rate, as we will see below. Studies have shown that the Faraday rotation takes place mainly at the inner parts of the accretion flow at the radii $\sim (10^3-10^5)\,r_{\rm S}$[12] for Sgr A* and M87* (Bower et al. 2018; Park et al. 2019).

Using Eq. (2.11) with various RIAF accretion models in combination with certain assumptions on the magnetic field (such as equipartition between the magnetic and gravitational energy), the polarimetry observations have made possible to restrict the accretion rate of

[11] At relativistically hot temperatures ($\Theta_{\rm e}\gg 1$), we have $f_{\rm rel}(\Theta_{\rm e})\approx \log(\Theta_{\rm e})/(2\Theta_{\rm e}^2)$, whereas for subrelativistic temperatures ($\Theta_{\rm e}\ll 1$), we have $f_{\rm rel}(\Theta_{\rm e})\approx 1$ (Gardner and Whiteoak 1966; Jones and O'Dell 1977).

[12] This interval is estimated with the variability of the RMs over time. The variability can be translated into a specific radius from which the RM originates. See more details in Bower et al. (2018)

Sgr A* to the range of $(10^{-9} - 10^{-7})\,\mathrm{M}_{\odot}\mathrm{yr}^{-1}$ (or even lower depending on the assumed inner and outer radii enclosing the polarized emission; see Fig. 4 in Marrone et al. 2006) within a radius of $r \lesssim 100\,r_{\mathrm{S}}$ (Bower et al. 2003; Macquart et al. 2006; Marrone et al. 2007). For M87*, the accretion rate must be less than $9.2 \times 10^{-4}\,\mathrm{M}_{\odot}\mathrm{yr}^{-1}$ at a distance of $r \sim 21\,r_{\mathrm{S}}$ (Kuo et al. 2014). Note that the accretion rate has a smaller value at event-horizon-scales compared with the estimations at Bondi radius scales (see Section 2.4.1). This is a necessary condition because a greater accretion rate at the inner regions of the flow would depolarize the light through extreme Faraday rotation gradients (see e.g. Jiménez-Rosales and Dexter 2018; Quataert and Gruzinov 2000a).

As we emphasized before, the constraints on the accretion rate obtained with polarimetry observations are highly model-dependent. In fact, there are many important effects that are not taken into account in Eq. (2.11). For example, not all photons are Faraday rotated by the same amount of material, the polarization properties of photons can be affected by parallel transport, and neither the emission nor the Faraday rotation can be assumed to behave in a spatially uniform way due to the presence of turbulence in the accretion flow (see e.g. Ricarte et al. 2020 and references therein). Therefore, there is an intrinsic uncertainty in the obtained accretion rates which is confronted with polarized radiative transfer calculations in GRMHD simulations (see e.g. Jiménez-Rosales and Dexter 2018; Ricarte et al. 2020).

Summarizing: the accretion rates of Sgr A* and M87* are constrained in both directions (inner and outer scales) by radio polarization observations and X-ray imaging. The accretions rates have a lower value at regions close to the BH's event horizon and a greater value for larger scales. Thus, the accretion rate increases with radius. As we saw in Section 2.3, this is a behavior consistent with the possible physical mechanisms present in a RIAF. In fact, for Sgr A* the change in the accretion rate with radius is supported by measurements of the radio of H-like to He-like Fe lines (Falcke and Markoff 2013; Shcherbakov and Baganoff 2010).

2.5 The breakdown of the hydrodynamic approximation

The continuous improvement of astrophysical observations make clear that, someday, we will be able to capture certain features of the accretion process with unprecedented quality [see, for example, the reconstructed image of M87* (Event Horizon Telescope Collaboration 2019a,b,c,d,e,f, 2021a,b) and the very recent reconstructed image of Sgr A* (Event Horizon Telescope Collaboration 2022a,b,c,d,e,f)]. These observations will serve as a test-bed for our most complete models of accretion, which include realistic non-symmetrical and unsteady flows, radiative processes, magnetic fields, matter outflows, convection currents and astrophysical jets.

As we mentioned in Section 2.3.1, all of these physical phenomena present in the accretion process are currently modeled with highly-complex GRMHD simulations (see e.g. Porth et al. 2017). Nevertheless, the accreting plasma of a RIAF is effectively collisionless because is in a high-temperature and low-density regime (Baganoff et al. 2003; Event Horizon Telescope Collaboration 2019e; Harris et al. 1998; Mahadevan and Quataert 1997), so the problem of the accuracy of the hydrodynamic simulations of RIAFs must be assessed; a *kinetic approach* would seem to be the most appropriate in this kind of flows. Furthermore, the GRMHD simulations coupled to radiative transfer equations assume that the radiation is mainly emitted by electrons described with a certain *distribution function* (which is a concept from Kinetic Theory; see Chapter 3), so our physical inferences based on the GRMHD models are intimately tied to the understanding of the electron distribution function (see e.g. Event Horizon Telescope Collaboration 2019e; Ryan et al. 2018).

We expect that a fully 3D kinetic simulation of a RIAF would capture all the relevant physics. However, kinetic simulations are extremely complex due to the high computational effort of calculating the evolution of the 6D distribution functions of ions and electrons in the accreting plasma (see e.g. Kunz et al. 2016 and references therein). To overcome this difficulty, researchers have developed numerical models of collisionless (or weakly collisional) plasmas which include some kinetic effects into the equations of GRMHD flow (Chandra et al. 2015; Foucart et al. 2017; Sharma et al. 2006). However, if we want to model the kinetic accretion onto a BH, then it is natural to expect the inclusion of GR (particularly for regions close to the event horizon). This inclusion is studied in the formalism of General Relativistic Kinetic Theory, a subject which has been treated only in the analytical regime, and to which the Chapter 3 is entirely devoted. Naturally, using this theory to model the RIAFs would give us the most complete picture of the problem.

Apart from the RIAF of underluminous sources, another scenario which demands a kinetic treatment is the accretion of dark matter (DM), an exotic entity which is expected to have a collisionless nature (see e.g. Ma and Bertschinger 2004; Salucci et al. 2020). The relativistic Bondi accretion of DM onto a Schwarzschild BH has been assessed e.g. in Feng et al. (2021), however they do not work directly under the kinetic approximation. In contrast, the recent study by Mach and Odrzywołek (2021a) successfully incorporates general relativistic Kinetic Theory to the problem of accretion of DM onto a moving Schwarzschild BH and its consequences to the growth of primordial BHs in the early Universe. The kinetic modeling of the DM accretion scenario is important since there are future detection prospects which require very precise predictions (for example, it has been recognized in Coogan et al. 2022; Kavanagh et al. 2020; Li et al. 2021 that a DM distribution around a BH binary may produce a small detectable change in its gravitational wave signal). Furthermore, it has been suggested that the accretion

of DM plays a prominent role in the formation of SMBHs (Argüelles et al. 2021; Choquette et al. 2019; Read and Gilmore 2003), so a complete understanding of the origin of SMBHs may require a fully general-relativistic treatment of the subject

Overall, we can see that General Relativistic Kinetic Theory (the topic of the following chapter) is necessary to apprehend all the relevant physics when we are dealing with a collisionless flow in a strong gravitational regime, such as those present near BHs.

Chapter 3

General Relativistic Kinetic Theory

The main purpose of Kinetic Theory (KT) is to model the statistical evolution of a system with a very large number of particles and to obtain a handful of averaged properties which completely describe the system. The nature of this particles and their interactions depend on the specific system under consideration. For example, the particles could be molecules in a gas, electrons and ions in a plasma, stars, galaxies or even clusters of galaxies, and they could be affected by long- and/or short-range interactions.

To model these phenomena, the standard non-relativistic KT employs Newtonian physics and the formalism of Classical Mechanics (Lagrangian or Hamiltonian mechanics). However, we can also formulate a *relativistic KT* by incorporating the principles of Special Relativity (special relativistic KT) or the formalism of General Relativity (general relativistic KT), with the corresponding increase in complexity. These generalizations are of great relevance to Cosmology and Astrophysics since they give us an appropriate framework for modeling plasmas with relativistic velocities (such as those present at the early Universe), and for modeling the dynamics of gases in strong gravitational fields (such as those in the vicinities of black holes).

In this chapter we will introduce the basic concepts of KT, such as the phase-space and the distribution function, and we will discuss the main changes needed to formulate a KT compatible with the postulates of Special Relativity and a KT consistent with the ideas of General Relativity (Section 3.1). Then, we will focus on the basic mathematical aspects needed to formulate a general relativistic KT (Section 3.2). In particular, we are going to concentrate on a formulation on the cotangent bundle of the space-time, and we will derive the relativistic Boltzmann equation and its collisionless limit, known as the relativistic Vlasov equation (Section 3.2.1). We will also connect the mathematical definitions with their macroscopical physical counterparts (Section 3.2.2). At the end of this chapter, we will discuss the application

of general relativistic KT to the problem of astrophysical accretion with a fixed spherical symmetric space-time geometry (Section 3.2.3).

3.1 Kinetic Theory formulations

Our objective in this section is to present the core concepts that are common in all KT formulations and that will be useful for the following chapter. We refer the reader to the book of Pathria and Beale (2021) for a complete presentation of non-Relativistic KT, to the books of Cercignani and Kremer (2002); Vereshchagin and Aksenov (2017) for a discussion of the Special Relativistic KT, and to the articles of Acuña Cárdenas et al. (2022); Debbasch and van Leeuwen (2009a,b); Sarbach and Zannias (2013, 2014, 2015) for a presentation of General Relativistic KT in a modern differential geometric language, with excellent historical accounts.

Let us consider a system of $N \gg 1$ classical (non-quantum) particles.[1] If we would want to know *exactly* the dynamics of the complete system, then we would need to solve a correspondingly huge number of equations. For example, in Classical (non-relativistic) Hamiltonian Mechanics, a system of N particles in three dimensions is, in general, completely described by $6N$ coupled differential equations for the positions and momenta of particles, involving the internal and external influences acting on the system. Clearly, solving these equations is a great endeavor for large N, even numerically. For this reason, KT uses an *statistical approach* to formulate the problem.

Each possible configuration of the system, that is each particular choice of the $6N$ degrees of freedom (positions and momenta),[2] is known as a *microstate*. The set of $6N$-dimensions containing all the microstates is known as the *phase-space*. A certain *macroscopic* state of the system is realized by different possible contiguous microstates in the phase-space. In KT we do not expect to calculate the specific microstate in which the system is, but rather the *probability* that the system is in a certain volume of the phase-space which physically represents the same macroscopic state.

The probabilistic description of the complete system is given by the *distribution function* (DF) $\mathscr{F}$, which represents the probability density of the system of being in a certain microstate

[1] By incorporating the principles of Quantum Mechanics, we can obtain a formulation of a Quantum KT (see e.g. Pathria and Beale 2021). In this work, we will stick to the classical (non-quantum) formulations of KT.

[2] We are not including *internal* degrees of freedom, such as the spin of particles.

at time t. The DF is not a directly observable quantity, however, with this function we can calculate macroscopic quantities of the system through an *averaging* procedure.[3]

The DF obeys an evolution equation which represents the conservation of the probability density during the evolution of the system, or equivalently, that the flow of the microstates in the phase-space is incompressible. This equation is known as the *Liouville equation*, and in the non-relativistic formulation looks like

$$\frac{d\mathscr{F}}{dt} = 0. \tag{3.1}$$

For large N, one can formulate an equivalent description of the system in terms of the *one-particle distribution function* f. This function is defined such that the product

$$f(t,\mathbf{x},\mathbf{p})\, d^3x d^3p, \tag{3.2}$$

represents the average number of particles in the volume element d^3x about $\mathbf{x}$, with momenta in a range d^3p about $\mathbf{p}$, at time t. The evolution equation for this function is known as the *Boltzmann equation*,

$$\frac{df}{dt} = C[f], \tag{3.3}$$

where $C[f]$ is the *collision operator* or *collision term* containing the information of the interactions between particles. When the probability of finding a particle near any phase-space point is unaffected by the other particles we have $C[f] \equiv 0$, and we obtain the *collisionless Boltzmann equation* or *Vlasov equation*.

The previous ideas constitute the basic concepts appearing in KT. However, to model kinetic flows in non-Newtonian scenarios (such as plasmas moving at relativistic velocities or gases in strong gravitational fields), we need to formulate a description consistent with the relativistic framework. This will be our task in the following sections.

3.1.1 Special Relativistic Kinetic Theory

The first extension of KT was made by Jüttner (1911a,b) who generalized the Maxwell-Boltzmann DF in a form consistent with the existence of the limiting speed c imposed by Special Relativity (SR). In the next years, the theory was further developed to include consistently all the principles of SR (see e.g. De Groot et al. 1980; Debbasch et al. 2001; Vereshchagin and Aksenov 2017 and references therein). In this way, the resultant framework

[3] Experiments and observations deal with space- and time-averaged quantities. Nevertheless, statistical theory usually works with *ensemble-averages* calculated with the DF. (An *ensemble* is a large set of macroscopically equal systems (but with possibly different microstates), and an *ensemble average* is an average over this set.)

maintains the same ideas and concepts of the non-relativistic formulation, but introduces three necessary conditions: 1) the momentum of the particles must satisfy the *on-shell restriction* (1.6) in Minkowski space-time, 2) the DF must be a Lorentz scalar (an invariant under Lorentz transformations), and 3) the equations must appear in a covariant way to manifest the equal treatment of space and time, and the equivalence between different inertial systems. Also, the meaning of initial data has to be reconsidered due to the reformulation of the concepts of space and time in SR.

A priori, the special relativistic one-particle DF depends on the points (x^μ, p^μ) of the phase-space. Nevertheless, the requirement that physical particles should obey the on-shell condition restricts the DF to the points (x^μ, p^i) since, conventionally, we can obtain the time component of the momentum from its spatial components using Eq. (1.6) with the Minkowski metric, thus obtaining $p^t = \sqrt{\mathbf{p} + m^2c^2}$. The points in phase-space which satisfy the on-shell restriction form a set known as the *mass shell*.

The special relativistic one-particle DF is defined in an analogous way as in Eq. (3.2). It follows from the transformation properties of vectors under Lorentz transformations and the on-shell condition, that the volume element $d^3x\,d^3p$ is a Lorentz scalar. Moreover, since the number of particles in the volume element $d^3x\,d^3p$ is also a Lorentz scalar (all observers will count the same particles), we conclude from the special relativistic version of Eq. (3.2) that the DF is a Lorentz scalar (Cercignani and Kremer 2002; Vereshchagin and Aksenov 2017).

The evolution equation for the one-particle DF has the same structure as Eq. (3.3). The left-hand side is substituted by an operator acting on f, called the *Liouville operator*, which contains information about the dynamics of the DF and the external forces acting on the system. Analogously, the right-hand side is associated to the interactions between particles, but considering the universal limit in the propagation of interactions imposed by the speed c.

3.1.2 General Relativistic Kinetic Theory

In the previous KT formulations, the dynamical physical entities are the particles and the internal or external fields acting on them. In the special relativistic formulation we had to incorporate the principles and ideas of SR. However, in a general relativistic KT (GRKT) the space-time itself is a dynamical entity which is influenced by the presence of particles and fields through the Einstein's field equations, so we need to take into account self-consistently the back reaction of particle kinetics on the background metric. Besides the difficulty of having an extra dynamical object, the problem *per se* is mathematically more challenging due to the complexity of differential geometry and the non-trivial nature of Einstein's field equations. So, how can we formulate a GRKT?

A crude procedure to obtain a fully GRKT is 1) write the KT definitions and equations in a way consistent with the framework of GR, and 2) couple the KT equations to the Einstein's field equations. The first step can be done within the formalism of differential geometry (see e.g. Acuña Cárdenas et al. 2022; Andreasson 2011; Debbasch and van Leeuwen 2009a,b; Sarbach and Zannias 2013, 2014, 2015). In Section 3.2 we outline a procedure to obtain a generalization of KT with a *cotangent bundle* formulation; in particular, we obtain the relativistic Boltzmann equation in this formalism. The second step requires the construction of an energy-momentum tensor from the DF (see Section 3.2.2), and the insertion of this tensor into the Einstein's field equations (1.1). The resulting system of equations (the relativistic Boltzmann equation for the DF + the Einstein's field equations for the space-time metric) is known as the *Einstein-Boltzmann* system.

Due to the complexity of the Einstein-Boltzmann system, it has been studied scarcely in the literature. To solve this complicated system one has to rely on different approximations, for example, assuming a background metric. Particularly, the Einstein-Boltzmann system has been studied in the context of Cosmology (see e.g. Lee 2013; Lee and Nungesser 2017, 2018; Lee et al. 2020), with the greatest application being to the early Universe: the inhomogeneities present at the early Universe can be analyzed by solving the Einstein-Boltzmann equations for different particle species in a perturbed Friedmann-Lemaître-Robertson-Walker space-time (see e.g. Dodelson and Schmidt 2020). On the mathematical side, Bancel and Choquet-Bruhat (1973) proved the (local in time) well-posedness for the Cauchy problem of the Einstein-Maxwell-Boltzmann system, which is an extension of the Einstein-Boltzmann system that includes the Maxwell equations. Following the latter work, Mucha (1998) studied the Cauchy problem for the Einstein-Boltzmann system with improved regularity assumptions on the initial data. We refer the reader to the references in Andreasson (2011) and Lee and Rendall (2013) for other mathematical works on the Einstein-Boltzmann system.

The simpler system composed by the collisionless Boltzmann equation coupled to the Einstein's field equation (called the *Einstein-Vlasov* system) has received more attention (see e.g. the review by Andreasson 2011). This system has been studied mathematically (see, for example, the proof of local existence of solutions to the Einstein-Vlasov system given smooth initial data by Choquet-Bruhat 1971, or Rein and Rendall 1992 for the existence of global asymptotically flat singularity-free solutions of the spherically symmetric Einstein-Vlasov system), and it has been used to analyze several problems related to Cosmology (such as the global existence of solutions for the future stability of the Universe, see e.g. Andersson and Fajman 2020; Andréasson and Ringström 2013; Barzegar and Fajman 2020; Fajman 2016; Joudioux et al. 2021; Ringström 2013) and Gravitation [such as gravitational collapse (Andreasson 2012; Andréasson 2014; Rendall and Velazquez 2011), the presence of singularities

in the space-time (Rendall and Velázquez 2017), the existence of solutions with spherical (Andréasson et al. 2014; Andreasson and Rein 2007; Rein 1994) and axisymmetrical symmetries (Andreasson et al. 2011, 2014), and the non-linear stability of Minkowski space-time (Bigorgne et al. 2021; Lindblad and Taylor 2020; Taylor 2016)].

Another simplification that can be made for the study of a GRKT is that, when the densities and energies of the particles are relatively low, we can ignore the self-gravity of the collection of particles. In this way, one selects a fixed background geometry (for example, a Schwarzschild or a Kerr space-time) and solve the Boltzmann or Vlasov equation for the DF. In this way, we obtain a *GRKT in a fixed curved space-time geometry*. Within this framework, people have studied, for example, the *mixing* of a gas of massive particles (Rioseco and Sarbach 2018, 2020),[4] the decay of massless particles (Andersson et al. 2018; Bigorgne 2020), and the astrophysical accretion onto a BH (Cieślik and Mach 2020; Gamboa et al. 2021; Mach and Odrzywołek 2021a,b, 2022; Rioseco and Sarbach 2017a,b), which is the main topic of this work. In Section 3.2.3 and Chapter 4, we are going to restrict to the fixed-background approach.

3.2 Kinetic Theory in curved space-times

Our first task is to introduce a covariant generalization of KT. In order to do this, we will work with a space-time (M,g), where M is a differentiable manifold and g is a pseudo-Riemannian metric (see Section 1.1 for a very brief introduction of these and subsequent mathematical objects; also see e.g. Nakahara 2003; Renteln 2014 for the complete definitions and physical interpretations of these entities). Physically, we associate *positions* of particles to the space-time points $x \in M$, and the *velocities* (or *momenta*) of particles at x to elements in T_xM. Since there exists an isomorphism between T_xM and T_x^*M (given by the metric g), is equally valid to associate the velocities (or momenta) of particles to T_x^*M. The main difference between these two points of view is the type of tensor we are dealing with; namely, the elements in T_xM are tensors of type $(1,0)$ (one upper index) called *vectors* and those of T_x^*M are of type $(0,1)$ (one lower index) called *covectors*.

We consider a gas of identical particles with mass m,[5] such that the one-particle DF f can be restricted on the *future mass shell* Γ_m^+ ($f \in \mathscr{F}(\Gamma_m^+)$ in the notation of differential

[4] A collisionless, relativistic kinetic gas propagating in the equatorial plane of a Kerr BH undergoes a relaxation process due to *phase-space mixing*, in which the kinetic gas eventually settles down to a stationary, axisymmetric configuration surrounding the BH. In this way, the final state of the gas is described by an effective DF depending only on the system's integrals of motion. See more details in Rioseco and Sarbach (2018, 2020).

[5] A gas composed by different species of particles would need a different DF for each species, besides a distinct evolution equation (a relativistic Boltzmann equation) for each DF.

geometry[6]), which is a seven-dimensional submanifold of T^*M consisting of those points (x^μ, p_μ) for which the on-shell restriction (1.6) is satisfied, and we require $p^\mu = g^{\mu\nu}p_\nu$ to be future-directed.[7] Therefore,

$$\Gamma_m^+ \coloneqq \{(x,p) \in T^*M : g_x^{-1}(p,p) = -m^2, \;\; p \text{ is future-directed}\}, \tag{3.4}$$

where we have used the inverse metric g^{-1} at x, since $p \in T_x^*M$. Notice that we can parametrize the future mass shell with the coordinates (x^μ, p_i), $i = 1,2,3$, since we can get the time component of the momentum from the mass-shell constraint (1.6). The future mass shell Γ_m^+ represents the *relativistic phase-space* for a simple kinetic gas. It is important to mention that the relativistic phase-space can also be associated to definitions on the tangent bundle TM. However, we are going to focus on the cotangent bundle formulation because it is more naturally adapted to the Hamiltonian formalism used in this work. Of course, both formulations are equivalent since TM and T^*M are isomorphic to each other through the metric g.

Finally, we can define the *future mass hyperboloid* as the set of covectors that satisfy the on-shell restriction and are future-directed,

$$P_x^+(m) \coloneqq \{p \in T_x^*M : g_x^{-1}(p,p) = -m^2, \;\; p \text{ is future-directed}\}. \tag{3.5}$$

Note that in the first definition we are dealing with points (x,p) and in the second definition we are dealing just with the covectors p. We will employ the definition (3.5) to specify the domain of integration of quantities that appear in the macroscopic description of the kinetic gas (see Section 3.2.2).

We refer the reader to the references Acuña Cárdenas et al. (2022); Andreasson (2011); Debbasch and van Leeuwen (2009a,b); Sarbach and Zannias (2013, 2014, 2015) for a comprehensive introduction to the geometry of the relativistic phase-space.

3.2.1 The relativistic Boltzmann equation

In the cotangent bundle formulation we can use a *symplectic form* and the Hamiltonian formalism to arrive at the relativistic Boltzmann equation, which is the evolution equation for the DF. For the sake of completeness, we will present very basic concepts required to

[6] We will use modern differential geometry notation, so that $\mathscr{F}(N)$ and $\mathscr{X}(N)$ refer to the class of C^∞-differentiable real scalar functions and vector fields, respectively, on a C^∞-differentiable manifold N.

[7] We assume that M is *time orientable*, so that we can make a continuous designation of "past" and "future" as we move on M (Wald 1984).

understand the derivation of the relativistic Boltzmann equation in curved space-times. A more detailed and pedagogical presentation can be found e.g. in Acuña Cárdenas et al. (2022).

Given a smooth function $\mathscr{H} \in \mathscr{F}(T^*M)$ on the cotangent bundle ($\mathscr{H}$ will be the *Hamiltonian function*) and the symplectic form $\Omega_s := d\Theta = dp_\mu \wedge dx^\mu$ (which is the differential of the Poincaré one-form $\Theta = p_\mu dx^\mu$), we can construct the associated Hamiltonian vector field $X_\mathscr{H} \in \mathscr{X}(T^*M)$ as

$$X_\mathscr{H} = \frac{\partial \mathscr{H}}{\partial p_\mu}\frac{\partial}{\partial x^\mu} - \frac{\partial \mathscr{H}}{\partial x^\mu}\frac{\partial}{\partial p_\mu}, \tag{3.6}$$

whose integral curves are determined by Hamilton's equation of motion.

In the Hamiltonian formulation we can compute the change of a function $\mathscr{G} \in \mathscr{F}(T^*M)$ along the Hamiltonian flow generated by $X_\mathscr{H}$, through the *Poisson brackets*. These brackets are defined using the symplectic form Ω_s, so that for two smooth functions $\mathscr{H}, \mathscr{G} \in \mathscr{F}(T^*M)$ with associated vector fields $X_\mathscr{H}, X_\mathscr{G} \in \mathscr{X}(T^*M)$, their Poisson bracket is given by

$$\{\mathscr{H}, \mathscr{G}\} := \Omega_s(X_\mathscr{H}, X_\mathscr{G}) = \frac{\partial \mathscr{H}}{\partial p_\mu}\frac{\partial \mathscr{G}}{\partial x^\mu} - \frac{\partial \mathscr{H}}{\partial x^\mu}\frac{\partial \mathscr{G}}{\partial p_\mu}, \tag{3.7}$$

where, in the last equality, we have written the expression of the Poisson brackets in local adapted coordinates. The importance of these concepts is that the *integrals of motion* (those quantities which are invariant under the Hamiltonian flow) of the system have a well defined property with respect to the Poisson brackets, namely,

$$\mathscr{G} \text{ is an integral of motion if and only if } \{\mathscr{H}, \mathscr{G}\} = 0.$$

Furthermore, with the chain rule, it can be proven that any function g of the integrals of motion, is also an integral of motion, i.e. $\{\mathscr{H}, g(\mathscr{G})\} = 0$. This property will be particularly important when we discuss the Vlasov equation.

The associated vector field of the free one-particle Hamiltonian $\mathscr{H}_{1\mathrm{p}}$,

$$\mathscr{H}_{1\mathrm{p}}(x,p) = \frac{1}{2} g^{\mu\nu}(x) p_\mu p_\nu, \tag{3.8}$$

is known as the *Liouville vector field* $\mathscr{L}$, and it is explicitly given by

$$\mathscr{L} := X_{\mathscr{H}_{1\mathrm{p}}} = g^{\mu\nu} p_\nu \frac{\partial}{\partial x^\mu} - \frac{1}{2}\frac{\partial g^{\alpha\beta}}{\partial x^\mu} p_\alpha p_\beta \frac{\partial}{\partial p_\mu}, \tag{3.9}$$

which can be calculated inserting Eq. (3.8) in (3.6). It can be shown that $\mathscr{L}$ is also a vector field on the future mass shell Γ_m^+, i.e. $\mathscr{L} \in \mathscr{X}(\Gamma_m^+)$ (Acuña Cárdenas et al. 2022). Therefore, when the integral curves of $\mathscr{L}$ are projected onto the space-time manifold, we obtain the

affinely parametrized geodesics of test particles with mass m. In other words, the world lines of the gas particles are described by the integral curves of the Liouville vector field $\mathscr{L}$.

In order to give a physical interpretation of the mathematical machinery presented so far, we consider a 3-dimensional hypersurface S in (M,g) representing a certain volume at a given time. We define the set

$$\Sigma := \{(x,p) : x \in S \text{ and } p \in P_x^+(m)\}, \tag{3.10}$$

and we define $\mathscr{N}(\Sigma)$ as the averaged number of occupied trajectories in Γ_m^+ crossing Σ. If the hypersurface Σ evolves into a new hypersurface Σ', then one can show that the net change in the averaged number of occupied trajectories, $\mathscr{N}(\Sigma') - \mathscr{N}(\Sigma)$, is directly related to the application of the Liouville operator onto the one-particle DF, $\mathscr{L}[f]$.

In particular, for a gas of *collisionless particles* we have $\mathscr{N}(\Sigma') = \mathscr{N}(\Sigma)$, which implies the *Liouville equation* (also known as *Vlasov* or *collisionless Boltzmann equation*)

$$\mathscr{L}[f] = g^{\mu\nu} p_\mu \frac{\partial f}{\partial x^\nu} - \frac{1}{2} \frac{\partial g^{\alpha\beta}}{\partial x^\mu} p_\alpha p_\beta \frac{\partial f}{\partial p_\mu} = 0. \tag{3.11}$$

Note that, from Eqs. (3.7), (3.8) and (3.11), the Vlasov equation can be written as

$$\mathscr{L}[f] = \{\mathscr{H}_{\rm lp}, f\} = 0. \tag{3.12}$$

On the other hand, if there are collisions between particles (with these interactions being of a binary, elastic and point-like nature), and the *molecular chaos hypothesis* (which asserts that just before collisions, the particles are uncorrelated) is satisfied, then we can obtain the *relativistic Boltzmann equation*,

$$\mathscr{L}[f] = C_W[f,f], \tag{3.13}$$

where W is the *transition probability density* for the binary collisions, and $C_W[f,f]$ is the associated *collision term* which depends quadratically on f. The details of this derivation can be found e.g. in Acuña Cárdenas et al. (2022).

A final point regarding the integrals of motion can be made here. Following the discussion after Eq. (3.7), we can see that if there are n conserved quantities $\mathscr{G}_i$ ($i = 1,2,...,n$) in the system (such that $\{\mathscr{H}_{\rm lp}, \mathscr{G}_i\} = 0$), and if f is a function only of these conserved quantities, $f = f(\mathscr{G}_i)$, then this DF must be a solution of the Vlasov equation (3.12). This remark will be extremely important in this work, since we are going to consider DFs which only depend on the energy and angular momentum, due to the symmetries of the studied systems.

3.2.2 Macroscopic description

The macroscopic description of the gas is based on the *moments* of the one-particle DF. The first moment is known as the *particle four-flow* or *particle current density*, and is defined as a vector field over T_xM. In an adapted local coordinate system, its components are given by

$$J^\mu(x) := c\int_{P_x^+(m)} p^\mu f(x,p)\,\mathrm{dvol}_x(p), \tag{3.14}$$

where $\mathrm{dvol}_x(p)$ is the Lorentz-invariant volume element on the future mass hyperboloid $P_x^+(m)$, defined as

$$\mathrm{dvol}_x(p) := \frac{1}{\sqrt{-g}}\frac{d^3p_*}{p^t}, \tag{3.15}$$

with $\sqrt{-g}$ the square root of the metric's determinant and where $p_* = (p_i)$ refer to the spatial components of the covariant linear momentum (Debbasch and van Leeuwen 2009a).

The second moment of the DF is also of particular relevance because it represents the energy-momentum tensor of the gas. Its components are given by

$$T^{\mu\nu}(x) := c\int_{P_x^+(m)} p^\mu p^\nu f(x,p)\,\mathrm{dvol}_x(p). \tag{3.16}$$

(Note that, if we were to consider the complete Einstein-Boltzmann or Einstein-Vlasov system, then we would need to insert the energy-momentum tensor (3.16) in the Einstein's field equations (1.1) to obtain the evolution equation for the space-time metric.) For the following, we will omit the notation referring to $P_x^+(m)$ in the integrals for briefness.

In the accretion process we are mainly interested in the first moment of f because it is physically associated with the flow of particles. In particular, an expression for an invariant particle number density n (independent of coordinates) shall be useful to quantify the accretion rate. To find such expression, we choose coordinates comoving with the flow of particles, such that *locally* the time component of Eq. (3.14) is

$$J^t(x) = c\int p^t f(x,p)\,\mathrm{dvol}_x(p) = c\int f(x,p)\,d^3p_*. \tag{3.17}$$

Identifying $\int f(x,p)\,d^3p_*$ as the particle number density in the comoving frame, we see that $J^t(x) = cn(x)$, for these coordinates. In this way, $n(x) = \frac{1}{c}\sqrt{(J^t(x))^2}$. Since in the comoving frame there is no net flow of particles in the spatial directions ($J^i = 0$), then we can propose the following generalized equation for the scalar particle number density,

$$n(x) := \frac{1}{c}\sqrt{-J^\mu(x)J_\mu(x)}. \tag{3.18}$$

Following these ideas, we define the mean four-velocity of the particles as (Eckart 1940)

$$u^{\mu}(x) := \frac{J^{\mu}(x)}{n(x)}. \tag{3.19}$$

Note that the units of the particle current density J^{μ} are $1/(\text{length}^2 \times \text{time})$.

An important property of the particle current density is that it has zero divergence, provided that the relativistic Vlasov equation (3.12) is satisfied. This property is known as the *continuity equation* and it expresses the conservation of the number of particles. The short proof relies on choosing a Gaussian coordinate system, so that $g_{\mu\nu}(x) = \eta_{\mu\nu}(x)$ and $\partial_{\sigma} g_{\mu\nu}(x) = 0$ at a certain point $x \in M$. In this way,

$$\begin{aligned}
\nabla^{\mu} J_{\mu}\big|_x &= \eta^{\mu\nu}\partial_{\nu} J_{\mu}\big|_x = \eta^{\mu\nu}\partial_{\nu}\int p_{\mu} f(x,p)\,\mathrm{dvol}_x(p) = \eta^{\mu\nu}\int p_{\mu}\partial_{\nu}\left[f(x,p)\,\frac{1}{\sqrt{-g}}\frac{d^3p_*}{p^t}\right] \\
&= \int \eta^{\mu\nu} p_{\mu}\partial_{\nu} f\,\mathrm{dvol}_x(p) = \int g^{\mu\nu} p_{\mu}\partial_{\nu} f\,\mathrm{dvol}_x(p) \\
&= \int L[f]\,\mathrm{dvol}_x(p),
\end{aligned} \tag{3.20}$$

where, in the first line, we have calculated the four-divergence in Gaussian coordinates, we have used the definition of the particle current density (3.14) and the expression of the volume element (3.15); from the first to the second line we have used that $\partial_{\nu} g_{\mu\sigma}(x) = 0$, and then we have used that $g_{\mu\nu}(x) = \eta_{\mu\nu}(x)$; and from the second to the third line we have employed Eq. (3.9), so that

$$\mathscr{L}[f] = g^{\mu\nu} p_{\mu}\partial_{\nu} f - \frac{1}{2}\partial_{\mu} g^{\alpha\beta} p_{\alpha} p_{\beta}\frac{\partial f}{\partial p_{\mu}} = g^{\mu\nu} p_{\mu}\partial_{\nu} f, \tag{3.21}$$

since $\partial_{\mu} g^{\alpha\beta} = 0$. Therefore, if $\mathscr{L}[f] = 0$, then

$$\nabla^{\mu} J_{\mu} = 0. \tag{3.22}$$

The energy-momentum tensor (3.16) also satisfies the conservation equation $\nabla^{\mu} T_{\mu\nu} = 0$ for a Vlasov gas. However, in this work, we will just need Eq. (3.22).

3.2.3 Spherically symmetric accretion

A very interesting application of the GRKT is the relativistic kinetic accretion onto a BH, which is a natural scenario with a highly astrophysical relevance. For the following, we assume that the self-gravity of the kinetic gas can be neglected, and that the gravitational background

is given by the stationary, spherically symmetric space-time metric (1.3). Furthermore, we will assume that the gas has acquired a configuration with the same symmetries of the metric (1.3). Thus, the one-particle DF f will be spherically symmetric and time independent.

As we saw in Sections 1.1 and 1.3, the symmetries of the metric (1.3) are related to the existence of four Killing vectors: one associated with the invariance under time translations and three with the invariance under spatial rotations. Therefore, the integrals of motion in this case consist of the energy E and the angular momentum vector $\mathbf{L}$ associated with the spherical symmetry.

Now, we will show that the continuity equation (3.22) applied to the spherically symmetric space-time metric (1.3), conduces to a mass accretion rate $\dot{M}$ independent of time and radius. We begin with the well-known coordinate expression for the divergence of a vector field (see e.g. Hartle 2003),

$$\nabla_\mu J^\mu = \frac{1}{\sqrt{-g}}\partial_\mu\left(\sqrt{-g}J^\mu\right). \tag{3.23}$$

Using the continuity equation (3.22) and the time-independence of the components of the metric and of the DF, we get

$$\partial_i\left(\sqrt{-g}J^i\right) = 0. \tag{3.24}$$

Next, we note from Eqs. (3.14) and (3.15) that

$$\sqrt{-g}J^i = c\int p^i f(x,p)\frac{d^3p_*}{p^t}. \tag{3.25}$$

Since f does not depend on the angular variables (it is spherically symmetric), then Eqs. (3.24) and (3.25) imply

$$\partial_r\left(\sqrt{-g}J^r\right) = 0 \qquad \rightarrow \qquad \sqrt{-g}J^r \equiv h(\theta,\phi), \tag{3.26}$$

where $h(\theta,\phi)$ is a function that appears after integration. To determine this unknown function, we compute the determinant of the metric (1.3), obtaining

$$\sqrt{-g} = r^2\sin\theta\sqrt{[g_{tr}(r)]^2 - g_{tt}(r)g_{rr}(r)}. \tag{3.27}$$

Therefore, Eqs. (3.26) and (3.27) give us

$$r^2J^r\sqrt{[g_{tr}(r)]^2 - g_{tt}(r)g_{rr}(r)} = \frac{h(\theta,\phi)}{\sin\theta}. \tag{3.28}$$

Eq. (3.28) is an equality between expressions that depend on different independent coordinates, hence it must be equal to a constant,

$$r^2 J^r \sqrt{[g_{tr}(r)]^2 - g_{tt}(r) g_{rr}(r)} = \text{const.} \tag{3.29}$$

For the Schwarzschild metric (1.13) which has $g_{tr}(r) = 0$ and $g_{tt}(r) = -1/g_{rr}(r)$, we obtain

$$r^2 J^r = \text{const.} \tag{3.30}$$

Since J^r is the particle current density (with dimensions of length^{-2} $\times$ time^{-1}) in the radial direction, then the flux of particles with mass m through a sphere of constant areal radius will be $4\pi r^2 m J^r$. Thus, we conclude that the accretion rate for the Schwarzschild metric is

$$\dot{M} = 4\pi r^2 m J^r = \text{const.} \tag{3.31}$$

This definition is coordinate-independent since it is defined in terms of the areal radius r and the contravariant r-component of the current density vector field, $J^r = dr(J)$. Also note that Eq. (3.31) can be evaluated at different radii, however, the combination $r^2 J^r$ is independent of this choice. Thus, the expression in (3.31) does not depend on radius nor in time.

3.2.4 Newtonian limit

In the Newtonian approximation (non-relativistic limit) the speed of the particles is much smaller than the speed of light, $|u^i| \ll c$, and the time component of the four-momentum satisfies $p^0 = mc\,dt/d\tau \approx mc$. Furthermore, the space-time is not curved, so that $g_{\mu\nu} = \eta_{\mu\nu}$, and thus $\sqrt{-g} = 1$. With these approximations, we will recover standard formulae for the particle number density, the average velocity and the mass accretion rate, that can be verified, for example, with Shapiro and Teukolsky (1983).

We begin using the previous approximations with Eqs. (3.14) and (3.15). We get

$$J^t(x) = c \int mc\, f(x,p) \frac{d^3 p_*}{mc} = c \int f(x,p)\, d^3 p_*, \tag{3.32}$$

$$J^i(x) = c \int p^i f(x,p) \frac{d^3 p_*}{mc} = \int \frac{p^i}{m} f(x,p)\, d^3 p_*. \tag{3.33}$$

Next, from Eq. (3.18) we get

$$n(x) = \frac{1}{c} \sqrt{[J^t(x)]^2 - J_i(x) J^i(x)} \approx \int f(x,p)\, d^3 p_*, \tag{3.34}$$

which is the classical equation for the particle number density and where we have used that $J^t \sim \mathscr{O}(c)$ and $J^i \sim \mathscr{O}(1)$. Then, employing Eq. (3.19) and (3.33), we obtain

$$u^i(x) = \frac{1}{n(x)} \int \frac{p^i}{m} f(x,p)\, d^3 p_*, \tag{3.35}$$

which is the non-relativistic average velocity in the i-direction. Finally, using Eqs. (3.19), (3.31) and (3.33), we arrive at

$$\dot{M} = 4\pi r^2 m n(x) u^r(x) = 4\pi r^2 \int p^r f(x,p)\, d^3 p_*, \tag{3.36}$$

which is also the expected result for the Newtonian spherically symmetric accretion.

Chapter 4

Relativistic kinetic accretion from finite radius

A very important application of Kinetic Theory is to the problem of astrophysical accretion. Depending on the collisional nature of the kinetic gas and on the gravitational regime, we may describe the accretion scenario with the Boltzmann or Vlasov equation coupled to the Poisson or Einstein equations. However, as we saw in the past chapter, the formulation of Kinetic Theory *per se* changes depending on the physical conditions of the system. In this way, the more general formalism to study the accretion of kinetic gases would be one described by the general relativistic Boltzmann equation coupled to the Einstein's field equations. Nevertheless, this system of equations is highly complex, so one has to rely on different assumptions to obtain analytical or numerical solutions.

In the context of accretion onto BHs, a particularly useful simplification is to assume that the space-time background is fixed and that the gas is collisionless. Under this assumption, Rioseco and Sarbach (2017a,b) developed a systematic study for the kinetic accretion of a collisionless gas onto a Schwarzschild BH. This systematic framework has been generalized in order to describe the kinetic accretion of a collisionless gas onto a *moving* Schwarzschild BH (Mach and Odrzywołek 2021a,b, 2022) and onto a Reissner-Nordström BH (Cieślik and Mach 2020). Very recently, this framework has also been used to study stationary and axisymmetric gas configurations surrounding a Schwarzschild BH (Gabarrete and Sarbach 2022). However, a common assumption of these kinetic models is that the gas is distributed in an *infinite* cloud, so that the external boundary conditions are given at infinity. At first glance, this is an incorrect supposition since we expect that all astrophysical systems have a finite extension.

To investigate the consequences of this latter assumption, in this chapter we will apply general relativistic Kinetic Theory to study the accretion of a collisionless kinetic gas from *finite* radius onto a Schwarzschild BH, a scenario which is more physically realistic than the

infinite distribution. We will analyze both the non-relativistic and relativistic limits, and we will specialize our results to a mono-energetic and Maxwell-Jüttner distribution functions, for a purely radial accretion (Section 4.1) and an accretion with angular momentum (Section 4.2). We will provide expressions for the accretion rate which generalize previous known solutions. At the end, we will present a summary of our relativistic analytic models (Section 4.3), and we will use them to analyze the accretion rates of Sgr A* and M87* at Bondi radius and event horizon scales (Section 4.4).

In the computations presented in this chapter, we assume that particles of mass m are being accreted from an *injection sphere* fixed at a finite areal radius R, where they have a specific numerical density and an energy or temperature which provide the external boundary conditions for the problem. Moreover, the one-particle DF is assumed to depend on (x,p) only through the integrals of motion of each particle, E (the energy) and L (the magnitude of the angular momentum), which arise from the static, spherical symmetry. Due to dispersion and mixing, it is in fact expected that any gas configuration relaxes in time to one described by such a DF, provided the boundary conditions specified at the injection sphere are compatible with it (see footnote 4 in Chapter 3). We shall use the capital letter F to denote the DF expressed in terms of E and L.

4.1 Purely radial accretion

In this section we treat both the non-relativistic and relativistic limits of the steady, spherically symmetric radial infall of a Vlasov gas onto a central object from finite radius, assuming that each individual particle has zero angular momentum. The distribution function describing this scenario depends only on the radial coordinate r and its momentum p_r, and the corresponding observables only on r. The definitions given in Section 3.2.2 are specialized in order to describe adequately the radial accretion process.

4.1.1 Non-relativistic limit

In this limit the particles are under the effect of a Newtonian gravitational central potential $\Phi(r)$ generated by a mass M (in the case of a point mass we have $\Phi(r) = -GMm/r$), and the injection sphere of the particles is at radius R, where we specify the particle number density n_R. We ignore interactions with the surface of the central object since we are interested in a scenario analogous to a Schwarzschild BH, where there is no physical surface. To obtain the scalar number density, the average radial velocity and the accretion rate we will use Eqs. (3.34-3.36).

We start by writing the momentum volume element (3.15) in flat space described by spherical coordinates (r,θ,ϕ),

$$\mathrm{dvol}_x(p) = \frac{1}{\sqrt{-g}}\frac{d^3p_*}{p^t} = \frac{1}{r^2\sin\theta}\frac{dp_r\,dp_\theta\,dp_\phi}{p^t}. \tag{4.1}$$

Under spherical symmetry, the observables of the system [e.g. the scalar particle density (3.18)] do not have any dependence on the angular variables $(\theta,\,\phi)$. Since the observables are constructed by taking moments of the distribution function [see e.g. (3.14)], the integrand $f(x,p)\,\mathrm{dvol}_x(p)$ must be independent of the angular variables. Therefore, if there is spherical symmetry and the particles have zero angular momentum ($p_\theta = 0$, $p_\phi = 0$), Eq. (4.1) suggest us that the complete distribution function $f^* = f^*(t,r,\theta,\phi,p_r,p_\theta,p_\phi)$ must satisfy

$$f^*(t,r,\theta,\phi,p_r,p_\theta,p_\phi) = f(t,r,p_r)\delta(p_\theta)\delta(p_\phi)\sin\theta, \tag{4.2}$$

where $f = f(t,r,p_r)$ is the radial one-particle distribution function. In this way, there will be no angular dependence in the observables.

To obtain the integration limits in Eqs. (3.34-3.36), we need to obtain the minimum value for $|p_r|$ (the maximum value of $|p_r|$ is not bounded). In order to do this, we see that at the injection radius $r = R$, the minimum possible energy of a particle is $E_{\min} = \Phi(R)$, corresponding to a particle falling radially from rest, since its total mechanical energy is

$$E = \frac{p_r^2}{2m} + \Phi(r), \tag{4.3}$$

and an energy satisfying $E < \Phi(R)$ would require an imaginary momentum. The conservation of energy, $E = E_{\min}$, give us the radial momentum with the minimum possible magnitude

$$p_{\mathrm{m}}(r,R) \coloneqq -\sqrt{2m[\Phi(R) - \Phi(r)]}, \tag{4.4}$$

where we have used the negative root since the particles are infalling.

Consequently, from Eqs. (3.34-3.36) and Eqs. (4.2- 4.4), we find that

$$n(r) = \frac{1}{r^2}\int_{-\infty}^{p_{\mathrm{m}}(r,R)} f(r,p_r)\,dp_r, \tag{4.5}$$

$$u^r(r) = \frac{1}{r^2\,m\,n(r)}\int_{-\infty}^{p_{\mathrm{m}}(r,R)} p_r\,f(r,p_r)\,dp_r, \tag{4.6}$$

$$\dot{M} = 4\pi r^2\,m\,n(r)\,u^r(r) = 4\pi\int_{-\infty}^{p_{\mathrm{m}}(r,R)} p_r\,f(r,p_r)\,dp_r. \tag{4.7}$$

where $p^r = p_r$, since we are in flat space. Note that if $R \to \infty$, then $n(r \to \infty) = 0$ (which is consistent with the fact that the distribution function vanishes at infinite radius), and thus we cannot apply the boundary condition $n(R) = n_R$.

This set of equations can be applied to any steady, spherically symmetric distribution function describing a radial infall of particles from finite radius onto a central object with no surface, described by a Newtonian potential $\Phi(r)$. In the following, we will use these equations to describe the accretion of mono-energetic particles and the accretion of particles following a Maxwell-Boltzmann distribution.

Mono-energetic distribution

We consider the radial infall of mono-energetic particles with energy $E_0 \geq E_{\rm min} = \Phi(R)$. Since there is no angular momentum in this case, the distribution function is

$$F(E) = f_0\,\delta(E - E_0) = f_0\,\delta\left(\frac{p_r^2}{2m} + \Phi(r) - E_0\right), \tag{4.8}$$

where f_0 is a constant with units of [time]$^{-1}$ (because the radial distribution function, $f = f(r, p_r)$, has units of [length $\times$ momentum]$^{-1}$) which is related to n_R [see Eq. (4.13)]. Next, we can use the properties of the Dirac delta distribution[1] to rewrite the distribution function as:

$$f(r, p_r) = f_0 \sqrt{\frac{m}{2}}\,\frac{\delta\left(p_r + \sqrt{2m[E_0 - \Phi(r)]}\right)}{\sqrt{E_0 - \Phi(r)}}, \tag{4.9}$$

where we have used the fact that all particles are infalling and hence they can only have a negative momentum. According to Eqs. (4.5-4.7) and the boundary condition $n(R) = n_R$, the particle density, the average radial velocity and the accretion rate are, respectively:

$$n(r) = \frac{f_0}{r^2}\sqrt{\frac{m}{2[E_0 - \Phi(r)]}}, \tag{4.10}$$

$$u^r(r) = -\sqrt{\frac{2[E_0 - \Phi(r)]}{m}}, \tag{4.11}$$

$$|\dot{M}| = 4\pi r^2 m n(r) |u^r(r)| = 4\pi m f_0, \tag{4.12}$$

where

$$f_0 = R^2 n_R \sqrt{\frac{2[E_0 - \Phi(R)]}{m}}, \tag{4.13}$$

[1] The composition of the Dirac delta distribution with a smooth function $g(x)$, is given by $\delta(g(x)) = \sum_i \frac{\delta(x - x_i)}{|g'(x_i)|}$, where the sum goes over all the different roots x_i of g.

which yields

$$\frac{|\dot{M}|}{mn_R} = 4\pi R^2 \sqrt{\frac{2\left[E_0 - \Phi(R)\right]}{m}}, \tag{4.14}$$

valid for $r \leq R$.

If $E_0 = 0$ and the gravitational potential is due to a central mass such that $\Phi(r) \sim 1/r$, Eq. (4.11) is easily recognized as the free-fall velocity. Furthermore, we see from Eqs. (4.10) and (4.11) that the particle number density and velocity are proportional to $r^{-3/2}$ and $r^{-1/2}$, respectively, which is the expected behaviour for the fluid limit (Shapiro and Teukolsky 1983).

Finally, note that if we set $E_0 = \Phi(R) + \frac{1}{2}mv_R^2$, where $v_R = u^r(R)$ is the speed of the particles at the injection radius with respect to the central object, then Eq. (4.14) can be written as the well-known expression

$$\frac{|\dot{M}|}{mn_R v_R} = 4\pi R^2. \tag{4.15}$$

Maxwell-Boltzmann distribution

Another scenario consists of the radial infall of a stationary cloud of particles described by a Maxwell-Boltzmann distribution function (see e.g. Binney and Tremaine 2008),

$$f(r, p_r) = A \exp\left[-\beta\left(\frac{p_r^2}{2m} + \Phi(r)\right)\right], \tag{4.16}$$

where as usual $\beta = 1/k_{\mathrm{B}}T$, with $k_{\mathrm{B}} = 1.38 \times 10^{-23}\,\mathrm{m^2\,kg\,K^{-1}\,s^{-2}}$ the Boltzmann constant, T the temperature of the cloud and A is a constant with units of [length $\times$ momentum]$^{-1}$. In this case, using Eqs. (4.5-4.7) and the boundary condition $n(R) = n_R$, the particle number density, the average radial velocity and the accretion rate for $r \leq R$ are, respectively:

$$\begin{aligned} n(r) &= \frac{A}{r^2}\sqrt{\frac{m\pi}{2\beta}}\, e^{-\beta\Phi(r)} \\ &\quad \times \left[1 - \mathrm{Erf}\left(\sqrt{\beta\left[\Phi(R) - \Phi(r)\right]}\right)\right], \end{aligned} \tag{4.17}$$

$$\begin{aligned} u^r(r) &= -\sqrt{\frac{2}{\beta m \pi}}\, e^{-\beta[\Phi(R) - \Phi(r)]} \\ &\quad \times \left[1 - \mathrm{Erf}\left(\sqrt{\beta\left[\Phi(R) - \Phi(r)\right]}\right)\right]^{-1}, \end{aligned} \tag{4.18}$$

$$|\dot{M}| = 4\pi r^2 m n(r) |u^r(r)| = 4\pi m \frac{A}{\beta} e^{-\beta\Phi(R)}, \tag{4.19}$$

where $\mathrm{Erf}(x)$ denotes the error function, and

$$A = n_R R^2 \sqrt{\frac{2\beta}{m\pi}} e^{\beta\Phi(R)}, \tag{4.20}$$

which yields

$$\frac{|\dot{M}|}{m n_R} = 4\pi R^2 \sqrt{\frac{2}{\pi m \beta}} = 4\pi R^2 \sqrt{\frac{2}{\pi}\frac{k_\mathrm{B} T}{m}}. \tag{4.21}$$

4.1.2 Relativistic limit

In the relativistic case, we consider a Vlasov gas on a Schwarzschild background (1.13), whose temporal and radial metric components are characterized by the function

$$\alpha(r)^2 := 1 - \frac{r_\mathrm{S}}{r}, \tag{4.22}$$

with $r_\mathrm{S} = 2GM/c^2$ the Schwarzschild radius. The volume element in momentum space takes the same form as in Eq. (4.1), but now p^t is related to the relativistic energy E through [see Eq. (1.18)]

$$E = \alpha(r)^2 c\, p^t. \tag{4.23}$$

Combining the on-shell condition (1.6) for radial infall ($p_\theta = p_\phi = 0$) with Eq. (4.23), we can obtain another expression for the relativistic energy:

$$E = \sqrt{[\alpha(r)^2 p_r c]^2 + \alpha(r)^2 m^2 c^4}. \tag{4.24}$$

The minimum possible energy of a particle at radius $r = R$ is achieved when it has zero momentum, so that $E_\mathrm{min}(R) = \alpha(R) mc^2$ [cf. Eq. (1.21)]. Setting $E = E_\mathrm{min}$ in Eq. (4.24), give us the minimum magnitude of radial momentum possible for infalling particles as a function of the radius r,

$$p_\mathrm{m}(r,R) := -\frac{mc}{\alpha(r)^2}\sqrt{\alpha(R)^2 - \alpha(r)^2}. \tag{4.25}$$

Naturally, this definition reduces to Eq. (4.4) in the non-relativistic limit.

Additionally, the spherical symmetry and the zero angular momentum of the particles imply a distribution function of the form (4.2). Therefore, using Eqs. (3.14) and (3.18) we find

$$J^t(r) = \frac{c}{r^2}\int_{-\infty}^{p_{\rm m}(r,R)} f(r,p_r)\,dp_r\,, \tag{4.26}$$

$$J^r(r) = \frac{c}{r^2}\int_{-\infty}^{p_{\rm m}(r,R)} f(r,p_r)\,\frac{p^r}{p^t}\,dp_r, \tag{4.27}$$

$$n(r) = \frac{1}{c}\sqrt{[\alpha(r)J^t(r)]^2 - [J^r(r)/\alpha(r)]^2}. \tag{4.28}$$

The boundary conditions are given by the particle number density at the injection sphere $n(R) = n_R$, and the energy or temperature as before. As in the non-relativistic case, this set of equations can be applied to any steady, spherically symmetric distribution function describing a radial infall of particles onto a Schwarzschild BH from finite radius. In the following, we will use these equations to describe the accretion of mono-energetic particles and the accretion of particles following a Maxwell-Jüttner-type distribution.

Mono-energetic distribution

We reconsider a Vlasov gas of mono-energetic particles with relativistic energy $E_0 \geq E_{\rm min} = \alpha(R)mc^2$. The expected distribution function is:

$$F(E) = f_0\,\delta(E - E_0), \tag{4.29}$$

where, again, f_0 is a constant with units of [time]$^{-1}$ and is related to n_R [see Eq. (4.34)]. Using Eq. (4.24), we can rewrite the distribution function (4.29) as:

$$\begin{aligned} f(r,p_r) &= f_0\,\delta\left(\sqrt{[\alpha(r)^2\,p_r\,c]^2 + \alpha(r)^2\,m^2c^4} - E_0\right) \\ &= \frac{f_0\,\delta\left(p_r + \frac{mc}{\alpha(r)^2}\sqrt{\left(\frac{E_0}{mc^2}\right)^2 - \alpha(r)^2}\right)}{c\,\alpha(r)^2\sqrt{1-\alpha(r)^2\left(\frac{mc^2}{E_0}\right)^2}}, \end{aligned} \tag{4.30}$$

where we have used the fact that all the particles have negative radial momentum. With this distribution function and the boundary condition $n(R) = n_R$, we can calculate the invariant particle number density, the average radial velocity and the mass accretion rate with Eqs. (3.31,

4.26-4.28),

$$n(r) = \frac{f_0}{r^2 c}\left[\left(\frac{E_0}{mc^2}\right)^2 - \alpha(r)^2\right]^{-1/2}, \tag{4.31}$$

$$u^r(r) = -c\left[\left(\frac{E_0}{mc^2}\right)^2 - \alpha(r)^2\right]^{1/2}, \tag{4.32}$$

$$|\dot{M}| = 4\pi m f_0, \tag{4.33}$$

valid for $r \leq R$, and with f_0 given by

$$f_0 = n_R\, cR^2\sqrt{\left(\frac{E_0}{mc^2}\right)^2 - \alpha(R)^2}, \tag{4.34}$$

which yields

$$\frac{|\dot{M}|}{mcn_R} = 4\pi R^2\sqrt{\left(\frac{E_0}{mc^2}\right)^2 - \alpha(R)^2}. \tag{4.35}$$

Note that, employing Eq. (4.32), we get the familiar result

$$\frac{|\dot{M}|}{mn_R u^r(R)} = 4\pi R^2, \tag{4.36}$$

as follows directly from integrating the continuity equation for radially infalling dust in which case $\rho = mn$.

Nevertheless, for our purposes it is convenient to express the accretion rate in terms of the 3-velocity v_R of the gas particles calculated by a static observer at the shell $r = R$, rather than the radial component of the four velocity $u^r(R)$, because the injection sphere is static with respect to the black hole. The relation between v_R and $u^r(R)$ is given by (see e.g. Crawford and Tereno 2002)

$$u^r(R) = \alpha(R)\, v_R\, \gamma, \tag{4.37}$$

where $\gamma := (1 - v_R^2/c^2)^{-1/2}$ is the Lorentz factor associated with v_R. In this way, the accretion rate is

$$\frac{|\dot{M}|}{mn_R v_R} = 4\pi R^2 \alpha(R)\gamma. \tag{4.38}$$

In the non-relativistic limit, with $v_R \ll c$ and $r_S \ll R$, the previous equations reduce to Eqs. (4.10-4.15), as expected.

Maxwell-Jüttner-type distribution

We now consider a distribution function of the Maxwell-Jüttner-type,[2]

$$F(E) = A\, e^{-\beta E}, \tag{4.39}$$

where A is a constant with units of [length $\times$ momentum]$^{-1}$, $\beta = 1/k_{\rm B}T$, T is the temperature of the gas at the injection sphere and E is the relativistic energy.[3]

Applying Eqs. (4.26-4.28) with E given by Eq. (4.24) in terms of the variables (r, p_r), the resulting integrals have no analytical closed form. Nevertheless, we can make a change of integration variable from p_r to E through Eq. (4.24), which will result in closed solutions. In this way, for the Schwarzschild metric we get

$$J^0(r) = \frac{1}{\alpha(r)^2 r^2} \int_{\alpha(R)mc^2}^{\infty} F(E)\, \frac{E}{\sqrt{E^2 - \alpha(r)^2 m^2 c^4}}\, dE, \tag{4.40}$$

$$J^r(r) = \frac{1}{r^2} \int_{\alpha(R)mc^2}^{\infty} F(E)\, dE. \tag{4.41}$$

(This set of equations can also be applied to the distribution function in Eq. (4.29) and the resulting expressions are again Eqs. (4.31-4.35).) For the distribution function in Eq. (4.39), we obtain

$$n_R = \frac{Amc}{R^2}\, \frac{\sqrt{\mathbf{K}_1(z)^2 e^{2z} - z^{-2}}}{e^z}, \tag{4.42}$$

$$u^r(R) = -\frac{1}{\beta mc}\, \frac{1}{\sqrt{\mathbf{K}_1(z)^2 e^{2z} - z^{-2}}}, \tag{4.43}$$

$$|\dot{M}| = 4\pi m \frac{A}{\beta} e^{-z}, \tag{4.44}$$

where $z \coloneqq mc^2 \alpha(R)\beta$ and $\mathbf{K}_1(z)$ is the modified Bessel function of the second kind and of first order (see e.g. Abramowitz and Stegun 1964). Note that the previous expressions are evaluated at $r = R$; this was necessary to get the analytical closed form (the accretion rate is not affected since it is a constant). Eliminating A, we get an expression for the accretion rate

$$\frac{|\dot{M}|}{mcn_R} = \frac{4\pi R^2 \alpha(R)}{\sqrt{[\mathbf{K}_1(z) z e^z]^2 - 1}}. \tag{4.45}$$

[2] As we mentioned in Section 3.1.1, the Maxwell-Jüttner distribution function is the relativistic generalization of the Maxwell-Boltzmann distribution.

[3] Strictly speaking, the distribution function described by (4.39) does not describe a configuration in thermodynamical equilibrium since in this section we restrict all the particles to have zero angular momentum.

Finally, considering the non-relativistic limit $mc^2 \gg k_{\rm B}T$, so that $z \gg 1$, we obtain:

$$\frac{|\dot{M}|}{mcn_R} \approx 4\pi R^2 \alpha(R) \sqrt{\frac{2}{\pi z}} = 4\pi R^2 \sqrt{\frac{2\alpha(R)}{\pi} \frac{k_{\rm B}T}{mc^2}}, \tag{4.46}$$

which reduces to the expression in Eq. (4.21) when $R \gg r_{\rm S}$.

A final remark can be done with respect to the purely radial infall from finite radius. For both the non-relativistic and relativistic limits, the accretion rate is proportional to R^2, hence it diverges as $R \to \infty$. This means that these models do not have a well-defined Bondi-type formula which relates the mass accretion rate to the properties of the gas at infinity (cf. with Eq. (2.6) which is defined in terms of variables at infinity). This is analogous to the case of accretion of pure dust in spherical symmetry, in which the only steady-state solution has vanishing mass density at infinity (Chaverra and Sarbach 2015). In fact, our mono-energetic model with purely radial infall does correspond precisely to this simple dust model, since its velocity dispersion is exactly zero (because all the particles are falling radially from the same radius with equal conditions).

4.2 Accretion with angular momentum

In this section we allow for the individual gas particles to have angular momentum. However, we assume that the averaged quantities describing the gas (i.e. the space-time observables) still have spherical symmetry. For simplicity, we shall assume a uniform distribution in the total angular momentum L. To apply our derived formulae, we employ the same mono-energetic and Maxwell-Jüttner-type distribution functions as considered in the previous section. In contrast to Section 4.1, we will derive the non-relativistic limits of accretion from finite radius by using approximations in the analytical results obtained for the relativistic limit.

4.2.1 Relativistic and non-relativistic limits

We consider the Schwarzschild metric (1.13) associated with a BH of mass M. We assume that the injection sphere is located at a radius R greater than the radius of the innermost stable circular orbit $r_{\rm ISCO}$ (see Section 1.3.1), that is $R > r_{\rm ISCO} = 6GM/c^2$ (it will become clear in a moment why this restriction is required). As in Section 4.1, we impose the particle number density n_R on the injection sphere, and we compute the accretion rate satisfying this boundary condition.

For the following, it is convenient to express the four-momentum p^μ in terms of *orthonormal components* $p^{\hat{\mu}}$ ($\hat{\mu} = 0,1,2,3$), defined by

$$p^0 = \alpha(r)p^t, \qquad p^1 = \frac{p^r}{\alpha(r)}, \qquad p^2 = r\,p^\theta, \qquad p^3 = r\sin\theta\,p^\phi, \tag{4.47}$$

with $\alpha(r)^2 = 1 - \dfrac{r_S}{r}$ as before, and such that

$$-m^2c^2 = p\cdot p = g_{\mu\nu}p^\mu p^\nu = \eta_{\mu\nu}p^{\hat{\mu}}p^{\hat{\nu}}, \tag{4.48}$$

where in the last step we have used the Schwarzschild metric (1.13) and Eqs. (4.47). In terms of these orthonormal components, the volume element (3.15) is

$$\mathrm{dvol}_x(p) = \frac{dp^1dp^2dp^3}{\sqrt{m^2c^2 + (p^1)^2 + (p^2)^2 + (p^3)^2}}. \tag{4.49}$$

Since the spherical symmetry and the steady assumption allow us to write the distribution function as a function of the integrals of motion (E,L), it is convenient to write the volume element (4.49) in terms of these variables. To proceed in this direction, we start by noting from Eqs. (4.23) and (4.47) that

$$p^0 = \frac{E}{c\,\alpha(r)}. \tag{4.50}$$

Next, from Eqs. (1.28) and (4.47) we find

$$p^1 = \pm\frac{\sqrt{E^2 - V_L(r)}}{c\,\alpha(r)}, \tag{4.51}$$

where the $\pm$ sign in p^1 determines whether the particle is outgoing or infalling, respectively, and $V_L(r)$ is the effective potential (1.27) describing the radial motion. For the angular variables, we remember from Hamiltonian mechanics that the total angular momentum L is given by

$$L^2 = p_\theta^2 + \frac{p_\phi^2}{\sin^2\theta}, \tag{4.52}$$

which suggests a parametrization of the (p_θ, p_ϕ)–space in terms of the variables (χ, L), defined by

$$p_\theta = L\cos\chi, \qquad p_\phi = L\sin\theta\sin\chi, \tag{4.53}$$

with $\chi \in [0, 2\pi)$. Using Eqs. (4.47) and (4.53), we find

$$p^2 = \frac{L\cos\chi}{r}, \qquad p^3 = \frac{L\sin\chi}{r}. \tag{4.54}$$

In this way, the orthonormal components of the four-momentum and the volume element expressed in terms of the integrals of motion (E, L) and the angle χ, are given by

$$(p^{\hat{\mu}}_{\pm}) = \left(\frac{E}{c\,\alpha(r)}, \pm\frac{\sqrt{E^2 - V_L(r)}}{c\,\alpha(r)}, \frac{L\cos\chi}{r}, \frac{L\sin\chi}{r} \right), \tag{4.55}$$

$$\mathrm{dvol}_x(p) = \frac{L\,dE\,dL\,d\chi}{r^2\sqrt{E^2 - V_L(r)}}, \tag{4.56}$$

where the new expression for the volume element is obtained with the Jacobian of the transformation $(p^1, p^2, p^3) \to (E, L, \chi)$.

The energy and angular momentum of the particles determine if they are going to be absorbed by the BH or scattered by the centrifugal barrier (see Section 1.3.2 for a discussion of the dynamics of massive test particles in Schwarzschild space-time). Absorbed particles necessarily have incoming trajectories (particles with momentum $p^{\hat{\mu}}_{-}$), but scattered particles have both incoming and outgoing trajectories (particles with momentum $p^{\hat{\mu}}_{\pm}$). This behavior is illustrated in Fig. 4.1, where we can see that if the particle's energy E^2 exceeds the local maximum of V_L, then we will only have incoming absorbed particles with momentum $p^{\hat{\mu}}_{-}$, and values of E^2 less than this maximum give rise to incoming and outgoing scattered particles with momenta $p^{\hat{\mu}}_{\pm}$.

In this way, the particle current density J is composed by absorbed and scattered particles,

$$J = J_{\mathrm{abs}} + J_{\mathrm{sca}}, \tag{4.57}$$

where, again, the particle current density J_{abs} is associated to particles with $p^{\hat{\mu}}_{-}$, and J_{sca} contains particles with both $p^{\hat{\mu}}_{\pm}$. To determine explicitly these currents we must use Eqs. (3.14), (4.55) and (4.56). However, first we need to know the integration limits associated to E, L and χ for particles coming from the injection sphere at radius R. The range for χ is $[0, 2\pi)$ due to the spherical symmetry. The ranges for E and L were discussed in Section 1.3.2, where we obtained the following characterization of the parameter space (E, L) of massive test particles orbiting a Schwarzschild BH:

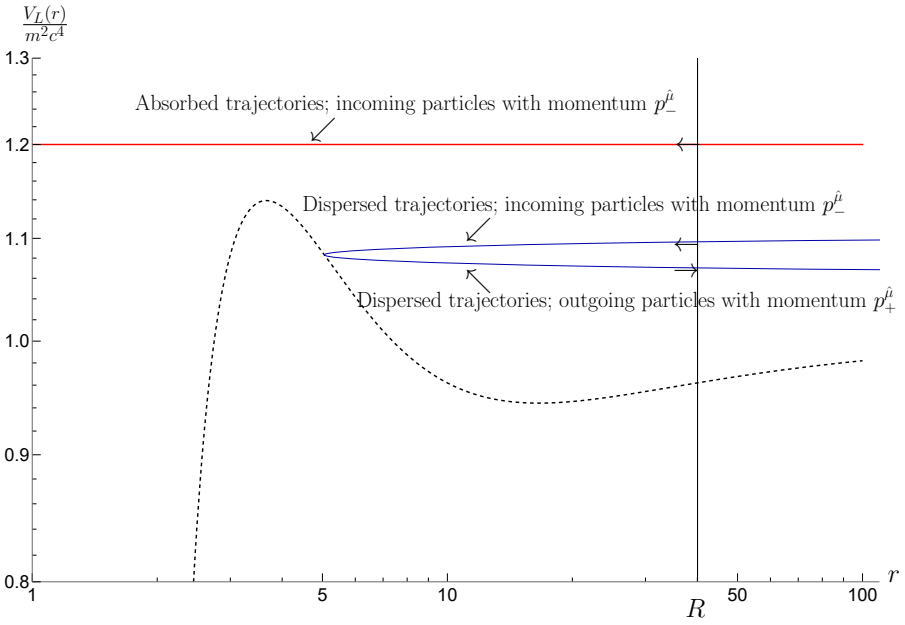

Fig. 4.1 Plot of the Schwarzschild effective potential $V_L(r)$ vs r (with r in units of r_S) and $L = 4.5GMm/c$. We have identified for the absorbed trajectories the incoming moments by $p^{\hat{\mu}}_{-}$, while for the scattered trajectories the incoming moments are $p^{\hat{\mu}}_{-}$ and the outgoing moments are $p^{\hat{\mu}}_{+}$ [see Eq. (4.55)]. For more details on the effective potential of Schwarzschild space-time and the dynamics of massive test particles see Section 1.3.2. [*Adapted plot from a previous version made by Carlos Gabarrete.*]

1. *Absorbed particles*

$$\begin{cases} \alpha(R)\,mc^2 \leq E < E_c(R) \quad \text{and} \quad 0 \leq L \leq L_{\max}(E,R), \\ E_c(R) < E < \infty \quad \text{and} \quad 0 \leq L < L_c(E). \end{cases}$$

2. *Scattered particles*

$$E_c(R) \leq E < \infty \quad \text{and} \quad L_c(E) < L < L_{\max}(E,R).$$

Since the distribution functions considered in this work depend only on E, this characterization is very appropriate because one can fix a value of E and perform the integrals over L explicitly. Thus, considering this characterization, the orthonormal components of the particle current densities are

$$J^{\hat{\mu}}_{\text{abs}}\Big|_{r=R} = c \int_{\alpha(R)mc^2}^{E_c(R)} \int_0^{L_{\max}(E,R)} \int_0^{2\pi} \frac{p^{\hat{\mu}}_{-} F(E)\, L\, dE\, dL\, d\chi}{R^2\sqrt{E^2 - V_L(R)}} + c \int_{E_c(R)}^{+\infty} \int_0^{L_c(E)} \int_0^{2\pi} \frac{p^{\hat{\mu}}_{-} F(E)\, L\, dE\, dL\, d\chi}{R^2\sqrt{E^2 - V_L(R)}}, \tag{4.58}$$

$$J^{\hat{\mu}}_{\rm sca}\Big|_{r=R} = c\sum_{\pm}\int_{E_{\rm c}(R)}^{+\infty}\int_{L_{\rm c}(E)}^{L_{\rm max}(E,R)}\int_{0}^{2\pi}\frac{p^{\hat{\mu}}_{\pm}F(E)\,L\,dE\,dL\,d\chi}{R^2\sqrt{E^2-V_L(R)}}, \tag{4.59}$$

with $p^{\hat{\mu}}_{\pm}$ given by Eq. (4.55). From Eqs. (3.14) and (4.47) we note that the orthonormal components of the particle current density (J^0, J^i) are related to the usual spherical components $(J^t, J^r, J^\theta, J^\phi)$ in the following way

$$J^0 = \alpha(r)J^t, \qquad J^1 = \frac{J^r}{\alpha(r)}, \qquad J^2 = rJ^\theta, \qquad J^3 = r\sin\theta\, J^\phi. \tag{4.60}$$

Now, we note from Eq. (4.59) that

$$J^1_{\rm sca}\big|_{r=R} = 0, \tag{4.61}$$

because the terms p^1_+ and p^1_- cancel each other out in Eq. (4.59). Therefore, *only the absorbed trajectories contribute to the mass accretion rate* since $\dot{M} = 4\pi r^2 m\,\alpha(r)J^1(r)$ [cf. Eqs. (3.31) and (4.60); also see Eq. (4.65)]. In contrast to this, all the trajectories (absorbed and scattered) contribute to the particle number density n_R. To see this, we compute the rest of the orthonormal components of the particle current density. The non-vanishing terms yield

$$J^0_{\rm abs}\big|_{r=R} = \frac{2\pi}{\alpha(R)^3c^2}\left\{\int_{mc^2\alpha(R)}^{+\infty} E\sqrt{E^2-m^2c^4\alpha(R)^2}\,F(E)\,dE - \int_{E_{\rm c}(R)}^{+\infty} E\sqrt{E^2-V_{\rm c}(E,R)}\,F(E)\,dE\right\}, \tag{4.62}$$

$$J^1_{\rm abs}\big|_{r=R} = -\frac{\pi}{R^2\alpha(R)}\left\{\int_{mc^2\alpha(R)}^{E_{\rm c}(R)} L_{\rm max}(E,R)^2\,F(E)\,dE + \int_{E_{\rm c}(R)}^{+\infty} L_{\rm c}(E)^2\,F(E)\,dE\right\}, \tag{4.63}$$

$$J^0_{\rm sca}\big|_{r=R} = \frac{4\pi}{\alpha(R)^3c^2}\int_{E_{\rm c}(R)}^{+\infty} E\sqrt{E^2-V_{\rm c}(E,R)}\,F(E)\,dE, \tag{4.64}$$

where we have introduced the shorthand notation $V_{\rm c}(E,R) := V_{L_{\rm c}(E)}(R)$. Note that, when $R\to\infty$, then $V_{L_{\rm c}(E)}(R)\to m^2c^4$ and $E_{\rm c}(R)\to mc^2$ [see Eqs. (1.27), (1.45) and (1.39)]; hence *only the scattered particles yield a non-vanishing contribution to* $J^\mu\big|_{r=R}$ *when* $R\to\infty$, since in Eq. (4.62) both integrals cancel each other out and the R^2 in the denominator of Eq. (4.63) makes $J^1_{\rm abs}\big|_{r=R\to\infty} = 0$.

Finally, using

$$J^r\big|_{r=R} = \alpha(R)\,(J^1_{\rm abs}+J^1_{\rm sca})\big|_{r=R} = \alpha(R)\,J^1_{\rm abs}\big|_{r=R}, \tag{4.65}$$

and employing Eqs. (3.31) and (4.62)–(4.64), we obtain the mass accretion rate

$$\dot{M} = 4\pi m R^2 \, J^r|_{r=R} = -4\pi^2 m \left\{ \int_{mc^2\alpha(R)}^{E_c(R)} L_{\rm max}(E,R)^2 F(E) dE + \int_{E_c(R)}^{+\infty} L_c(E)^2 F(E) dE \right\}, \tag{4.66}$$

and the particle number density at $r = R$,

$$n_R = \frac{1}{c}\sqrt{\left[J^0_{\rm abs}(R) + J^0_{\rm sca}(R)\right]^2 - \left[J^1_{\rm abs}(R)\right]^2}, \tag{4.67}$$

which is composed by both absorbed and scattered particles, as we said earlier.

To compute these expressions we need an explicit form of the distribution function $F(E)$ and the expressions for $L_c(E)$ and $L_{\rm max}(E,R)$, given by Eqs. (1.39) and (1.41). In the following, we further analyze these results for the mono-energetic and Maxwell-Jüttner-type distributions in the energy.

Mono-energetic distribution

First, it is convenient to obtain an expression for the energy E_0 of a gas particle measured by a static observer at the injection sphere (see the radial analogue in Section 4.1.2). At $r = R$ we expect that, locally, $p^0 = m\gamma c$ and $p^i = m\gamma u^i$, where we recall that $\gamma = (1 - v_R^2/c^2)^{-1/2}$ is the Lorentz factor associated with the 3-velocity of the gas particles measured by the static observer at R. Hence,

$$\frac{|\vec{p}|^2}{(p^0)^2} = \frac{m^2\gamma^2|\vec{v}_R|^2}{m^2\gamma^2 c^2} = \frac{|\vec{v}_R|^2}{c^2}, \tag{4.68}$$

with $|\vec{p}|^2 \equiv (p^1)^2 + (p^2)^2 + (p^3)^2$. Substituting the orthonormal components of the momentum given in Eq. (4.55), we get

$$E_0 = mc^2\alpha(R)\gamma. \tag{4.69}$$

This is a relation between the energy and the Lorentz factor, which we will use to express our results.

Now, for the mono-energetic model $F(E) = f_0\,\delta(E - E_0)$, one obtains from Eqs. (4.66), (4.67) and (4.69)

$$\frac{|\dot{M}|}{mcn_R} = 4\pi R^2 \alpha(R) \times \begin{cases} \sqrt{\dfrac{\gamma^2-1}{3\gamma^2+1}} \quad \text{for} \quad 1 < \gamma < \gamma_{\rm c}(R), & \text{(4.70a)} \\ \dfrac{h(R,\gamma)}{\left[4\gamma^2\left(\sqrt{\gamma^2-1}+\sqrt{\gamma^2-1-h(R,\gamma)}\right)^2 - h(R,\gamma)^2\right]^{1/2}} \\ \quad \text{for} \quad \gamma > \gamma_{\rm c}(R), & \text{(4.70b)} \end{cases}$$

where $\gamma_{\rm c}(R) \coloneqq E_{\rm c}(R)/[mc^2\alpha(R)]$ and h denotes the function

$$h(R,\gamma) \coloneqq \left[\frac{L_{\rm c}(E_0)}{mcR}\right]^2 = \frac{8r_{\rm S}^2}{R^2}\,\frac{1}{36\,\alpha^2\gamma^2 - 8 - 27\alpha^4\gamma^4 + \alpha\gamma[9\alpha^2\gamma^2-8]^{3/2}}. \tag{4.71}$$

Eqs. (4.70a) and (4.70b) generalize the Bondi-type formula (which can be found, for instance in Chapter 14, Section 2 of Shapiro and Teukolsky 1983) to the accretion of a mono-energetic gas of arbitrary energy $E_0 > mc^2\alpha(R)$ accreting from a sphere of finite radius $R > r_{\rm ISCO}$.

In the limit $R \to \infty$, it follows that $E_{\rm c}(R) \to mc^2$ [see Eq. (1.45)] so that $\gamma_{\rm c}(R) \to 1$ and Eq. (4.70b) reduces to

$$\frac{|\dot{M}|}{mcn_\infty} = \frac{\pi L_{\rm c}^2(mc^2\gamma_\infty)}{m^2c^2\gamma_\infty\sqrt{\gamma_\infty^2-1}} = \frac{16\pi G^2M^2}{c^3 v_\infty}\left[1 + \frac{v_\infty^2}{c^2} - \frac{v_\infty^4}{c^4} + \mathscr{O}\left(\frac{v_\infty^6}{c^6}\right)\right], \tag{4.72}$$

where $n_\infty \coloneqq \lim_{R\to\infty} n_R$, $v_\infty \coloneqq \lim_{R\to\infty} v_R$, and $\gamma_\infty \coloneqq \lim_{R\to\infty} \gamma_R$.

The leading-order term of Eq. (4.72) in v_∞/c, agrees with the Zeldovich-Novikov accretion rate for mono-energetic particles [Eq.(13.2.2) of Zeldovich and Novikov 1971] given by[4]

$$\dot{M} = \frac{16\pi G^2M^2}{c^2}\frac{\rho_\infty}{v_\infty}, \tag{4.73}$$

which represents the relativistic accretion of a collisionless kinetic gas onto a Schwarzschild BH from $R \to \infty$.

Using the fact that for $E = E_{\rm c}(R)$ one has $L_{\rm c}(E_{\rm c}) = L_{\max}(E_{\rm c}, R)$, it is simple to verify that $|\dot{M}|$ given by Eqs. (4.70a) and (4.70b) is continuous at the transition point $\gamma = \gamma_{\rm c}(R)$, where it

[4]The standard derivation of this result with an emphasis on Kinetic Theory can be found in the book of Shapiro and Teukolsky (1983), particularly Eq. (14.2.20).

has the value

$$\frac{|\dot{M}|}{mcn_R} = \frac{4\pi r_S R\alpha(R)}{\sqrt{1+\frac{2r_S}{R}}}. \tag{4.74}$$

In fact, for fixed R, $|\dot{M}|$ is a monotonically increasing function of γ in the interval $1<\gamma<\gamma_c(R)$, while it decreases monotonically for $\gamma>\gamma_c(R)$. Thus, *Eq.* (4.74) *is the maximum accretion rate for the mono-energetic model with angular momentum.*

Comparing Eq. (4.70a) with the corresponding expression for the mass accretion rate in the absence of angular momentum (4.35), the difference relies in the factor $(3\gamma^2+1)^{-1/2}\leq 1$ which implies that for $\gamma<\gamma_c(R)$ the accretion rate is smaller when angular momentum is considered. This is expected since the tangential movement of particles with angular momentum reduces the net infall of particles. Note that in the non-relativistic limit $\gamma\to 1$ for fixed R one obtains half the value given in Eq. (4.38) computed for the purely radial infall. In other words, by setting $v_R\to 0$ one does not recover the same accretion rate for purely radial infall; it appears an extra factor of $1/2$. As further analyzed in Appendix A, this is due to the fact that when angular momentum is present, the three-velocity contains non-trivial angular components.

A simplified form of Eqs. (4.70a, 4.70b) can be obtained in the limit when the injection sphere is far from the horizon ($R\gg r_S$) and for non-relativistic energies, such that $v_R\ll c$. For this, one notices that

$$\gamma_c(R)-1 = 2\left(\frac{r_S}{R}\right)^2+\mathscr{O}\left(\frac{r_S}{R}\right)^3, \tag{4.75}$$

and that the denominator of the second factor on the right-hand side of (4.71) converges to 2 when $\alpha(R)\to 1$ and $\gamma\to 1$. Using this, one finds to leading order,

$$\frac{|\dot{M}|}{mcn_R} = 4\pi R^2\times\begin{cases}\dfrac{v_R}{2c} & \text{for}\quad \dfrac{v_R}{2c}<\dfrac{r_S}{R}, & \text{(4.76a)}\\[2ex] \dfrac{2c}{v_R}\left(\dfrac{r_S}{R}\right)^2\dfrac{1}{1+\sqrt{1-\left(\frac{2c}{v_R}\frac{r_S}{R}\right)^2}} & \text{for}\quad \dfrac{v_R}{2c}>\dfrac{r_S}{R}, & \text{(4.76b)}\end{cases}$$

which is valid for $R\gg r_S$ and $v_R\ll c$. Therefore, Eqs. (4.76a) and (4.76b) represent the non-relativistic limit of the accretion of a collisionless mono-energetic kinetic gas onto a Schwarzschild BH from finite radius.

In Fig. 4.2 we show the behaviour of the dimensionless quantity $\Gamma=|\dot{M}|/(4\pi R^2\alpha(R)mcn_R)$ as a function of γ for different values of R (or, equivalently, Γ as a function of the velocity v_R). As can be observed from this figure, $|\dot{M}|$ increases for small values of γ (or small velocities v_R), the quantity Γ being independent of R, as follows from Eq. (4.70a). Hence, in this regime the *qualitative* behavior of the accretion rate as a function of v_R is similar to the case of

purely radial infall (Eq. (4.38); the only difference consisting of the factor $(3\gamma^2+1)^{-1/2}$, as explained above) in which $|\dot{M}|$ increases linearly with γ. However, as soon as γ reaches the critical value $\gamma_c(R)$, $|\dot{M}|$ starts decreasing, converging to a finite (R-dependent value) in the limit $\gamma \to \infty$. This can be understood as follows: when $\gamma < \gamma_c(R)$, all the particles have their energy below the critical value $E_c(R)$ and thus all of them are absorbed by the BH. This leads to an accretion rate which increases with v_R. However, when $\gamma > \gamma_c(R)$, the particles have their energy lying above $E_c(R)$ and hence a fraction of them (namely, those with angular momentum larger than $L_c(E)$) are scattered off the effective potential, leading to a smaller accretion rate. As v_R increases this fraction becomes larger which leads to a smaller mass accretion rate (see Rioseco and Sarbach 2017b for a more extended discussion regarding this effect for a similar model with $R \to \infty$).

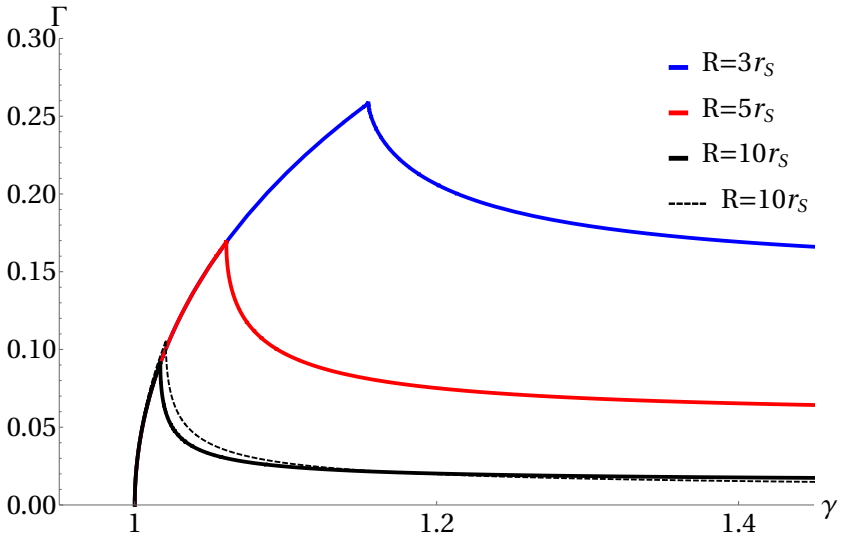

Fig. 4.2 The dimensionless quantity $\Gamma = |\dot{M}|/(4\pi R^2 \alpha(R) mcn_R)$ as a function of the Lorentz factor $\gamma = (1 - v_R^2/c^2)^{-1/2}$ for some fixed values of the injection sphere's radius R. The solid lines are computed from Eqs. (4.70a, 4.70b) for different values of R. The black dashed line shows the same quantity Γ for the case $R = 10r_S$, using the approximation from Eqs. (4.76a, 4.76b) which is valid for $R \gg r_S$ and non-relativistic velocities $v_R \ll c$. [*Plot made by Carlos Gabarrete.*]

Maxwell-Jüttner-type distribution

Next, we analyze the Maxwell-Jüttner-type distribution (4.39) which was also considered in Rioseco and Sarbach (2017a,b).[5] To understand this case, we define $z(R,T) := z = mc^2\beta\alpha(R)$,

[5] Again, one should be careful with associating T with temperature. Although in this section the gas particles are not restricted to zero angular momentum, the gas is still not in strict thermodynamic equilibrium at finite R because we are not considering hypothetical incoming particles emanating from the *white hole*. However, in the collisionless case, the Maxwell-Jüttner-type distribution (4.39) has physical sense. See the discussion in Section 4 of Rioseco and Sarbach (2017b).

and we perform the variable substitutions $E = mc^2\alpha(R)(1+x/z)$ and $E = E_c(R)(1+y/z)$ in the integrals shown in Eqs. (4.62, 4.63, 4.64). This yields

$$J^0 = \left(J^0_{\rm abs} + J^0_{\rm sca}\right)\big|_{r=R} = \frac{2\pi A m^3 c^4}{z^{3/2}} e^{-z} I_1(R,z), \tag{4.77}$$

$$J^1 = J^1_{\rm abs}\big|_{r=R} = -\frac{\pi A m^3 c^4}{z^2} e^{-z} I_2(R,z), \tag{4.78}$$

where $I_1(R,z)$ and $I_2(R,z)$ are given by

$$\begin{aligned} I_1(R,z) = &\int_0^\infty \left(1+\frac{x}{z}\right)\sqrt{2x+\frac{x^2}{z}}\,e^{-x}dx \\ &+ \gamma_c(R)^3 e^{-\Lambda(R,z)} \int_0^\infty \left(1+\frac{y}{z}\right) e^{-\gamma_c(R)y} \sqrt{z\left[1-\frac{V_c\left[E_c(R)\left(1+\frac{y}{z}\right),R\right]}{E_c(R)^2}\right]+2y+\frac{y^2}{z}}\,dy, \end{aligned} \tag{4.79}$$

$$I_2(R,z) = \int_0^{\Lambda(R,z)} \left(2x+\frac{x^2}{z}\right) e^{-x}dx + \frac{\gamma_c(R)}{R^2} z e^{-\Lambda(R,z)} \int_0^\infty \frac{L_c\left[E_c(R)\left(1+\frac{y}{z}\right)\right]^2}{m^2c^2} e^{-\gamma_c(R)y}dy, \tag{4.80}$$

where we recall the shorthand notation $\gamma_c(R) \coloneqq E_c(R)/(mc^2\alpha(R))$ and where we have set $\Lambda(R,z) \coloneqq (\gamma_c(R)-1)z$.

In this way, from Eqs. (4.66, 4.67, 4.77, 4.78) one obtains

$$\frac{|\dot{M}|}{mcn_R} = \frac{4\pi R^2\alpha(R)}{\sqrt{4z\left[\frac{I_1(R,z)}{I_2(R,z)}\right]^2 - 1}}. \tag{4.81}$$

This equation, together with the integrals defined in Eqs. (4.79, 4.80), provides an exact expression for the mass accretion rate as a function of the injection radius R and the temperature T. Unfortunately, the integrals involved are rather complicated and for this reason it is advantageous to obtain simplified expressions for certain limits. One such expression can be obtained assuming that the gas temperature is low, such that $k_B T \ll mc^2$, and that $R \gg r_S$. In order to discuss this limit, we first note that

$$1 - \frac{V_c\left[E_c(R)\left(1+\frac{y}{z}\right),R\right]}{E_c^2(R)} = -\frac{16 r_S^2}{R^2 - r_S^2}\frac{y}{z} + \mathscr{O}\left(\frac{y^2}{z^2}\right), \tag{4.82}$$

and hence for $z \gg 1$ one obtains

$$I_1(R,z) \approx \int_0^\infty \sqrt{2x} e^{-x} dx + \gamma_c(R)^3 e^{-\Lambda(R,z)} \int_0^\infty \sqrt{2y \frac{1-(3r_S/R)^2}{1-(r_S/R)^2}} e^{-\gamma_c(R)y} dy. \tag{4.83}$$

Now, the integrals in Eq. (4.83) can be evaluated explicitly which yields, for $z \gg 1$,

$$I_1(R,z) \approx \sqrt{\frac{\pi}{2}} \left[1 + \gamma_c(R)^{3/2} e^{-\Lambda(R,z)} \sqrt{\frac{1-(3r_S/R)^2}{1-(r_S/R)^2}} \right]. \tag{4.84}$$

Similarly,

$$I_2(R,z) \approx 2 - 2[1+\Lambda(R,z)] e^{-\Lambda(R,z)} + \frac{4r_S^2}{R^2[\gamma_c(R)-1]} \frac{\Lambda(R,z) e^{-\Lambda(R,z)}}{\alpha(R)^2 (1+3r_S/R)}, \tag{4.85}$$

for $z \gg 1$, where we have used that

$$\frac{L_c [E_c(R)]^2}{(mc)^2} = \frac{4r_S^2}{\alpha(R)^2 (1+3r_S/R)}, \tag{4.86}$$

which can be deduced from Eqs. (1.39) and (1.45). The expressions (4.84) and (4.85) are valid when $z \gg 1$, independent of the value of R.

When $R \gg r_S$ one can use the expansion (4.75) to show that

$$\Lambda(R,z) \approx 2 \left(\frac{r_S}{R} \right)^2 z. \tag{4.87}$$

Therefore, $\Lambda(R,z)$ depends on the ratio between the two large quantities z and R^2, implying that it varies over the whole range $(0,\infty)$. Assuming that $R \gg r_S$ in Eqs. (4.84) and (4.85) leads to a further simplification,

$$I_1(R,z) \approx \sqrt{\frac{\pi}{2}} \left[1 + e^{-\Lambda(R,z)} \right], \tag{4.88}$$

$$I_2(R,z) \approx 2 \left[1 - e^{-\Lambda(R,z)} \right], \tag{4.89}$$

which can be introduced into Eq. (4.81). In this way, one obtains the simple expression

$$\frac{|\dot{M}|}{mcn_R} \approx R^2 \alpha(R) \tanh \left(\frac{r_S^2}{R^2} z \right) \sqrt{\frac{32\pi}{z}}, \tag{4.90}$$

which is valid for arbitrary values of $R \gg r_S$ and $z = mc^2/(k_B T) \gg 1$. Eq. (4.90) represents the non-relativistic limit of the accretion of a collisionless kinetic gas described by a Maxwell-Boltzmann distribution[6] onto a Schwarzschild BH from finite radius.

In the limit $R \to \infty$, Eq. (4.90) gives

$$\frac{|\dot{M}|}{mcn_\infty} \approx \sqrt{32\pi z_\infty}\, r_S^2, \tag{4.91}$$

where $z_\infty := \lim_{R\to\infty} z$, which agrees with Eq. (87) in Rioseco and Sarbach (2017a).

In Fig. 4.3 we show the dimensionless quantity $\Gamma = |\dot{M}|/(4\pi R^2 \alpha(R) mcn_R)$ as a function of z^{-1} (or, equivalently, Γ as a function of the temperature T) for different values of R. The behavior is very similar to the one of the mono-energetic model, except that the function is smooth at the maximum value of the accretion rate, which is due to the non-trivial velocity dispersion in the distribution function.

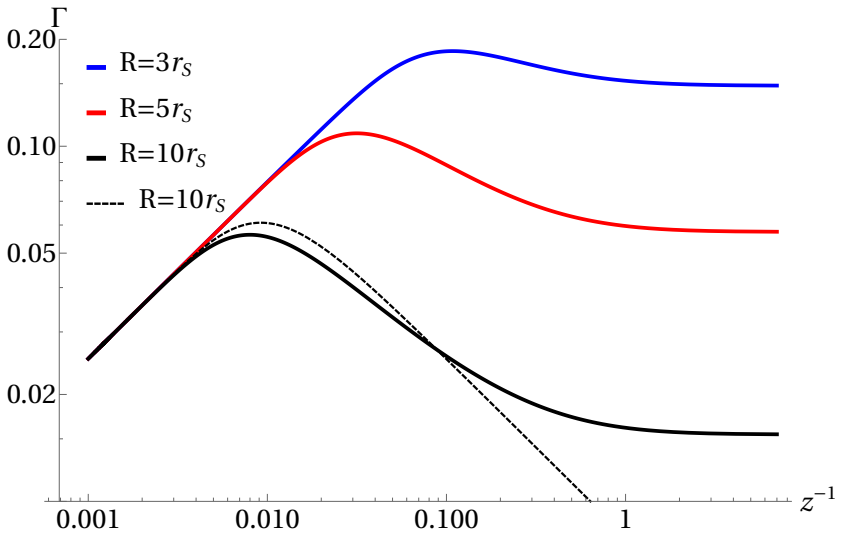

Fig. 4.3 The dimensionless quantity $\Gamma = |\dot{M}|/(4\pi R^2 \alpha(R) mcn_R)$ as a function of $z^{-1} = k_B T/(mc^2 \alpha(R))$ for some fixed values of the radius R of the injection sphere. The solid lines are computed from Eq. (4.81) for different values of R. The black dashed line shows the same quantity Γ for the case $R = 10r_S$, using the approximation from Eq. (4.90) which is valid for $R \gg r_S$ and non-relativistic temperatures $z^{-1} \ll 1$. [*Plot made by Carlos Gabarrete.*]

[6] When the temperatures are non-relativistic ($mc^2 \gg k_B T$), the Maxwell-Jüttner distribution reduces to the Maxwell-Boltzmann distribution.

4.3 Summary of analytic models

In this section we provide a summary of the relativistic expressions that we have obtained for the steady, spherical accretion of a collisionless kinetic gas from finite radius onto a Schwarzschild BH for the different models presented in Sections 4.1 and 4.2. In all these models, the mass accretion rate can be written in the following general form:

$$|\dot{M}| = 4\pi R^2 \alpha(R) mcn_R \Gamma, \tag{4.92}$$

where R is the areal radius of the injection sphere, $\alpha(R) = \sqrt{1 - r_S/R}$, with $r_S = 2GM/c^2$ the Schwarzschild radius of the black hole, m is the mass of the particles and n_R is the particle density at the injection sphere. Here, Γ is a model-dependent dimensionless factor which is defined as follows.

1. **Purely radial mono-energetic model**:

$$\Gamma = \frac{v_R}{c} \frac{1}{\sqrt{1 - \frac{v_R^2}{c^2}}}, \tag{4.93}$$

   where v_R is the magnitude of the three-velocity measured by static observers at the injection sphere.

2. **Purely radial Maxwell-Jüttner-type model**:

$$\Gamma = \frac{1}{\sqrt{[\mathbf{K}_1(z) z e^z]^2 - 1}}, \tag{4.94}$$

   where $z = mc^2\alpha(R)/k_B T$ with T the gas temperature at the injection sphere and where $\mathbf{K}_1(z)$ is the modified Bessel function of the second kind of first order. In the low-temperature limit $z \gg 1$, this factor reduces to $\Gamma \approx \sqrt{2/(\pi z)}$.

3. **Mono-energetic model with angular momentum**:

$$\Gamma = \begin{cases} \sqrt{\dfrac{\gamma^2 - 1}{3\gamma^2 + 1}} & \text{for} \quad 1 < \gamma < \gamma_c(R), \qquad (4.95a) \\ \dfrac{h(R,\gamma)}{\left[4\gamma^2 \left(\sqrt{\gamma^2 - 1} + \sqrt{\gamma^2 - 1 - h(R,\gamma)}\right)^2 - h(R,\gamma)^2\right]^{1/2}} & \text{for} \quad \gamma > \gamma_c(R), \qquad (4.95b) \end{cases}$$

where $\gamma = (1 - v_R^2/c^2)^{-1/2}$ is the Lorentz factor, $\gamma_c(R) = E_c(R)/[mc^2\alpha(R)]$ with $E_c(R)$ given by Eq. (1.45), and

$$h(R,\gamma) = \frac{8r_S^2}{R^2}\frac{1}{36\,\alpha^2\gamma^2 - 8 - 27\alpha^4\gamma^4 + \alpha\gamma[9\alpha^2\gamma^2 - 8]^{3/2}}. \tag{4.96}$$

In the (non-relativistic) limit $R \gg r_S$ and $v_R \ll c$, these expressions simplify to

$$\Gamma \approx \begin{cases} \dfrac{v_R}{2c}, \quad \text{for} \quad \dfrac{v_R}{2c} < \dfrac{r_S}{R}, & \text{(4.97a)} \\ \dfrac{\frac{2c}{v_R}\left(\frac{r_S}{R}\right)^2}{1+\sqrt{1-\left(\frac{2c}{v_R}\frac{r_S}{R}\right)^2}}, \quad \text{for} \quad \dfrac{v_R}{2c} > \dfrac{r_S}{R}. & \text{(4.97b)} \end{cases}$$

4. **Maxwell-Jüttner-type model with angular momentum**:

$$\Gamma = \frac{1}{\sqrt{4z\left[\frac{I_1(R,z)}{I_2(R,z)}\right]^2 - 1}}, \tag{4.98}$$

where the integrals I_1 and I_2 are defined in Eqs. (4.79, 4.80). In the (non-relativistic) limit $R \gg r_S$ and $z \gg 1$, this expression simplifies to

$$\Gamma \approx \sqrt{\frac{2}{\pi z}}\tanh\left(\frac{r_S^2}{R^2}z\right). \tag{4.99}$$

Note that in the limit $z \gg R^2/r_S^2$ one obtains precisely the same result as the low-temperature limit of the purely radial Maxwell-Jüttner-type model, $\Gamma \approx \sqrt{2/(\pi z)}$. This shows that at very low temperatures the angular momentum is unimportant, which is expected since at low temperatures most of the particles have low energy and hence must have low angular momentum as well.[7]

4.4 Applications to Sgr A* and M87*

In this section we apply our models to the flows of Sgr A* and M87*, and we compare the results with those obtained from hydrodynamical considerations (see Section 2.4). We compute the accretion rate at scales of the order of the Bondi radius (in which the hydrodynamical treatment is expected to be a good approximation) and at the scales of the Schwarzschild

[7] See Eq. (1.41): $L_{\max}$ is small if E is close to its minimum value $\alpha(R)mc^2$.

radius (in which the kinetic analysis should become the best approximation). In our models we use the same temperature T for the cases described by a Maxwell-Boltzmann or Maxwell-Jüttner-type distribution, whereas in the mono-energetic cases we convert T to a velocity by choosing the velocity of the particles at the injection radius v_R such that

$$\frac{1}{2}m_{\rm p}v_R^2 = k_{\rm B}T, \tag{4.100}$$

in a first approximation.[8]

4.4.1 Accretion at Bondi radius scales

For Sgr A*, which has $T \sim 2.2\times10^7$ K (or $k_{\rm B}T \sim 1.9$ keV) at $R = r_{\rm B} \sim 0.06$ pc (see Section 2.4.1), we obtain $v_R = 600\,{\rm km\,s^{-1}}$, which lies within the velocity range of stellar winds (see footnote 8), suggesting that the approximation (4.100) is acceptable. In the case of M87*, we have $T \sim 1.06\times10^7$ K (or $k_{\rm B}T \sim 0.91$ keV) at $R \sim 0.19$ kpc (see also Section 2.4.1), which gives us $v_R = 420\,{\rm km\,s^{-1}}$. We also use these values of v_R to compute the mass accretion rate for the Zeldovich-Novikov model for mono-energetic particles (Eq. (4.73) in this work, or Eq. (14.2.20) in Shapiro and Teukolsky 1983) and we use the same temperature for the Rioseco-Sarbach model (Eq. (4.91) in this work, or Eq. (87) in Rioseco and Sarbach 2017a).[9] We show the comparisons in Tables 4.1 and 4.2. In all of these models, we have considered the observational approach and assumed that the values of n_R correspond to the measured electron number density $n_{\rm e}$ at R, as is regularly done when applying the Bondi model. Furthermore, we assume a fully ionized hydrogen gas, so $n_{\rm e} = n_{\rm p}$, and since $m_{\rm p} \gg m_{\rm e}$, then the mass accretion rate will be determined mainly by the protons, thus we take $m = m_{\rm p}$.

We see from Tables 4.1 and 4.2 that our models predict significantly different mass accretion rates depending on whether or not the infalling particles have angular momentum. The results from the purely radial infall in the kinetic description, both in the relativistic and non-relativistic cases, agree in order of magnitude with those of the hydrodynamical Bondi model. In contrast to this, the models with angular momentum predict a significantly lower mass accretion rate (by about $\sim$ 4–5 orders of magnitude) than the Bondi formula, and have

[8] Although v_R is not known a priori, it is reasonable to suppose that it is of the order of the fluid sound speed or to assume that its value is of the order of the wind velocity from known massive stars that are embedded within the dilute accretion flow. For example, the stellar winds surrounding Sgr A* have velocities of the order of $\sim$ 450–3000 km s^{-1} depending if the winds are composed by O-type stars (Allen et al. 1990; Puls et al. 1996; Repolust et al. 2004) or Wolf-Rayet stars (Martins et al. 2007; Paumard et al. 2006). Through numerical hydrodynamical simulations of wind-fed accretion, this range of velocities has been shown to be consistent with observational constraints from X-ray luminosities and Faraday rotation measures (Calderón et al. 2020; Cuadra and Nayakshin 2006; Cuadra et al. 2008; Ressler et al. 2018, 2020; see also Section 2.4).

[9] To apply the Zeldovich-Novikov and Rioseco-Sarbach models, we have assumed that $n_\infty = n_R$

Accretion model	Approximation	Distribution function	$\lvert\dot{M}\rvert\,[\mathrm{M}_\odot\,\mathrm{yr}^{-1}]$	Reference
Bondi	non-rel	(Perfect fluid)	$\sim 10^{-5}$	Falcke and Markoff (2013)
Zeldovich-Novikov	non-rel	Mono-energetic	$\sim 1.29\times 10^{-9}$	Zeldovich and Novikov (1971)
Rioseco-Sarbach	rel	Maxwell-Jüttner	$\sim 1.45\times 10^{-9}$	Rioseco and Sarbach (2017a)
Radial infall	non-rel	Mono-energetic	$\sim 1.09\times 10^{-4}$	This work, Eq. (4.15)
Radial infall	non-rel	Maxwell-Boltzmann	$\sim 6.22\times 10^{-5}$	This work, Eq. (4.21)
Radial infall	rel	Mono-energetic	$\sim 1.09\times 10^{-4}$	This work, Eq. (4.35)
Radial infall	rel	Maxwell-Jüttner	$\sim 6.22\times 10^{-5}$	This work, Eq. (4.46)
Infall with angular momentum	rel	Mono-energetic	$\sim 1.29\times 10^{-9}$	This work, Eq. (4.76b)
Infall with angular momentum	rel	Maxwell-Jüttner	$\sim 1.45\times 10^{-9}$	This work, Eq. (4.90)

Table 4.1 Mass accretion rate inferred for Sgr A* at $R = 0.06\,\mathrm{pc}$, for the models studied in this work and for other models from the literature. We assume $m = m_\mathrm{p} = 1.67\times 10^{-27}\,\mathrm{kg}$, and the characteristic values of $M = 4.3\times 10^6\ \mathrm{M}_\odot$, $T = 2.2\times 10^7\,\mathrm{K}$ and $n_R = 160\,\mathrm{cm}^{-3}$, as mentioned in the text. We consider an infall velocity of $v_R = 600\,\mathrm{km\,s}^{-1}$ at the radius R for the mono-energetic models. The Bondi model result is taken from Eq. (2.9). In the mono-energetic models we have used $E_0 = \frac{1}{2}m_\mathrm{p}v_R^2 - GMm_\mathrm{p}/R$ for the non-relativistic case and $E_0 = mc^2\alpha(R)\gamma$ for the relativistic case. Note that in the latter case with angular momentum it turns out that $\gamma > \gamma_\mathrm{c}(R)$, and since both conditions $R \gg r_\mathrm{S}$ and $v_\mathrm{R} \ll c$ are met, one can use the corresponding approximation (4.76b). 'Non-rel' and 'rel' stand for the kinetic non-relativistic and relativistic cases, respectively.

rates very similar to the ones from the Zeldovich-Novikov and Rioseco-Sarbach models, where the infall is assumed to start from infinity, clearly indicating that the angular momentum is a decisive parameter in determining the magnitude of the mass accretion rate.

To shed some light on these results, we first note that in the scenario considered in Table 4.1, the parameter $z = mc^2\alpha(R)/k_\mathrm{B}T \approx mc^2/k_\mathrm{B}T \approx 5\times 10^5$ is still smaller than the ratio $\left(\frac{R}{r_\mathrm{S}}\right)^2 \approx 2.1\times 10^{10}$, that is $z \ll \left(\frac{R}{r_\mathrm{S}}\right)^2$, and thus the results for the Maxwell-Jüttner model with or without angular momentum *differ significantly* [see the discussion below Eq. (4.99)].[10] On the other hand, for the scenario considered in Table 4.2, we have $z \approx 10^6$ and $\left(\frac{R}{r_\mathrm{S}}\right)^2 \approx 9.3\times 10^{10}$, so we still have $z \ll \left(\frac{R}{r_\mathrm{S}}\right)^2$, and the same analysis applies.

Furthermore, we observe that the models describing a purely radial infall can be written in the form [see Eqs. (4.92), (4.93) and (4.94)]

$$\frac{|\dot{M}|}{mn_R v_R} = 4\pi\lambda_{L=0}R^2, \tag{4.101}$$

with $\lambda_{L=0} \coloneqq \alpha(R)\,\Gamma\, c/v_\mathrm{R} = \mathscr{O}(1)$ for both Sgr A* and M87* cases.[11] This has the same form as the Bondi formula (2.6) with the Bondi radius r_B replaced with R and the sound speed

[10] The only way the role of the angular momentum could be neglected is to have $z \gg \left(\frac{R}{r_\mathrm{S}}\right)^2$. This means that only at very low temperatures (of the order of the Cosmic Microwave background, $T \sim 2.73\,\mathrm{K}$ or lower), the models with and without angular momentum yield comparable mass accretion rates for the ratio between R and r_S considered in our example.

[11] The fact that $\lambda_{L=0} = \mathscr{O}(1)$ can be seen directly from Eq. (4.93) for the radial case, but for the Maxwell-Jütner case we need to use that $v_R/c \approx \sqrt{2/z}$ which can be seen from Eq. (4.100) and the definition of z.

Accretion model	Approximation	Distribution function	$\lvert\dot{M}\rvert\,[\mathrm{M}_\odot\,\mathrm{yr}^{-1}]$	Reference
Bondi	non-rel	(Perfect fluid)	~ 0.3	This work, Eq. (2.10)
Zeldovich-Novikov	non-rel	Mono-energetic	$\sim 8.15\times10^{-6}$	Zeldovich and Novikov (1971)
Rioseco-Sarbach	rel	Maxwell-Jüttner	$\sim 9.24\times10^{-6}$	Rioseco and Sarbach (2017a)
Radial infall	non-rel	Mono-energetic	~ 1.49	This work, Eq. (4.15)
Radial infall	non-rel	Maxwell-Boltzmann	~ 0.84	This work, Eq. (4.21)
Radial infall	rel	Mono-energetic	~ 1.49	This work, Eq. (4.35)
Radial infall	rel	Maxwell-Jüttner	~ 0.84	This work, Eq. (4.46)
Infall with angular momentum	rel	Mono-energetic	$\sim 8.15\times10^{-6}$	This work, Eq. (4.76b)
Infall with angular momentum	rel	Maxwell-Jüttner	$\sim 9.24\times10^{-6}$	This work, Eq. (4.90)

Table 4.2 Mass accretion rate inferred for M87* at $R = 0.19\,\mathrm{kpc}$, for the models studied in this work and for other models from the literature. We assume $m = m_\mathrm{p} = 1.67\times10^{-27}\,\mathrm{kg}$, and the characteristic values of $M = 6.5\times10^9\ \mathrm{M}_\odot$, $T = 1.06\times10^7\,\mathrm{K}$ and $n_R = 0.31\,\mathrm{cm}^{-3}$, as mentioned in the text. We consider an infall velocity of $v_R = 420\,\mathrm{km\,s}^{-1}$ at the radius R for the mono-energetic models. In the mono-energetic models we have used $E_0 = \frac{1}{2}m_\mathrm{p}v_R^2 - GMm_\mathrm{p}/R$ for the non-relativistic case and $E_0 = mc^2\alpha(R)\gamma$ for the relativistic case. Note that in the latter case with angular momentum it turns out that $\gamma > \gamma_\mathrm{c}(R)$, and since both conditions $R \gg r_\mathrm{S}$ and $v_\mathrm{R} \ll c$ are met, one can use the corresponding approximation (4.76b). 'Non-rel' and 'rel' stand for the kinetic non-relativistic and relativistic cases, respectively.

c_∞ replaced with v_R. Since in our example $R \approx r_\mathrm{B}$ and v_R is comparable with c_∞, it follows that the accretion rates for the purely radial infall yield similar results to the Bondi model. In contrast, the models with angular momentum [Eqs. (4.97) and (4.99)] in the limit $z \ll (R/r_\mathrm{S})^2$ relevant for our example, give us

$$\frac{|\dot{M}|}{mn_Rv_R} = 4\pi\lambda_{L>0}\,r_\mathrm{S}^2 z = 4\pi\lambda_{L>0}\,r_\mathrm{B}^2\left(\frac{r_\mathrm{S}^2}{r_\mathrm{B}^2}z\right), \tag{4.102}$$

with $\lambda_{L>0} := R^2\alpha(R)\Gamma c/(v_R r_S^2 z) = \mathscr{O}(1)$ for both Sgr A* and M87* cases. Accordingly, the mass accretion rate is suppressed by a factor of $(r_\mathrm{S}/r_\mathrm{B})^2 z \sim 10^{-5}$ for both cases, compared to the Bondi accretion rate.

As mentioned in Section 2.3.2, a long standing problem in astrophysics is that the measured luminosity of Sgr A* (and other underluminous sources such as M87*) is way lower than that expected from the Eddington luminosity. Since the luminosity of the accreting flow of BHs is proportional to the mass accretion rate, there have been mainly two proposed solutions to explain the observed low luminosity: 1) a Bondi accretion rate with a very low radiative efficiency or 2) a much lower mass accretion rate than the Bondi rate. In the literature, various RIAF models have been proposed to solve this problem by taking into account one or both of these solutions (see Section 2.3). Comparing the results from Tables 4.1 and 4.2, we conclude that part of the solution to the low luminosity problem of Sgr A* and M87* could be that the mass accretion rate should be inferred from the accretion of a kinetic gas at a finite radius, taking into account the angular momentum of the individual particles. In this case, our mass accretion rate estimates for the models with angular momentum are of the order of the mass

accretion rates bounds inferred from rotation measures (see Section 2.4.2). Note, however, that these bounds are supposed to be for the vicinity of the BH horizon. Therefore, there is a significant difference in the results of the hydrodynamical and kinetic approaches for the wind accretion at $R \sim r_{\rm B}$, at least for our simplified models with angular momentum. A more complete theoretical kinetic treatment and future kinetic simulations of this accretion scenario could explain this difference, by confirming the important disparity between the accretion rates, or by endowing the kinetic flow with an accretion rate-reduction mechanism as a consequence of the more complex modelling of the problem. Finally, note that our explanation of the low luminosity problem relies solely in the assumption that the luminosity is proportional to the accretion rate. In contrast, the RIAF solutions rely in the mechanism of radiation of the accretion flow to explain the low luminosity (see Section 2.3). In our simplified models, we did not take into account the radiation properties of the collisionless kinetic gas.

4.4.2 Accretion at event horizon scales

At the scales of the Schwarzschild radius, the values of temperature and density of the flow near the BH are estimated from the results of GRMHD simulations for a two-temperature plasma of electrons and ions (see Section 2.3). The accretion in these simulations proceeds through a geometrically thick, optically thin hydrodynamical flow, coming initially from a weakly magnetized torus in hydrodynamic equilibrium, orbiting a Kerr BH. Despite the significant physical differences with the more realistic case studied in the GRMHD simulations, we apply our models of the Maxwell-Jüttner-type distribution function as an illustrative first approximation for the kinetic scenario.[12]

For Sgr A* we take the values of density and temperature at event horizon scales of a two-temperature radial inflow–outflow hydrodynamical model with self-consistent feeding and conduction presented in Shcherbakov and Baganoff (2010); we assume a fully ionized plasma so that there is an equality between electron and proton densities, $n_{\rm e} = n_{\rm p}$, and we take $R = 5\,r_{\rm S}$, $n_R = n_{\rm e} = 2 \times 10^6\,{\rm cm}^{-3}$ and $T = T_{\rm p} = 30\,T_{\rm e} = 1.2 \times 10^{12}\,{\rm K}$. We also take $m = m_{\rm p}$ since $m_{\rm p} \gg m_{\rm e}$. The accretion rates calculated are shown in Table 4.3. We found consistency with the values of the RM constraints for the vicinity of Sgr A* (see Section 2.4.2).[13] Moreover, the radial infall in our models produces a greater mass accretion rate by a factor of ~ 3.3. Thus, *in these models the role of angular momentum is not highly significant close to the BH horizon* (in contrast, at the Bondi radius scales, we found a difference of $\sim$ 4–5 orders of magnitude

[12] In this case, we do not consider the mono-energetic models due to their more idealized (non-physical) nature.

[13] Very recently, the Event Horizon Telescope collaboration estimated Sgr A*'s accretion rate to be around $\dot{M} \sim 10^{-9} - 10^{-8}\,{\rm M}_\odot\,{\rm yr}^{-1}$ with their GRMHD simulations (Event Horizon Telescope Collaboration 2022e). Our kinetic model with angular momentum predicts an accretion rate inside this range.

between the radial infall and the infall with angular momentum, as we discussed earlier). This is consistent with the well-known fact that particles fall almost radially as they approach to the ISCO (see e.g. Chandrasekhar 1983; Núñez and Degollado 2005). It is important to note that we took values of temperature and densities from hydrodynamical models as a first approximation, due to the lack of model-independent estimations of the conditions near the SMBHs.

Accretion model	Distribution function	$\lvert\dot{M}\rvert\,[\mathrm{M}_\odot\,\mathrm{yr}^{-1}]$	Reference
Radial infall	Maxwell-Jüttner	$\sim 2\times10^{-7}$	This work, Eq. (4.45)
Infall with angular momentum	Maxwell-Jüttner	$\sim 6.04\times10^{-8}$	This work, Eq. (4.81)

Table 4.3 Mass accretion rate inferred for Sgr A* at $R = 5\,r_\mathrm{S}$, for the Maxwell-Jüttner models. We have used $m = m_\mathrm{p} = 1.67\times10^{-27}\,\mathrm{kg}$, $M = 4.3\times10^{6}\,\mathrm{M}_\odot$, $T = 1.2\times10^{12}\,\mathrm{K}$ and $n_R = 2\times10^{6}\,\mathrm{cm}^{-3}$ (see Shcherbakov and Baganoff 2010).

With the same caveats as in the Sgr A* case, we apply our Maxwell-Jüttner-type models to M87*. Recently, the EHT collaboration has provided results for the mass accretion rate due to the plasma around M87*. They report an estimated average number density range of $n_\mathrm{e}\sim 2.9\times10^{4\text{–}7}\,\mathrm{cm}^{-3}$, an electron temperature $T_\mathrm{e}\sim$ (1–12) $\times10^{10}\,\mathrm{K}$, and an inferred mass accretion rate for M87* of $(3-20)\times10^{-4}\,\mathrm{M}_\odot\,\mathrm{yr}^{-1}$ from a simple one-zone emission model (Event Horizon Telescope Collaboration 2019e, 2021a,b). For the specific isothermal sphere model, they estimate the plasma number density $n_\mathrm{e}\simeq 2.9\times10^{4}\,\mathrm{cm}^{-3}$ and the electron temperature $T_\mathrm{e}\simeq 6.25\times10^{10}\,\mathrm{K}$, at an emission radius $r\simeq 5r_\mathrm{S}/2$. In Table 4.4 we present the mass accretion rates obtained from these values, assuming a fully ionized hydrogen plasma ($n_\mathrm{ions}=n_\mathrm{e}$) and assuming thermal equilibrium between the ions and electrons ($T_\mathrm{ions}=T_\mathrm{e}$) as a first approximation. Furthermore, we impose these values at radius $R\sim 5r_\mathrm{S}$, as in the example of Sgr A*.[14] In this case, we also got similar mass accretion rates for the models with and without angular momentum. Therefore, we confirm again that the *angular momentum does not play an important role at event horizon scales*. Despite our crude approximation for the accretion flow of M87*, the inferred mass accretion rates are consistent with the reported bounds by the Event Horizon Telescope Collaboration (2021b) (see Section 2.4.2).

[14]The reason for not choosing $R = 5r_\mathrm{S}/2$ is that this value is smaller than the ISCO radius of a Schwarzschild BH assumed in our model.

Accretion model	Distribution function	$\lvert\dot{M}\rvert\,[\mathrm{M}_\odot\,\mathrm{yr}^{-1}]$	Reference
Radial infall	Maxwell-Jüttner	$\sim 1.53\times10^{-3}$	This work, Eq. (4.45)
Infall with angular momentum	Maxwell-Jüttner	$\sim 1.52\times10^{-3}$	This work, Eq. (4.81)

Table 4.4 Mass accretion rate inferred for M87* at $R = 5\,r_\mathrm{S}$, for the Maxwell-Jüttner models. We have used $m = m_\mathrm{p} = 1.67\times10^{-27}\,\mathrm{kg}$, $M = 6.5\times10^{9}\,\mathrm{M}_\odot$, $T = 6.25\times10^{10}\,\mathrm{K}$ and $n_R = 2.9\times10^{4}\,\mathrm{cm}^{-3}$ (see Event Horizon Telescope Collaboration 2019f, 2021b).

Conclusions

Low collisionality is a general property expected in underluminous flows near black holes (BHs) due to the conditions of high temperatures and low densities; it is also an expected property of dark matter. Remarkably, this kind of flows could be immersed in a strong gravitational background and/or in a high-velocity/high-temperature state. Therefore, we expect that the appropriate treatment of these scenarios should be done with general relativistic Kinetic Theory. Previous analytic studies treat the problem of kinetic relativistic accretion onto BHs by specifying boundary conditions at infinity, whereas in a realistic situation the gas is accreted from a region of finite radius.

In this work we presented several analytic models and their corresponding steady-state solutions for the accretion of a spherically symmetric, collisionless kinetic gas cloud onto a Schwarzschild BH. The novelty of this work consists in specifying the properties of the kinetic gas (its particle density n_R and mean velocity or temperature) at an *injection sphere* of *finite radius* R. The models we have discussed (both in non-relativistic and relativistic regimes) include the simple case of purely radial infall (in which all the particles have zero angular momentum) and the case of a kinetic gas with a uniform distribution in the angular momentum, such that individual gas particles may rotate about the BH, but maintaining the spherical symmetry of the gas configuration as a whole. We considered two particular models: 1) a mono-energetic distribution in energy in which all particles have the same energy (or the same three-velocity v_R at the injection sphere), and 2) a Maxwell-Jüttner distribution (a generalization of the Maxwell-Boltzmann distribution) with corresponding temperature T, assuming that the gas is accreted from a reservoir of particles in thermodynamic equilibrium. In each model, the mass accretion rate depends linearly on n_R which is a direct consequence of our test field approximation (we have neglected the self-gravity of the kinetic gas) while its dependency on R and v_R or T is more intricate and is summarized in Section 4.3. We have checked that for fixed values of n_R, v_R and T, the accretion rates of our models converge to the corresponding expressions of previously known results in the limit $R \to \infty$.

We used our models to calculate the mass accretion rate onto the SMBHs Sgr A* and M87*, estimating the conditions of the gas at Bondi radius and event horizon scales. Our results, which are summarized in Tables 4.1–4.4, are of the order of the model-dependent bounds for the mass accretion rate of Sgr A* and the bounds estimated for M87* by the Event Horizon Telescope collaboration. Overall, our kinetic models can predict lower mass accretion rates than the Bondi fluid model (see the following paragraphs). This suggests that a complete kinetic treatment to the accretion problem could explain some of the current questions associated with underluminous sources such as Sgr A* or M87*.

We have shown that, for boundary conditions corresponding to non-relativistic velocities or temperatures, the mass accretion rates predicted by the purely radial infall models and by the well-known Bondi model for a hydrodynamic flow, yield comparable results, provided R is of the same order as the Bondi radius. This has physical sense since the presence of collisions between particles in the Bondi hydrodynamical model restricts tangential motion and funnels particles effectively in the radial direction. Therefore, in this work we obtained the kinetic relativistic analogue of the Bondi model.

Regarding our models with angular momentum, we have found that the kinetic accretion rate differs significantly (is much lesser) from the Bondi estimation (this was previously known for models with $R \to \infty$). This is a consequence of having a collisionless gas, since the collisions in the hydrodynamic model channel the particles into the BH, as we mentioned before. Moreover, we have showed that the predictions of kinetic models with $R \sim R_{\mathrm{B}}$ are very similar to those with $R \to \infty$.

When the injection sphere is close to the event horizon, $R \sim r_{\mathrm{S}}$, we have found that the kinetic accretion rates predicted by the models with and without angular momentum yield very similar results. This is consistent with the fact that the particles fall almost radially as they approach to the radius of the innermost stable circular orbit.

Furthermore, we showed that the accretion rate of the models with angular momentum behaves qualitatively similarly to the purely radial infall models (it increases with increasing values of v_R or T) as long as v_R or T lie below a critical value. However, above this critical value, the accretion rate reverses its behavior and decreases with increasing v_R or T until it reaches a finite value. As we have explained, this reversal is due to the fact that as the particle's energy increases above a certain threshold, not all the particles are absorbed by the BH, and the fraction of absorbed particles becomes smaller as the energy increases, leading to a diminishing mass accretion rate.

There are several ingredients which, for simplicity, we did not take into account in our models. In particular, we restricted ourselves to spherical, steady accretion onto a Schwarzschild BH, instead of the more realistic non-spherical (possibly disk-like) and unsteady accretion

onto a Kerr BH. Furthermore, we did not included the effects of radiative processes, magnetic fields, the consequences of outflows, convection currents or jets.

Despite its simplicity, the presented models could serve as reference for more generic kinetic models, and they could be useful as a starting point to describe other physical scenarios where the assumptions of very low collisionality or quasi-spherical symmetry are approximately satisfied. This is the case, for example, in the BH accretion of dark matter, which is expected to be very weakly interactive, or in the accretion of low-luminosity active galactic nuclei whose corresponding flows are in a hot and low-density state. Future generalizations of the presented formalism could be a key step in understanding the accretion process.

References

Abramowicz, M. A., Czerny, B., Lasota, J. P., and Szuszkiewicz, E. (1988). Slim Accretion Disks. *Astrophysical Journal*, 332:646.

Abramowitz, M. and Stegun, I. A. (1964). *Handbook of Mathematical Functions with Formulas, Graphs, and Mathematical Tables*. Dover, New York, ninth dover printing, tenth gpo printing edition.

Acuña Cárdenas, R. O., Gabarrete, C., and Sarbach, O. (2022). An introduction to the relativistic kinetic theory on curved spacetimes. *Gen. Rel. Grav.*, 54(3):23.

Adamo, T. and Newman, E. T. (2014). The Kerr-Newman metric: A Review. *Scholarpedia*, 9:31791.

Agol, E. (2000). Sagittarius a* polarization: No advection-dominated accretion flow, low accretion rate, and nonthermal synchrotron emission. *The Astrophysical Journal*, 538(2):L121–L124.

Aguayo-Ortiz, A., Tejeda, E., Sarbach, O., and López-Cámara, D. (2021). Spherical accretion: Bondi, Michel, and rotating black holes. MNRAS.

Aitken, D. K. et al. (2000). Detection of Polarized Millimeter and Submillimeter Emission from Sagittarius A*. *Astrophysical Journal Letters*, 534(2):L173–L176.

Allen, D. A., Hyland, A. R., and Hillier, D. J. (1990). The source of luminosity at the Galactic Centre. MNRAS, 244:706.

Andersson, L., Blue, P., and Joudioux, J. (2018). Hidden symmetries and decay for the vlasov equation on the kerr spacetime. *Communications in Partial Differential Equations*, 43(1):47–65.

Andersson, L. and Fajman, D. (2020). Nonlinear Stability of the Milne Model with Matter. *Commun. Math. Phys.*, 378:261–298.

Andreasson, H. (2011). The Einstein-Vlasov System/Kinetic Theory. *Living Rev. Rel.*, 14:4.

Andreasson, H. (2012). Black hole formation from a complete regular past for collisionless matter. *Annales Henri Poincare*, 13:1511–1536.

Andréasson, H. (2014). On gravitational collapse and cosmic censorship for collisionless matter. *Int. J. Geom. Meth. Mod. Phys.*, 11:1460002.

Andréasson, H., Fajman, D., and Thaller, M. (2014). Static solutions to the Einstein-Vlasov system with non-vanishing cosmological constant. *SIAM J. Math. Anal.*, 47(4):2657–2688.

Andreasson, H., Kunze, M., and Rein, G. (2011). Existence of axially symmetric static solutions of the Einstein-Vlasov system. *Commun. Math. Phys.*, 308:23–47.

Andreasson, H., Kunze, M., and Rein, G. (2014). Rotating, stationary, axially symmetric spacetimes with collisionless matter. *Commun. Math. Phys.*, 329:787–808.

Andreasson, H. and Rein, G. (2007). On the steady states of the spherically symmetric Einstein-Vlasov system. *Class. Quant. Grav.*, 24:1809–1832.

Andréasson, H. and Ringström, H. (2013). Proof of the cosmic no-hair conjecture in the T^3-Gowdy symmetric Einstein-Vlasov setting. *Journal of the European Mathematical Society*.

Argüelles, C. R., Díaz, M. I., Krut, A., and Yunis, R. (2021). On the formation and stability of fermionic dark matter haloes in a cosmological framework. MNRAS, 502(3):4227–4246.

Ashtekar, A. et al. (2015). *General Relativity and Gravitation: A Centennial Perspective*. Cambridge University Press.

Baganoff, F. K. et al. (2003). Chandra X-Ray Spectroscopic Imaging of Sagittarius A* and the Central Parsec of the Galaxy. ApJ, 591(2):891–915.

Bancel, D. and Choquet-Bruhat, Y. (1973). Existence, uniqueness, and local stability for the einstein-maxwell-boltzman system. *Comm. Math. Phys.*, 33:83–96.

Barzegar, H. and Fajman, D. (2020). Stable cosmologies with collisionless charged matter.

Belmont, G., Grappin, R., Mottez, F., Pantellini, F., and Pelletier, G. (2013). *Collisionless Plasmas in Astrophysics*. Wiley.

Berti, E. et al. (2015). Testing General Relativity with Present and Future Astrophysical Observations. *Class. Quant. Grav.*, 32:243001.

Bigorgne, L. (2020). Decay estimates for the massless vlasov equation on schwarzschild spacetimes.

Bigorgne, L. et al. (2021). Asymptotic stability of Minkowski space-time with non-compactly supported massless Vlasov matter. *Arch. Rational Mech. Anal.*, 242:1–147.

Binney, J. and Tremaine, S. (2008). *Galactic Dynamics*. Princeton University Press, Princeton, NJ, USA, 2nd ed. edition.

Birkhoff, G. (1923). *Relativity and Modern Physics*. Harvard University Press, Cambridge, Mass., U.S.A.

Blandford, R. D. and Begelman, M. C. (1999). On the fate of gas accreting at a low rate onto a black hole. *Mon. Not. Roy. Astron. Soc.*, 303:L1.

Blandford, R. D. and Payne, D. G. (1982). Hydromagnetic flows from accretion disks and the production of radio jets. *Monthly Notices of the Royal Astronomical Society*, 199:883–903.

Blandford, R. D. and Znajek, R. L. (1977). Electromagnetic extraction of energy from Kerr black holes. *Monthly Notices of the Royal Astronomical Society*, 179:433–456.

Bondi, H. (1952). On spherically symmetrical accretion. *Monthly Notices of the Royal Astronomical Society*, 112:195.

Bondi, H. and Hoyle, F. (1944). On the Mechanism of Accretion by Stars. *Monthly Notices of the Royal Astronomical Society*, 104(5):273–282.

Bower, G. C. et al. (2018). ALMA Polarimetry of Sgr A*: Probing the Accretion Flow from the Event Horizon to the Bondi Radius. *Astrophysical Journal*, 868(2):101.

Bower, G. C., Wright, M. C. H., Falcke, H., and Backer, D. C. (2003). Interferometric Detection of Linear Polarization from Sagittarius A* at 230 GHz. *Astrophysical Journal*, 588(1):331–337.

Calderón, D., Cuadra, J., Schartmann, M., Burkert, A., and Russell, C. M. P. (2020). Stellar Winds Pump the Heart of the Milky Way. ApJ, 888(1):L2.

Carroll, S. M. (2004). *Spacetime and geometry: An introduction to general relativity*. Addison Wesley, San Francisco.

Cercignani, C. and Kremer, G. (2002). *The Relativistic Boltzmann Equation: Theory and Applications*. Birkhäuser, Basel.

Chandra, M., Gammie, C. F., Foucart, F., and Quataert, E. (2015). An Extended Magnetohydrodynamics Model for Relativistic Weakly Collisional Plasmas. *Astrophys. J.*, 810(2):162.

Chandrasekhar, S. (1931). The maximum mass of ideal white dwarfs. *Astrophys. J.*, 74:81–82.

Chandrasekhar, S. (1957). *An Introduction to the Study of Stellar Structure*. Astrophysical monographs. Dover Publications.

Chandrasekhar, S. (1983). *The Mathematical Theory of Black Holes*. Oxford University Press, Oxford, England.

Chaverra, E. and Sarbach, O. (2015). Radial accretion flows on static spherically symmetric black holes. *Class. Quant. Grav.*, 32(15):155006.

Choquet-Bruhat, Y. (1971). Problème de Cauchy pour le système intégro-différentiel d'Einstein-Liouville. *Annales de l'Institut Fourier*, 21(3):181–201.

Choquette, J., Cline, J. M., and Cornell, J. M. (2019). Early formation of supermassive black holes via dark matter self-interactions. J. Cosmology Astropart. Phys., 2019(7):036.

Cieślik, A. and Mach, P. (2020). Accretion of the Vlasov gas on Reissner-Nordström black holes. *Phys. Rev. D*, 102(2):024032.

Coogan, A. et al. (2022). Measuring the dark matter environments of black hole binaries with gravitational waves. *Phys. Rev. D*, 105(4):043009.

Crawford, P. and Tereno, I. (2002). Generalized Observers and Velocity Measurements in General Relativity. *General Relativity and Gravitation*, 34(12):2075–2088.

Cuadra, J. and Nayakshin, S. (2006). Variable accretion of stellar winds onto Sgr A*. In *Journal of Physics Conference Series*, volume 54 of *Journal of Physics Conference Series*, pages 436–442.

Cuadra, J., Nayakshin, S., and Martins, F. (2008). Variable accretion and emission from the stellar winds in the Galactic Centre. MNRAS, 383(2):458–466.

Cuadra, J., Nayakshin, S., and Wang, Q. D. (2015). The role of feedback in accretion on low-luminosity AGN: Sgr A* case study. *Monthly Notices of the Royal Astronomical Society*, 450(1):277–287.

D'Angelo, C. R., Fridriksson, J. K., Messenger, C., and Patruno, A. (2015). The Radiative Efficiency of a Radiatively Inefficient Accretion Flow. *Mon. Not. Roy. Astron. Soc.*, 449(3):2803–2817.

De Groot, S. R., Van Leeuwen, W. A., and Van Weert, C. G. (1980). *Relativistic Kinetic Theory. Principles and Applications*. Amsterdam: North-Holland Pub. Co.

Debbasch, F., Rivet, J., and van Leeuwen, W. (2001). Invariance of the relativistic one-particle distribution function. *Physica A: Statistical Mechanics and its Applications*, 301(1):181–195.

Debbasch, F. and van Leeuwen, W. (2009a). General relativistic boltzmann equation, i: Covariant treatment. *Physica A: Statistical Mechanics and its Applications*, 388(7):1079–1104.

Debbasch, F. and van Leeuwen, W. (2009b). General relativistic boltzmann equation, ii: Manifestly covariant treatment. *Physica A: Statistical Mechanics and its Applications*, 388(9):1818–1834.

Di Matteo, T., Khandai, N., DeGraf, C., Feng, Y., Croft, R. A. C., Lopez, J., and Springel, V. (2012). Cold Flows and the First Quasars. ApJ, 745(2):L29.

D'Inverno, R. (1992). *Introducing Einstein's Relativity*. Clarendon Press.

Dodelson, S. and Schmidt, F. (2020). *Modern Cosmology*. Elsevier Science.

Eatough, R. P. et al. (2013). A strong magnetic field around the supermassive black hole at the centre of the Galaxy. Nature, 501(7467):391–394.

Eckart, C. (1940). The thermodynamics of irreversible processes. iii. relativistic theory of the simple fluid. *Phys. Rev.*, 58:919–924.

Edgar, R. (2004). A review of bondi–hoyle–lyttleton accretion. *New Astronomy Reviews*, 48(10):843–859.

Event Horizon Telescope Collaboration (2019a). First M87 Event Horizon Telescope Results. I. The Shadow of the Supermassive Black Hole. *Astrophys. J. Lett.*, 875:L1.

Event Horizon Telescope Collaboration (2019b). First M87 Event Horizon Telescope Results. II. Array and Instrumentation. *Astrophys. J. Lett.*, 875(1):L2.

Event Horizon Telescope Collaboration (2019c). First M87 Event Horizon Telescope Results. III. Data Processing and Calibration. *Astrophys. J. Lett.*, 875(1):L3.

Event Horizon Telescope Collaboration (2019d). First M87 Event Horizon Telescope Results. IV. Imaging the Central Supermassive Black Hole. *Astrophys. J. Lett.*, 875(1):L4.

Event Horizon Telescope Collaboration (2019e). First M87 Event Horizon Telescope Results. V. Physical Origin of the Asymmetric Ring. ApJ, 875(1):L5.

Event Horizon Telescope Collaboration (2019f). First M87 Event Horizon Telescope Results. VI. The Shadow and Mass of the Central Black Hole. ApJ, 875(1):L6.

Event Horizon Telescope Collaboration (2021a). First M87 Event Horizon Telescope Results. VII. Polarization of the Ring. ApJ, 910(1):L12.

Event Horizon Telescope Collaboration (2021b). First M87 Event Horizon Telescope Results. VIII. Magnetic Field Structure near The Event Horizon. ApJ, 910(1):L13.

Event Horizon Telescope Collaboration (2022a). First Sagittarius A* Event Horizon Telescope Results. I. The Shadow of the Supermassive Black Hole in the Center of the Milky Way. *Astrophys. J. Lett.*, 930(2):L12.

Event Horizon Telescope Collaboration (2022b). First Sagittarius A* Event Horizon Telescope Results. II. EHT and Multiwavelength Observations, Data Processing, and Calibration. *Astrophys. J. Lett.*, 930(2):L13.

Event Horizon Telescope Collaboration (2022c). First Sagittarius A* Event Horizon Telescope Results. III. Imaging of the Galactic Center Supermassive Black Hole. *Astrophys. J. Lett.*, 930(2):L14.

Event Horizon Telescope Collaboration (2022d). First Sagittarius A* Event Horizon Telescope Results. IV. Variability, Morphology, and Black Hole Mass. *Astrophys. J. Lett.*, 930(2):L15.

Event Horizon Telescope Collaboration (2022e). First Sagittarius A* Event Horizon Telescope Results. V. Testing Astrophysical Models of the Galactic Center Black Hole. *Astrophys. J. Lett.*, 930(2):L16.

Event Horizon Telescope Collaboration (2022f). First Sagittarius A* Event Horizon Telescope Results. VI. Testing the Black Hole Metric. *Astrophys. J. Lett.*, 930(2):L17.

Fajman, D. (2016). Future asymptotic behavior of three-dimensional spacetimes with massive particles. *Class. Quant. Grav.*, 33(11):11LT01.

Falcke, H. and Markoff, S. B. (2013). Toward the event horizon—the supermassive black hole in the galactic center. *Classical and Quantum Gravity*, 30(24):244003.

Feng, W.-X., Parisi, A., Chen, C.-S., and Lin, F.-L. (2021). Self-interacting dark scalar spikes around black holes via relativistic bondi accretion.

Foucart, F. et al. (2017). How important is non-ideal physics in simulations of sub-Eddington accretion on to spinning black holes? *Mon. Not. Roy. Astron. Soc.*, 470(2):2240–2252.

Frank, J., King, A., and Raine, D. J. (2002). *Accretion Power in Astrophysics*. Cambridge University Press, Cambridge, UK, 3rd ed. edition.

Gabarrete, C. and Sarbach, O. (2022). Kinetic Gas Disks Surrounding Schwarzschild Black Holes. *Acta Phys. Polon. Supp.*, 15(1):1.

Gamboa, A., Gabarrete, C., Domínguez-Fernández, P., Núñez, D., and Sarbach, O. (2021). Accretion of a Vlasov gas onto a black hole from a sphere of finite radius and the role of angular momentum. *Phys. Rev. D*, 104(8):083001.

Gardner, F. F. and Whiteoak, J. B. (1966). The polarization of cosmic radio waves. *Annual Review of Astronomy and Astrophysics*, 4(1):245–292.

Gebhardt, K. et al. (2011). The black hole mass in M87 from GEMINI/NIFS adaptive optics observations. *The Astrophysical Journal*, 729(2):119.

Ghez, A. M. et al. (2003). The First Measurement of Spectral Lines in a Short-Period Star Bound to the Galaxy's Central Black Hole: A Paradox of Youth. ApJ, 586(2):L127–L131.

Giacconi, R., Gursky, H., Paolini, F. R., and Rossi, B. B. (1962). Evidence for x rays from sources outside the solar system. *Phys. Rev. Lett.*, 9:439–443.

Gillessen, S. et al. (2009). Monitoring Stellar Orbits Around the Massive Black Hole in the Galactic Center. ApJ, 692(2):1075–1109.

Goddi, C. et al. (2017). Blackholecam: Fundamental physics of the galactic center. *International Journal of Modern Physics D*, 26(02):1730001.

Griffiths, D. (2013). *Introduction to Electrodynamics*. Always learning. Pearson.

Harris, W. E., Harris, G. L. H., and McLaughlin, D. E. (1998). M87, Globular Clusters, and Galactic Winds: Issues in Giant Galaxy Formation. AJ, 115(5):1801–1822.

Harrison, B. K., Thorne, K. S., Wakano, M., and Wheeler, J. A. (1965). *Gravitation Theory and Gravitational Collapse*. University of Chicago Press.

Hartle, J. B. (2003). *An introduction to Einstein's general relativity*. Addison-Wesley.

Hewish, A., Bell, S. J., Pilkington, J. D. H., Scott, P. F., and Collins, R. A. (1968). Observation of a rapidly pulsating radio source. *Nature*, 217:709–713.

Hoyle, F. and Lyttleton, R. A. (1939). The effect of interstellar matter on climatic variation. *Mathematical Proceedings of the Cambridge Philosophical Society*, 35(3):405–415.

Jackson, J. D. (1998). *Classical Electrodynamics*. Wiley.

Jeffery, G. B. and Filon, L. N. G. (1921). The field of an electron on Einstein's theory of gravitation. *Proceedings of the Royal Society of London. Series A, Containing Papers of a Mathematical and Physical Character*, 99(697):123–134.

Jiménez-Rosales, A. and Dexter, J. (2018). The impact of Faraday effects on polarized black hole images of Sagittarius A*. MNRAS, 478(2):1875–1883.

Johnson, M. D. et al. (2015). Resolved magnetic-field structure and variability near the event horizon of sagittarius a*. *Science*, 350(6265):1242–1245.

Jones, T. W. and O'Dell, S. L. (1977). Transfer of polarized radiation in self-absorbed synchrotron sources. I. Results for a homogeneous source. *Astrophysical Journal*, 214:522–539.

Joudioux, J., Thaller, M., and Kroon, J. A. V. (2021). The conformal Einstein field equations with massless Vlasov matter. *Annales Inst. Fourier*, 71(2):799–842.

Jüttner, F. (1911a). Das maxwellsche gesetz der geschwindigkeitsverteilung in der relativtheorie. *Annalen der Physik*, 339(5):856–882.

Jüttner, F. (1911b). Die dynamik eines bewegten gases in der relativtheorie. *Annalen der Physik*, 340(6):145–161.

Kavanagh, B. J. et al. (2020). Detecting dark matter around black holes with gravitational waves: Effects of dark-matter dynamics on the gravitational waveform. *Phys. Rev. D*, 102(8):083006.

Kerr, R. P. (1963). Gravitational field of a spinning mass as an example of algebraically special metrics. *Phys. Rev. Lett.*, 11:237–238.

Korol, V., Ciotti, L., and Pellegrini, S. (2016). Bondi accretion in early-type galaxies. *Monthly Notices of the Royal Astronomical Society*, 460(2):1188–1200.

Kruskal, M. D. (1960). Maximal extension of Schwarzschild metric. *Phys. Rev.*, pages 1743–1745.

Kunz, M. W., Stone, J. M., and Quataert, E. (2016). Magnetorotational turbulence and dynamo in a collisionless plasma. *Physical Review Letters*, 117(23).

Kuo, C. Y. et al. (2014). Measuring Mass Accretion Rate onto the Supermassive Black Hole in M87 Using Faraday Rotation Measure with the Submillimeter Array. ApJ, 783(2):L33.

Lee, H. (2013). Asymptotic behaviour of the relativistic Boltzmann equation in the Robertson-Walker spacetime. *J. Diff. Eq.*, 255(11):4267–4288.

Lee, H. and Nungesser, E. (2017). Bianchi I solutions of the Einstein-Boltzmann system with a positive cosmological constant. *J. Math. Phys.*, 58(9):092501.

Lee, H. and Nungesser, E. (2018). Late-time behaviour of the Einstein–Boltzmann system with a positive cosmological constant. *Class. Quant. Grav.*, 35(2):025001.

Lee, H., Nungesser, E., and Tod, P. (2020). The massless Einstein–Boltzmann system with a conformal gauge singularity in an FLRW background. *Class. Quant. Grav.*, 37(3):035005.

Lee, H. and Rendall, A. D. (2013). The einstein-boltzmann system and positivity. *Journal of Hyperbolic Differential Equations*, 10(01):77–104.

Li, G.-L., Tang, Y., and Wu, Y.-L. (2021). Probing dark matter spikes via gravitational waves of extreme mass ratio inspirals.

Lindblad, H. and Taylor, M. (2020). Global Stability of Minkowski Space for the Einstein–Vlasov System in the Harmonic Gauge. *Arch. Ration. Mech. Anal.*, 235:517–633.

Ma, C.-P. and Bertschinger, E. (2004). A Cosmological kinetic theory for the evolution of cold dark matter halos with substructure: Quasilinear theory. *Astrophys. J.*, 612:28–49.

Macchetto, F. et al. (1997). The supermassive black hole of m87 and the kinematics of its associated gaseous disk. *The Astrophysical Journal*, 489(2):579–600.

Mach, P. and Odrzywołek, A. (2021a). Accretion of dark matter onto a moving schwarzschild black hole: An exact solution. *Phys. Rev. Lett.*, 126:101104.

Mach, P. and Odrzywołek, A. (2021b). Accretion of the relativistic Vlasov gas onto a moving Schwarzschild black hole: Exact solutions. *Phys. Rev. D*, 103(2):024044.

Mach, P. and Odrzywołek, A. (2022). Accretion of the relativistic Vlasov gas onto a moving Schwarzschild black hole: Low-temperature limit and numerical aspects. *Acta Phys. Polon. Supp.*, 15:1–A7.

Macquart, J.-P. et al. (2006). The rotation measure and 3.5 millimeter polarization of sagittarius a*. *The Astrophysical Journal*, 646(2):L111–L114.

Mahadevan, R. (1999). Probing the two-temperature paradigm: observational tests for the basic assumptions in advection-dominated accretion flows. *Monthly Notices of the Royal Astronomical Society*, 304(3):501–511.

Mahadevan, R. and Quataert, E. (1997). Are particles in advection-dominated accretion flows thermal? *The Astrophysical Journal*, 490(2):605–618.

Maoz, D. (2016). *Astrophysics in a Nutshell: Second Edition*. In a Nutshell. Princeton University Press.

Marrone, D. P., Moran, J. M., Zhao, J.-H., and Rao, R. (2006). Interferometric Measurements of Variable 340 GHz Linear Polarization in Sagittarius A*. *Astrophysical Journal*, 640(1):308–318.

Marrone, D. P., Moran, J. M., Zhao, J.-H., and Rao, R. (2007). An Unambiguous Detection of Faraday Rotation in Sagittarius A*. *Astrophysical Journal Letters*, 654(1):L57–L60.

Martins, F. et al. (2007). Stellar and wind properties of massive stars in the central parsec of the Galaxy. A&A, 468(1):233–254.

Matteo, T. D., Allen, S. W., Fabian, A. C., Wilson, A. S., and Young, A. J. (2003). Accretion onto the supermassive black hole in m87. *The Astrophysical Journal*, 582(1):133–140.

Michel, F. C. (1972). Accretion of Matter by Condensed Objects. *Astrophysics and Space Science*, 15(1):153–160.

Mucha, P. B. (1998). The Cauchy Problem for the Einstein–Boltzmann System. *Journal of Applied Analysis*, 4(1):129–141.

Nakahara, M. (2003). *Geometry, topology and physics*. Taylor & Francis.

Narayan, R., Mahadevan, R., and Quataert, E. (1998). Advection-dominated accretion around black holes. In Abramowicz, M. A., Björnsson, G., and Pringle, J. E., editors, *Theory of Black Hole Accretion Disks*, pages 148–182.

Narayan, R. and Yi, I. (1994). Advection-dominated Accretion: A Self-similar Solution. *Astrophysical Journal Letters*, 428:L13.

Newman, E. T. et al. (1965). Metric of a Rotating, Charged Mass. *J. Math. Phys.*, 6:918–919.

Nordström, G. (1918). On the energy of the gravitational field in Einstein's theory. *Proc. Kon. Ned. Akad. Wet.*, 20:1238–1245.

Núñez, D. and Degollado, J. C. (2005). *Relatividad General*. online, Facultad de Ciencias, UNAM, Mexico City, Mexico.

Oda, M. (1977). CygX-1/A candidate of the black hole. Space Sci. Rev., 20(6):757–813.

Oppenheimer, J. R. and Snyder, H. (1939). On Continued gravitational contraction. *Phys. Rev.*, 56:455–459.

Park, J. et al. (2019). Faraday rotation in the jet of M87 inside the Bondi radius: indication of winds from hot accretion flows confining the relativistic jet. *Astrophys. J.*, 871(2):257.

Pathria, R. and Beale, P. (2021). *Statistical Mechanics*. Elsevier Science.

Paumard, T. et al. (2006). The Two Young Star Disks in the Central Parsec of the Galaxy: Properties, Dynamics, and Formation. ApJ, 643(2):1011–1035.

Penrose, R. (1969). Gravitational collapse: The role of general relativity. *Riv. Nuovo Cim.*, 1:252–276.

Porth, O., Olivares, H., Mizuno, Y., Younsi, Z., Rezzolla, L., Moscibrodzka, M., Falcke, H., and Kramer, M. (2017). The black hole accretion code. *Computational Astrophysics and Cosmology*, 4(1).

Prieto, M. A., Fernández-Ontiveros, J. A., Markoff, S., Espada, D., and González-Martín, O. (2016). The central parsecs of M87: jet emission and an elusive accretion disc. *Monthly Notices of the Royal Astronomical Society*, 457(4):3801–3816.

Pringle, J. E. and Rees, M. J. (1972). Accretion Disc Models for Compact X-Ray Sources. *Astronomy and Astrophysics*, 21:1.

Puls, J. et al. (1996). O-star mass-loss and wind momentum rates in the Galaxy and the Magellanic Clouds Observations and theoretical predictions. A&A, 305:171.

Quataert, E. and Gruzinov, A. (2000a). Constraining the Accretion Rate onto Sagittarius A* Using Linear Polarization. *The Astrophysical Journal*, 545(2):842–846.

Quataert, E. and Gruzinov, A. (2000b). Convection-dominated Accretion Flows. *The Astrophysical Journal*, 539(2):809–814.

Quataert, E. and Narayan, R. (1999). On the Energetics of Advection-dominated Accretion Flows. ApJ, 516(1):399–410.

Read, J. I. and Gilmore, G. (2003). Can supermassive black holes alter cold dark matter cusps through accretion? *Mon. Not. Roy. Astron. Soc.*, 339:949.

Rein, G. (1994). Static solutions of the spherically symmetric Vlasov-Einstein system. *Math. Proc. Cambridge Phil. Soc.*, 115:559.

Rein, G. and Rendall, A. D. (1992). Global existence of solutions of the spherically symmetric Vlasov-Einstein system with small initial data. *Communications in Mathematical Physics*, 150(3):561 – 583.

Reissner, H. (1916). Über die eigengravitation des elektrischen feldes nach der einsteinschen theorie. *Annalen der Physik*, 355(9):106–120.

Rendall, A. D. and Velazquez, J. J. L. (2011). A Class of dust-like self-similar solutions of the massless Einstein-Vlasov system. *Annales Henri Poincare*, 12:919–964.

Rendall, A. D. and Velázquez, J. J. L. (2017). Veiled Singularities for the Spherically Symmetric Massless Einstein–Vlasov System. *Annales Henri Poincare*, 18(11):3565–3631.

Renteln, P. (2014). *Manifolds, Tensors and Forms*. Cambridge University Press.

Repolust, T., Puls, J., and Herrero, A. (2004). Stellar and wind parameters of Galactic O-stars. The influence of line-blocking/blanketing. A&A, 415:349–376.

Ressler, S. M., Quataert, E., and Stone, J. M. (2018). Hydrodynamic simulations of the inner accretion flow of Sagittarius A* fuelled by stellar winds. MNRAS, 478(3):3544–3563.

Ressler, S. M., White, C. J., Quataert, E., and Stone, J. M. (2020). Ab Initio Horizon-scale Simulations of Magnetically Arrested Accretion in Sagittarius A* Fed by Stellar Winds. ApJ, 896(1):L6.

Ricarte, A., Prather, B. S., Wong, G. N., Narayan, R., Gammie, C., and Johnson, M. (2020). Decomposing the Internal Faraday Rotation of Black Hole Accretion Flows. *Mon. Not. Roy. Astron. Soc.*, 498(4):5468–5488.

Ringström, H. (2013). *On the Topology and Future Stability of the Universe*. Oxford University Press.

Rioseco, P. and Sarbach, O. (2017a). Accretion of a relativistic, collisionless kinetic gas into a Schwarzschild black hole. *Class. Quantum Grav.*, 34(9):095007.

Rioseco, P. and Sarbach, O. (2017b). Spherical steady-state accretion of a relativistic collisionless gas into a Schwarzschild black hole. *J. Phys. Conf. Ser.*, 831(1):012009.

Rioseco, P. and Sarbach, O. (2018). Phase space mixing in the equatorial plane of a Kerr black hole. *Phys. Rev. D*, 98(12):124024.

Rioseco, P. and Sarbach, O. (2020). Phase space mixing in an external gravitational central potential. *Class. Quant. Grav.*, 37(19):195027.

Russell, H. R., Fabian, A. C., McNamara, B. R., and Broderick, A. E. (2015). Inside the Bondi radius of M87. *Mon. Not. Roy. Astron. Soc.*, 451(1):588–600.

Ryan, B. R., Ressler, S. M., Dolence, J. C., Gammie, C., and Quataert, E. (2018). Two-temperature GRRMHD simulations of m87. *The Astrophysical Journal*, 864(2):126.

Rybicki, G. B. and Lightman, A. P. (1985). *Radiative Processes in Astrophysics*. Wiley, New York, NY.

Salucci, P., Turini, N., and Di Paolo, C. (2020). Paradigms and Scenarios for the Dark Matter Phenomenon. *Universe*, 6(8):118.

Sarbach, O. and Zannias, T. (2013). Relativistic Kinetic Theory: An Introduction. *AIP Conf. Proc.*, 1548(1):134–155.

Sarbach, O. and Zannias, T. (2014). The geometry of the tangent bundle and the relativistic kinetic theory of gases. *Class. Quant. Grav.*, 31:085013.

Sarbach, O. and Zannias, T. (2015). Tangent bundle formulation of a charged gas. *AIP Conf. Proc.*, 1577(1):192–207.

Schmidt, M. (1963). 3C 273 : A Star-Like Object with Large Red-Shift. Nature, 197(4872):1040.

Schwarzschild, K. (1916). On the gravitational field of a mass point according to Einstein's theory. *Sitzungsber. Preuss. Akad. Wiss. Berlin (Math. Phys.)*, 1916:189–196.

Shakura, N. I. and Sunyaev, R. A. (1973). Reprint of 1973A&A....24..337S. Black holes in binary systems. Observational appearance. *Astronomy and Astrophysics*, 500:33–51.

Shapiro, S. L. and Teukolsky, S. A. (1983). *Black Holes, White Dwarfs, and Neutron Stars: The Physics of Compact Objects*. Wiley, New York, USA.

Sharma, P., Hammett, G. W., Quataert, E., and Stone, J. M. (2006). Shearing box simulations of the mri in a collisionless plasma. *Astrophys. J.*, 637:952–967.

Shcherbakov, R. V. and Baganoff, F. K. (2010). Inflow-Outflow Model with Conduction and Self-consistent Feeding for Sgr A*. *Astrophysical Journal*, 716(1):504–509.

Straumann, N. (2013). *General Relativity*. Springer-Verlag, Berlin.

Szekeres, P. (1960). On the singularities of a Riemannian manifold. *Publ. Mat. Debrecen*, 7:285–301.

Taylor, M. (2016). The global nonlinear stability of minkowski space for the massless einstein–vlasov system.

The LIGO Scientific Collaboration, The Virgo Collaboration, and The KAGRA Collaboration (2021). GWTC-3: Compact binary coalescences observed by ligo and virgo during the second part of the third observing run.

Turyshev, S. G. (2008). Experimental tests of general relativity. *Annual Review of Nuclear and Particle Science*, 58(1):207–248.

Vereshchagin, G. and Aksenov, A. (2017). *Relativistic Kinetic Theory: With Applications in Astrophysics and Cosmology*. Cambridge University Press.

Wald, R. M. (1984). *General Relativity*. The University of Chicago Press, Chicago, U.S.A.

Walsh, J. L., Barth, A. J., Ho, L. C., and Sarzi, M. (2013). The M87 black hole mass from gas-dynamical models of space telescope imaging spectrograph observations. *The Astrophysical Journal*, 770(2):86.

Wang, Q. D. et al. (2013). Dissecting X-ray-Emitting Gas Around the Center of Our Galaxy. *Science*, 341(6149):981–983.

Weyl, H. (1917). Zur gravitationstheorie. *Annalen der Physik*, 359(18):117–145.

Wheeler, J. A. (1968). Our universe: the known and the unknown. *American Scientist*, 56(1):1–20.

Will, C. M. (2014). The Confrontation between General Relativity and Experiment. *Living Rev. Rel.*, 17:4.

Yuan, F. and Narayan, R. (2014). Hot Accretion Flows Around Black Holes. *Annual Review of Astronomy and Astrophysics*, 52:529–588.

Yuan, F., Quataert, E., and Narayan, R. (2003). Nonthermal Electrons in Radiatively Inefficient Accretion Flow Models of Sagittarius A*. ApJ, 598(1):301–312.

Zank, G. P. (2014). *Transport processes in space physics and astrophysics*. Lecture notes in physics, Volume 877. Springer, New York.

Zeldovich, Y. B. and Novikov, I. D. (1971). *Relativistic Astrophysics. Vol.1: Stars and Relativity*. University of Chicago Press, Chicago, USA.

Appendix A

Fixed-L-models

The purpose of this appendix is to shed some light on the difference between the accretion rates predicted by the mono-energetic model in the purely radial case, Eq. (4.38), and the same model in the presence of angular momentum, Eq. (4.70a). As we have discussed below Eq. (4.74), in the non-relativistic limit $v_R \ll c$ the latter case yields an accretion rate that is smaller (by a factor of 2) compared to the purely radial case. In contrast, there is not such difference for the Maxwell-Jüttner type model when the low temperature limit is taken [cf. the comments below Eq. (4.99)].

To illustrate the role played by the angular momentum in this behavior, we consider the following simple model

$$F(E,L) = f(E)\frac{\delta(L-L_0)}{L_0}, \tag{A.1}$$

in which all the particles have the same angular momentum $L_0 > 0$ and are subject to the energy distribution $f(E)$ which we specify later. Assuming that L_0 is small enough such that $L_0 < L_c(E)$ for all $E > mc^2\alpha(R)$ (which is guaranteed to be the case if $L_0 < L_{\rm ISCO}$), one obtains from Eqs. (4.58) and (4.59) the expressions

$$J^{\hat{\mu}}_{\rm abs}\Big|_{r=R} = c\int\limits_{\sqrt{V_{L_0}(R)}}^{\infty}\int\limits_0^{2\pi}\frac{p^{\hat{\mu}}_- f(E)dEd\chi}{R^2\sqrt{E^2-V_{L_0}(R)}}, \tag{A.2}$$

$$J^{\hat{\mu}}_{\rm sca}\Big|_{r=R} = 0, \tag{A.3}$$

from which one immediately obtains

$$J^0_{\rm abs}\big|_{r=R} = \frac{2\pi}{\alpha(R)R^2}\int\limits_{\sqrt{V_{L_0}(R)}}^{\infty}\frac{f(E)EdE}{\sqrt{E^2-V_{L_0}(R)}}, \tag{A.4}$$

$$J^1_{\rm abs}\big|_{r=R} = -\frac{2\pi}{\alpha(R)R^2}\int\limits_{\sqrt{V_{L_0}(R)}}^{\infty} f(E)dE, \tag{A.5}$$

and $J^2_{\rm abs}\big|_{r=R} = J^3_{\rm abs}\big|_{r=R} = 0$, where we have introduced the shorthand notation

$$V_{L_0}(r) := V_L(r)|_{L\to L_0}\,.$$

For the mono-energetic model with $f(E) = f_0\delta(E-E_0)$ and $E_0 = mc^2\alpha\gamma$ [see Eq. (4.69)], this yields (assuming $V_{L_0}(R) < E_0^2$ or, equivalently, $L_0 < L_{\rm max}(E_0,R)$)

$$\frac{|\dot{M}|}{mcn_R} = 4\pi R^2\alpha(R)\sqrt{\frac{\gamma^2}{1+\kappa^2}-1}, \tag{A.6}$$

where we have defined $\kappa := L_0/(Rmc)$. In the limit $L_0 \to 0$ one recovers the result from Eq. (4.38) which has been derived directly with the assumption that all the gas particles have vanishing angular momentum. If instead of $L_0 \to 0$ one sets $L_0 = R|v_\perp|$ with $v_\perp$ the angular components of the velocity, one obtains in the limit $|v_R| \ll c$,

$$\frac{|\dot{M}|}{mcn_R} \approx 4\pi R^2\alpha(R)\frac{v_{\rm rad}}{c}, \tag{A.7}$$

where $v_{\rm rad} = \sqrt{v_R^2 - |v_\perp|^2}$ denotes the radial component of the three-velocity of the particles. For purely radial infall $v_{\rm rad} = v_R$ and this result agrees precisely with Eq. (4.15). However, when angular momentum is present, the accretion rate is suppressed by a factor of $v_{\rm rad}/v_R$. This illustrates why the accretion rate is smaller for models with angular momentum when n_R and v_R are fixed at the injection sphere.

It is also interesting to apply the model described in Eq. (A.1) to the Maxwell-Jüttner-type distribution function. Inserting $f(E) = Ae^{-\beta E}$ into Eqs. (A.4, A.5) yields the following

non-vanish components of the current density

$$J^0_{\text{abs}}\big|_{r=R} = \frac{2\pi A}{\alpha(R)R^2\beta} z_\kappa \mathbf{K}_1(z_\kappa), \tag{A.8}$$

$$J^1_{\text{abs}}\big|_{r=R} = -\frac{2\pi A}{\alpha(R)R^2\beta} e^{-z_\kappa}, \tag{A.9}$$

where we have set $z_\kappa := \sqrt{1+\kappa^2}z$ and $z = mc^2\alpha(R)\beta$, as defined below Eq. (4.44). This in turn leads to the mass accretion rate

$$\frac{|\dot{M}|}{mcn_R} = \frac{4\pi\alpha(R)R^2}{\sqrt{\left[\mathbf{K}_1(z_\kappa)\, z_\kappa e^{z_\kappa}\right]^2 - 1}}, \tag{A.10}$$

which converges to the same expression as in Eq. (4.45) in the limit $L_0 \to 0$. Whereas the leading-order behavior of the mass accretion rate given in Eq. (A.6) for $v_R \ll c$ and $\kappa \ll 1$ depends on the relation between v_R/c and κ, the limit of the right-hand side of Eq. (A.10) for $z \gg 1$ and $\kappa \ll 1$ always yields $4\alpha(R)R^2\sqrt{2\pi/z}$, regardless of the relation between z and κ. This explains why in the Maxwell-Jüttner case the accretion rate for the models with and without angular momentum agree with each other in the low temperature limit.